Imperial College London
Department of Physics

Optimal control of nonclassical light in optomechanics

Yuxun Ling

Submitted in part fulfilment of the requirements for
the degree of Doctor of Philosophy in Physics and
the Diploma of Imperial College London

March 2024

Supervised by Prof. Florian Mintert

The copyright of this thesis rests with the author. Unless otherwise indicated, its contents are licensed under a Creative Commons Attribution-Non Commercial 4.0 International Licence (CC BY-NC). Under this licence, you may copy and redistribute the material in any medium or format. You may also create and distribute modified versions of the work. This is on the condition that: you credit the author and do not use it, or any derivative works, for a commercial purpose. When reusing or sharing this work, ensure you make the licence terms clear to others by naming the licence and linking to the licence text. Where a work has been adapted, you should indicate that the work has been changed and describe those changes. Please seek permission from the copyright holder for uses of this work that are not included in this licence or permitted under UK Copyright Law.

I hereby declare that the content in this thesis is my own work. Any information used from the workof others has been appropriately acknowledged in the references.

Yuxun Ling

17th March 2024

Acknowledgements

First and foremost, I would like to express my deepest gratitude to Florian Mintert for his comprehensive support throughout my research career. There have been several crucial challenges in the past few years. These include, but are not limited to, the transfer into a physics research field from a math background, the lack of academic writing skills as a non-native speaker, and the difficulty in conducting research during the pandemic. Without his invaluable advice, insights, guidance, and supervision, this work would not have been possible.

I also want to extend my heartfelt thanks to other members of the academic community from whom I received much support. Special mention goes to Sean Greenaway for the countless discussions, for the countless discussions, pushing the boundaries of our understanding, and being my source of personal inspiration. Equally importantly, I am very appreciative of Sofia Qvarfort for her deep insights into the research and general guidance for my PhD career. I would also like to acknowledge Myungshik Kim for his dedication and support to the Quantum Systems Engineering hub.

Last but not least, I want to give my sincere thanks to my friends and family, their faith in me and endless encouragement has been the bedrock on which this work stands. Without their support, I would not have carried on my research, especially during these challenging times.

Abstract

Nonclassical light stands out for its ability to improve quantum metrology, cryptography, and optical quantum computation. Yet, generation of certain types of nonclassical light, especially Fock states, remains a considerable challenge. Optomechanical systems, characterized by a nonlinear interaction between light and a mechanical oscillator, have emerged as a promising avenue to address this challenge. However, these systems also introduce challenges due to the intricate interplay between mechanical and optical components, and the interference of cavity dissipation. This thesis introduces innovative driving strategies that address the two limitations.

First, a driving scheme is proposed to generate separable optomechanical states, while maintaining the nonlinear nature of the system dynamics. This is illustrated with driving profiles leading to an optical two-photon Fock state and its superpositions with the vacuum. While the study mainly focuses on an ideal situation where the system dissipations are neglected, I also show that the fidelity of the final states remain high even when perturbed by the environment.

Then, I consider a more general case where the optical dissipation is no longer negligible. A novel driving scheme is crafted to suppress destructive interference of Fock state amplitudes of more than a single photon. As a result, strong photon-blockade effect can be realized in a time orders of magnitude shorter than in existing schemes that achieve photon blockade in the steady state. Moreover, the driving scheme provides the flexibility to adjust the duration of photon blockade, as well as to increase the single-photon occupation at the cost of weaker photon blockade.

Towards the end, the existing study is extended to include the dynamics of external components. In the study, I consider a simple case where leaked light is directed into a resonant cavity. The range of system parameters where the output cavity also experiences pronounced photon blockade is then identified.

Contents

Abstract **7**

1 Introduction **21**

1.1 Motivation and objectives 21

1.2 Outline of the thesis 24

2 Background Theory **26**

2.1 State of the art 26

2.1.1 Types of nonclassical light 27

2.1.2 Platforms of nonclassical light 28

2.2 Perturbative methods 30

2.2.1 Dyson series 30

2.2.2 Magnus expansion 32

2.3 Optomechanics 33

2.3.1 The optomechanical Hamiltonian 33

2.3.2 Polaron transform and energy level structure 35

2.4 Propagation of closed optomechanical systems 38

2.4.1 Interaction picture 39

2.4.2 Effective Hamiltonian . . . 40
2.4.3 Perturbative expansion . . . 41
2.5 Propagation of open optomechanical systems . . . 44
2.5.1 Lindblad master equation . . . 45
2.5.2 Input-output formalism and cascaded system . . . 48
2.6 Photon blockade and autocorrelation . . . 51

3 Nonclassical light in dissipationless optomechanical systems 53

3.1 Introduction . . . 53
3.2 Design of optimal driving . . . 55
3.2.1 Driving profiles . . . 56
3.2.2 Effective Hamiltonian to second order . . . 57
3.2.3 Third-order corrections . . . 63
3.2.4 Optimized driving pattern . . . 67
3.3 Numerical results . . . 68
3.3.1 Fock state preparation . . . 69
3.3.2 Superposition preparation . . . 72
3.4 Model accuracy . . . 74
3.5 Experimental imperfections . . . 77
3.5.1 Thermal initial states . . . 81
3.5.2 Optical loss . . . 83
3.5.3 Mechanical thermalisation . . . 85
3.6 Conclusions and outlook . . . 87

4 Optomechanical nonclassical light in the presence of cavity dissipation 88

4.1 Introduction . . . 88

4.2 Model and theory . . . 90

4.2.1 Perturbative solution to the system dynamics . . . 90

4.2.2 Dynamics of the autocorrelation function . . . 94

4.3 Numerical results . . . 97

4.3.1 Monochromatic driving . . . 98

4.3.2 Bichromatic driving . . . 101

4.3.3 Extending the lifetime of photon blockade driving . . . 104

4.3.4 Optimization for higher single-photon occupation . . . 106

4.4 Discussion . . . 107

4.4.1 Thermal initial state . . . 107

4.4.2 Mechanical dissipation . . . 108

4.4.3 Validity of perturbative methods . . . 110

4.4.4 System parameters in existing platforms . . . 112

4.5 Conclusions and outlook . . . 113

5 Output states from optomechanical cavity 115

5.1 Introduction . . . 115

5.2 Model . . . 116

5.3 Numerical results . . . 119

5.3.1 Autocorrelation against output dissipation rate . . . 120

5.3.2 Single-photon population against output dissipation rate . . . 124

5.4 Conclusions 126

6 Conclusion **128**

6.1 Thesis achievements and limitations 128

6.2 Future work 130

Bibliography **130**

A Excess reduction in the autocorrelation function due to cascade coupling **151**

B Driving profiles used in plots **156**

B.1 Parameters in Chap. 3 156

B.2 Parameters in Chap. 4 160

B.3 Parameters in Chap. 5 161

List of Figures

2.1 A schematic of the optomechanical system under consideration in this thesis. The system contains a Fabry–Pérot cavity consisting of one fixed mirror and one movable mirror. The cavity supports a single optical mode with resonance frequency ω_{c} and the movable mirror supports a single mechanical mode with resonance frequency ω_{m}. The coupling between the optical mode and the mechanical motion is achieved through radiation pressure, where the light field exerts a force on the movable mirror. Any optical pumping field with driving function $\xi(t)$ (see Eq. (2.7)) enters the cavity only through the fixed mirror to avoid undesired motion in the movable mirror. Both the optical and the mechanical degrees of freedom may suffer from dissipation at rate κ and γ respectively. 34

2.2 Schematic energy-level diagram of the optomechanical system in the polaron frame (refer to Eq. (2.10)). The thick solid lines represent the photonic energy levels (i.e. when $m = 0$), and the thin solid lines represent the energy substructures introduced by the polarons (i.e. when $m \neq 0$). The arrows indicate transition energies between different energy levels. The dashed thick line represents an artificial energy level that has a energy difference with the level $n = 1, m = 0$ equal to the energy difference between the level $n = 0, m = 0$ and the level $n = 1, m = 0$. This artificial level is forbidden in the optomechanical system whenever it does not overlap with any of the energy sublevels induced by polarons. 37

2.3 A schematic of a cacaded system containing two components. The output field of the first system is directed into the second system. 50

3.1 A schematic of the optomechanical system under consideration in this Chapter. The optomechanical system is driven by a temporally modulated, coherent light field. The cavity and the mechanical dissipation are neglected when design optimal driving. . . 55

3.2 Schematic example of a driving pattern of duration $15T = 3\mathcal{T}$. The protocol is comprised of three intervals of length $\mathcal{T} = 5T$ (green, long arrows) characterized by a constant value of the driving amplitude E. Each of these intervals consists of a pair of time-windows of length $2T$ of driven dynamics (black arrow), each of which is followed by half a period of undriven dynamics (red, short arrows). The driving amplitudes shown in the plot serve solely as examples; in actuality, these amplitudes are numerically optimized for each specific target state. 68

3.3 Plots of populations of Fock states in the cavity. Subplot (a) plots populations of even Fock states and subplot (b) plots populations of odd Fock states. The coupling strength is $g_0 = \omega_{\mathrm{m}}/26$, the driving strengths E are optimized with a maximally admissible value $E_{\mathrm{max}} = 4\omega_{\mathrm{m}}$, and the length of evolution is $t_f = 16\mathcal{T}$. A data point is plotted after each five mechanical periods $\mathcal{T}$. The final state is almost a Fock state $|2\rangle$. 70

3.4 Plot of the fidelity F_n against the evolution time t_{f} in $\mathcal{T}$ when $E_{\mathrm{max}} = 4\omega_{\mathrm{m}}$. (a) For each time point, the coupling strength g_0 is optimized to achieve the highest possible fidelity. (b) The coupling strength is fixed to be $g_0 = \omega_{\mathrm{m}}/26$. (c) The coupling strength is fixed to be $g_0 = \omega_{\mathrm{m}}/13$. The combination of interaction strength and evolution time has a great impact on the final fidelity F. 71

3.5 Plots of populations of Fock states in the cavity. Subplot (a) plots populations of even Fock states and subplot (b) plots populations of odd Fock states. The relative coupling strength $g_0 = \omega_{\mathrm{m}}/26$, the relative driving strengths η are optimized with a maximally admissible value $E_{\mathrm{max}} = 4$, and the length of evolution is $t_f = 10\mathcal{T}$. A data point is plotted after each five mechanical periods $\mathcal{T}$. The final state is almost an equal superposition state $1/\sqrt{2}\left(|0\rangle + e^{-1.86i}|2\rangle\right)$. 74

3.6 Plot of theoretical results (solid lines) and numerical results (dashed lines) of the fidelity between the final state and a two-photon Fock state. Each data point represents the fidelity of the final state when the driving function is optimized for the generation of two-photon Fock state at the given time on x-axis. Subplot(a) and (b) represent cases where $g_0 = \omega_{\mathrm{m}}/26$ and $g_0 = \omega_{\mathrm{m}}/13$ respectively, and the maximum admissible driving strengths are as shown in the plot legend. 75

3.7 Optomechanical system considered in this section include optical dissipation, mechanical dissipations, or initial thermal occupation. The optical and mechanical dissipation rates are denoted as κ and γ, the thermal occupation of the heat bath related to mechanical dissipation is denoted as $\bar{n}_{\mathrm{b}}$, and the initial thermal occupation of the optomechanical oscillator is denoted as $\bar{n}_{\mathrm{th}}$. 77

3.8 Plots of the fidelities (a) F_{l} and (b) F_{i} against mean thermal phonon numbers $\bar{n}_{\mathrm{th}}$ of initial states for optimized driving profiles with parameters $(g_0, E_{\mathrm{max}}, t_{\mathrm{f}})$ equal to (i) $(\omega_{\mathrm{m}}/26, 4\omega_{\mathrm{m}}, 16\mathcal{T})$, (ii) $(\omega_{\mathrm{m}}/21, 4\omega_{\mathrm{m}}, 10\mathcal{T})$, and (iii) $(\omega_{\mathrm{m}}/16, 4\omega_{\mathrm{m}}, 5\mathcal{T})$, respectively. All fidelities remain higher than 0.9 when $\bar{n}_{\mathrm{th}} < 1$ except for the case of $(\omega_{\mathrm{m}}/16, 4\omega_{\mathrm{m}}, 5\mathcal{T})$ where the fidelity F_{l} drops below 0.8. The exception may arise from the higher order entanglement that is amplified by excitations in the mechanical oscillator. 82

3.9 Plots of the fidelities (a) F_{l} and (b) F_{i} against relative optical decay rates $10^4\kappa/\omega_{\mathrm{m}}$ of the lossy cavity for optimized driving profiles with parameters $(g_0, E_{\mathrm{max}}, t_{\mathrm{f}})$ equal to (i) $(\omega_{\mathrm{m}}/26, 4\omega_{\mathrm{m}}, 16\mathcal{T})$, (ii) $(\omega_{\mathrm{m}}/21, 4\omega_{\mathrm{m}}, 10\mathcal{T})$, and (iii) $(\omega_{\mathrm{m}}/16, 4\omega_{\mathrm{m}}, 5\mathcal{T})$, respectively. The x-axis is in log scale while the y-axis is in linear scale. The plots suggest that the fidelity drops dramatically with the increase in optical decay rate when the decay rate exceeds $10^{-4}\omega_m$, and that shorter evolution time leads to a more resilient state. 84

3.10 Plots of the fidelities (a) F_{l} and (b) F_{i} against relative mechanical decay rates $10^4\gamma/\omega_{\mathrm{m}}$ of the lossy cavity for optimized driving profiles with parameters $(g_0, E_{\max}, t_{\mathrm{f}})$ equal to (i) $(\omega_{\mathrm{m}}/26, 4\omega_{\mathrm{m}}, 16\mathcal{T})$, (ii) $(\omega_{\mathrm{m}}/21, 4\omega_{\mathrm{m}}, 10\mathcal{T})$, and (iii) $(\omega_{\mathrm{m}}/16, 4\omega_{\mathrm{m}}, 5\mathcal{T})$, respectively. Solid and dashed curves represent cases when the thermal bath contains on average $\bar{n}_{\mathrm{b}} = 1$ (solid), $\bar{n}_{\mathrm{b}} = 10$ (dashed) phonons respectively. The x-axis is in log scale and the y-axis is in linear scale. The plots suggest that the infidelity resulting from mechanical imperfection is negligible compared to that from optical imperfection when the thermal phonon number $\bar{n}_{\mathrm{b}} \ll 10$, but becomes noticeable otherwise. . 86

4.1 A schematic of the optomechanical system under consideration in this Chapter. The optomechanical cavity is driven by two coherent light sources with different temporal dependence. The optical dissipation (with rate κ) is explicitly included in the design of the driving, while the mechanical dissipation is neglected. 91

4.2 A replicate of the optomechanical energy-level diagram in Fig. 2.2. 99

4.3 The value of the autocorrelation function $g^{(2)}$ as a function of the target time t_{op} in terms of mechanical periods ($T = 2\pi/\omega_{\mathrm{m}}$) when the approximate autocorrelation function $\tilde{g}^{(2)}(t_{\mathrm{op}})$ is minimized with respect to the drive detuning Δ at the considered time t_{op}. Different values of the optomechanical coupling strength $g_0 = 0.3\omega_{\mathrm{m}}$ (cross), $g_0 = 0.4\omega_{\mathrm{m}}$ (circle), and $g_0 = 0.5\omega_{\mathrm{m}}$ (triangle) and $g_0 = 0.6\omega_{\mathrm{m}}$ (star) are considered. The driving strength is $E = \omega_{\mathrm{m}}/200$ and the cavity decay rate is $\kappa = 0.02\omega_{\mathrm{m}}$. The minimized autocorrelation function decreases when either the driving strength or the evolution time increases, but strong photon blockade ($g^{(2)} \sim 10^{-4}$) cannot be observed within the range of parameters considered. 100

4.4 Single-photon occupation p_1 (dashed), two-photon occupation p_2 (dotted) and autocorrelation function $g^{(2)}$ (solid) as functions of time for parameters that minimize the autocorrelation function at the 5-th mechanical period when the parameters have the values $E = \omega_{\mathrm{m}}/200$, $g_0 = 0.3\omega_{\mathrm{m}}$, $\kappa = 0.02\omega_{\mathrm{m}}$, and the drive detuning and phases are optimized. Subplot (a) corresponds to the dynamics when the driving is bichromatic and strong photon blockade ($g^{(2)} \sim 10^{-4}$) can be observed at $5T$. Subplot (b) corresponds to the dynamics when the driving is monochromatic and the lowest value of the autocorrelation function only reaches 10^{-1}. 102

4.5 The minimal value of autocorrelation function against the relative cavity decay rate $\kappa/\omega_{\rm m}$ when $t_{\rm op} = 5T$ (circle) and $t_{\rm op} = 10T$ (cross). The driving strength is $E = \omega_{\rm m}/200$ and optomechanical coupling rate is $g_0 = 0.3\omega_{\rm m}$. The minimal values of the autocorrelation function increase as the cavity decay increases, but do not have a monotonic dependence on the evolution time. 103

4.6 Single-photon occupation p_1 (dashed), two-photon occupation p_2 (dotted) and autocorrelation function $g^{(2)}$ (solid) as functions of time for parameters that minimize the target function Eq. (4.27) at 5-th mechanical period when the parameters have the values $E = \omega_{\rm m}/200$, $g_0 = 0.3\omega_{\rm m}$ and $\kappa = 0.02\omega_{\rm m}$. The autocorrelation function stays around its minimum for approximately 0.2 mechanical periods. 105

4.7 The autocorrelation function $g^{(2)}$ as a function of the relative mechanical decay rate $\gamma/\omega_{\rm m}$ for average phonon number in the heat bath being $\bar{n}_{\rm b} = 0$ (cross), $\bar{n}_{\rm b} = 0.1$ (circle), $\bar{n}_{\rm b} = 1$ (triangle), and $\bar{n}_{\rm b} = 10$ (square). The dashed line specifies the value of the autocorrelation function that is 10% larger than the value without the mechanical loss (i.e. $\gamma = 0$). The assumptions of vanishing mechanical decay rate $\gamma \ll \omega_{\rm m}$ and environmental phonon occupation $\bar{n_b} \approx 0$ are required in order to achieve strong photon blockade. 109

4.8 The autocorrelation $g^{(2)}$ and $\tilde{g}^{(2)}$ as functions of the driving strength $E/\omega_{\rm m}$ rescaled by the mechanical frequency. The circular data points plot the exact autocorrelation values $g^{(2)}(5T)$ obtained from a full numerical simulation. The cross data points plot the approximate autocorrelation values $\tilde{g}^{(2)}(5T)$ obtained from numerical simulation. The dashed curve plots the case when the perturbative expansion is truncated up to the order $(g_0/\omega_{\rm m})^2$ (i.e. $(g_0/\omega_{\rm m})^4 \ll 1$). The dotted curve plots the case when the relevant perturbative expansion is truncated to a higher order which imposes a less strict condition (i.e. $(g_0/\omega_{\rm m})^8 \ll 1$) on the coupling strength. The inset zooms into the results for small driving strengths. The figure shows that a weak driving strength is necessary for obtaining the results in this paper. 111

5.1 Subplot (a) displays a schematic of the cascaded optomechanical system under consideration in this Chapter. This model can serve for analyzing the specific mode output field of the optomechanical cavity. The system comprises an optomechanical setup and a second cavity (output component). The output light from the optomechanical cavity is directed into the output component using a unidirectional waveguide. Subplot (b) display the same physical setup but plotted in a different way to highlight the optical input and output ports. The optomechanical cavity involves two pairs of optical input and output ports ($a_{\mathrm{l,in}}$, $a_{\mathrm{l,out}}$ and $a_{\mathrm{r,in}}$, $a_{\mathrm{r,out}}$). The output component has one pair of optical input and output ports ($a_{2,\mathrm{in}}$, $a_{2,\mathrm{out}}$). The coupling between the optomechanical cavity and the output component is unidirectional, with $a_{\mathrm{r,out}} = a_{2,\mathrm{in}}$. 118

5.2 Temporal dependence of output autocorrelation, $g^{(2)}_{\mathrm{out}}(t)$, across different output dissipation rates $\kappa_2 \in [10^{-2}/\omega_{\mathrm{m}}, 10/\omega_{\mathrm{m}}]$. The dotted curves represent output autocorrelation values when the optomechanical parameters read $E = \omega_{\mathrm{m}}/200$, $g_0 = 0.3\omega_{\mathrm{m}}$, $\kappa_l = \omega_{\mathrm{m}}/100$, $\kappa_r = \omega_{\mathrm{m}}/100$. Subplot (a) and (b) correspond to simulations under the driving profiles (ii) $g_0 = 0.3\omega_{\mathrm{m}}$ and (iv) $g_0 = 0.3\omega_{\mathrm{m}}$ with broader minimum, respectively. The dashed lines connect minimum output autocorrelation values, $(t_{\mathrm{min}}, g^{(2)}_{\mathrm{out}}(t_{\mathrm{min}}))$. The solid curve presents the optical autocorrelation $g^{(2)}_{\mathrm{op}}(t)$ within the optomechanical cavity, which mirrors the temporal dependence shown in Fig. 4.4(a) and Fig. 4.6 for subplots (a) and (b) respectively. 120

5.3 Plots of (a) the minimum autocorrelation $g^{(2)}_{\mathrm{out}}(t_{\mathrm{min}})$ in the output cavity; (b) the time t_{min} at which the output autocorrelation achieves its minimum, each as a function of the output cavity decay rate κ_2. The four distinct curves in each subplot correspond to instances where: (i) $g_0 = 0.28\omega_{\mathrm{m}}$, (ii) $g_0 = 0.3\omega_{\mathrm{m}}$, (iii) $g_0 = 0.32\omega_{\mathrm{m}}$, and (iv) $g_0 = 0.3\omega_{\mathrm{m}}$ with the driving parameters optimized for an extended duration of photon blockade. The remaining optomechanical parameters are set as $(E, \kappa_l, \kappa_r) = (\omega_{\mathrm{m}}/200, \omega_{\mathrm{m}}/100, \omega_{\mathrm{m}}/100)$. The optimized driving profiles can be found in Appendix B.3. 122

5.4 Ratio of the single-photon population $p_{1,\text{out}}/p_{1,\text{op}}$ (a) as a function of evolution time for a range of different output dissipation rate ($\kappa_2 \in [0.01, 10]$) for the parameter set ((ii)) (i.e. same as in Fig. 5.2(a)), (b) at the time point when the photon blockade effect is the strongest for the output component and the optomechanical cavity respectively (y-axis) against the output decay rate (x-axis), where: (i) $g_0 = 0.28\omega_\text{m}$, (ii) $g_0 = 0.3\omega_\text{m}$, (iii) $g_0 = 0.32\omega_\text{m}$, and (iv) $g_0 = 0.3\omega_\text{m}$ with the driving parameters optimized for an extended duration of photon blockade. 125

A.1 Time evolution of the autocorrelation function in the output cavity for the initial system state described in Eq. (A.6), with parameters $p_{1,\text{op}} = p_{1,\text{out}} = 0.1$, $g^{(2)}_{\text{op}} = 10^{-3}$, $g^{(2)}_{\text{out}} = 10^{-4}$, $\psi_{2,\text{op}} = \psi_{2,\text{out}} = 0$, and the vacuum and two-photon populations are determined by the values of autocorrelation and the normalization condition. The x-axis is plotted in the unit of coupling strenth (i.e. $\sqrt{\kappa_2\kappa_r} = 1$) The three curves correspond to the cases where the phase of the single-photon components are $\psi_{1,\text{op}} = \psi_{1,\text{out}} = 0, \pi/4, \pi/2$, respectively. For these three values, c_3 in Eq. (A.8) is positive, zero and negative, respectively, and so does the derivatives of the three curves at $t = 0$. The gray dashed line represents the autocorrelation value in the optomechanical cavity. . . 155

List of Tables

4.1 The values of the sign variables $s_{j,k}^{(i,j)}$ in Eq. (4.21). 96

4.2 System parameters in experiments in comparison with the parameters adopted in this paper and the strength of the resulting photon blockade at the target time $t_{\rm op} = 5T$. The coupling strength assumed in this paper is too large in comparison with experimental data in the work on nano-acoustic resonators. The parameters in the theoretical work [1] suggest that hybrid systems potentially constitute good platforms for realizing photon blockade. 113

B.1 Parameters in Sec. 5.3. 161

Chapter 1

Introduction

1.1 Motivation and objectives

Nonclassical light has become increasingly significant for various reasons, including its ability to enhance accuracy in quantum metrology [2–4], provide resources for quantum cryptography [5–7], and facilitate optical quantum computation to outperform classical computation [8, 9]. Despite the wide range of applications, generating nonclassical states of light from classical resources poses significant challenges. This difficulty arises from the linear nature of commonly used optical components such as mirrors and lenses, which preserve the classical nature of light passing through them.

A specific challenge is the generation of non-vacuum Fock states of light on demand. Since the first successful generation of single photons [10], heralding schemes have become the most popular method for generating optical Fock states [11–14]. These schemes exploit the simultaneous emission of two highly correlated photons into two different modes, i.e. the signal mode and the idler mode. The signal mode is continuously monitored so that the detection of a photon indicates the successful generation of a photon in the idler mode. Despite the success, such schemes suffer from their probabilistic nature. For example, these schemes are limited by their probabilistic nature, as sometimes more or fewer than two photons are emitted simultaneously, or the signal photon is not detected due to detector inefficiencies.

To overcome these limitations, schemes using single particles as photon sources have been proposed, including cavity quantum electrodynamics [15–18] and solid-state artificial atoms [19–21]. Currently, single photons can be generated in such systems with near-optimal purity ($g^{(2)}(0) < 10^{-3}$) and indistinguishablility ($> 99\%$) [22]. Multi-photon states can also be prepared in laboratories with up to 15 photons [23], and theoretical proposals exist for generating 100 or more photons [24, 25]. However, a primary limitation of these systems is that the generated photons are usually in the microwave range, which do not interact efficiently with optical components. While significant advances have been made in microwave-to-optical transducers, the best experimentally available transducers still require improvements to achieve near-unit efficiency [26–28].

A promising approach to overcoming the aforementioned limitations is the utilization of optomechanical systems [29]. The typical optomechanical system under consideration in this thesis contains one Fabry-Pérot cavity and one mechanical oscillator. When light is pumped into the optomechanical cavity, it nonlinearly interacts with the mechanical oscillator via radiation pressure. This interaction results in a coupling between the intensity of the light and the position of the oscillator, leading to a Kerr-like nonlinearity in the optical energy-level spectrum. In the past decades, there are several proposals for optomechanical systems to generate nonclassical light, including squeezed states [30], cat states [31][1], and photon-blockaded states [32]. Remarkably, the optical part of the system can be equivalently treated as a cavity with Kerr medium [33, 34], which further guarantees its ability to generate a wide range of nonclassical lights.

Apart from the ability to generate nonclassical lights, optomechanical systems also offer several advantages. One such advantage is that interconversion of nonclassical optical and mechanical states is possible through optomechanical systems. The interconversion offers a more reliable method to store nonclassical lights [35–37] due to the higher robustness of the mechanical oscillators compared to the cavity. Furthermore, it also opens up the possibility of preparing macroscopic nonclassical states. Another advantage of optomechanical systems is their compatibility with other systems through hybridization. For example, incorporating a nonlinear medium in the optomechanical cavity enhances the effective optomechanical nonlinearity, thus overcoming the limitations imposed by either the system or the medium alone [38, 39].

[1] The reference contains schemes both for generating optical cat states and for generating mechanical cat states.

Despite numerous appealing advantages, optomechanical systems also have several limitations. One limitation is that the optomechanical coupling induces correlation between the optical and mechanical degrees of freedom. Although pure states of either subsystem can be prepared through projective measurement on the other subsystem, precise measurement of mechanical motion is generally challenging. Furthermore, such schemes [40, 41] are intrinsically probabilistic with a success probability limited by the multitude of possible measurement outcomes.

A second limitation lies in the coupling strength between the oscillator and the cavity, which is in general low relative to the cavity dissipation rate. For the generation of any nonclassical light, physical constraints typically demand a system nonlinearity that exceeds the cavity dissipation [42, 43]. Numerous efforts have been directed toward enhancing the optomechanical coupling strength beyond the cavity dissipation rate [29, 44]. However, simply achieving parity in this context does not guarantee generation of nonclassical, pure states with high fidelity. Under such conditions, the preparation of a nonclassical state often necessitates a duration comparable to the cavity relaxation time, consequently resulting in a highly mixed final state with a diminished fidelity to the desired target state.

This thesis proposes solutions to overcome these limitations through the design of optimal driving. I show that, by controlling the optomechanical cavity through classical mixtures of coherent light fields with suitable temporal phases and amplitudes, the light-matter correlation in the final state can be suppressed to leading orders. In the ideal scenario of negligible system dissipation, the optical final state exhibits a high degree of similarity to target nonclassical states, including two-photon Fock state and superposition states of two-photon Fock state and vacuum. I also demonstrate that, despite non-vanishing optical dissipation rates, optomechanical systems can generate highly nonclassical light with low autocorrelation values. This is achievable within the time frame where the generation of nonclassical light is not achievable with a single coherent source alone.

Regarding practicality, it is important to note that although the assumed parameters may not be readily available under current experimental conditions, ongoing experimental progress suggests promising advancements. The two most important assumptions in this thesis, strong coupling compared to cavity dissipation rates and ground-state cooling for mechanical initial state preparation, have received significant attention in the optomechanical systems literature [45–48].

In terms of extensibility, it is worth mentioning that while this thesis primarily focuses on the generation of Fock states and their superposition states with vacuum, the proposed techniques can be applied to a wider range of target states such as cat states and superposition with higher-lying Fock states. Furthermore, these techniques are not limited to the specific optomechanical setup considered in this thesis but can be extended to other systems with similar nonlinear terms in the Hamiltonian.

1.2 Outline of the thesis

Chapter 2 provides the necessary background for this thesis. I present a state-of-the-art review of optical nonclassical states and optomechanical systems. Detailed presentations of the required mathematical tools are provided, along with a methodology for designing driving profiles for optomechanical systems.

Chapter 3 is dedicated to the design of a driving profile for generating pure, nonclassical optical states in optomechanical systems. I demonstrate the creation of a two-photon Fock state and its superpositions with the vacuum state. The quality of the driving profile and its robustness under system dissipation are subsequently analyzed. The content of this chapter is primarily based on the following publication:

Ling, Yuxun, and Mintert, Florian. "Deterministic preparation of nonclassical states of light in cavity optomechanics." Phys. Rev. Research **3**, 033071 (2021).

Chapter 4 introduces a protocol for inducing a strong photon blockade effect in the presence of significant cavity dissipation. I illustrate how this protocol outperforms existing steady-state schemes. The versatility of the protocol in balancing the strength, duration of photon blockade, and the single-photon population is also explored. The content of this chapter is primarily based on the following publication:

Ling, Yuxun, Qvarfort, Sofia, and Mintert, Florian. "Fast optomechanical photon blockade." Phys. Rev. Research **5**, 023148 (2023).

Chapter 5 further extends the study to incorporate an output component that captures the light field

leaked from the optomechanical cavity. I demonstrate that a strong photon blockade can be transferred into the output component with high fidelity, and the parameter range for this phenomenon is delineated.

Chapter 6 presents final remarks and offers perspectives and recommendations for future investigations.

Chapter 2

Background Theory

The primary focus of this initial chapter is devoted to providing the necessary background knowledge essential for a comprehensive understanding of this thesis. Specifically, this chapter reviews the state of the art in the non-classical quantum states and single-photon sources, the basis of quantum optomechanics and the theory of open quantum systems.

2.1 State of the art

In recent years, the field of nonclassical light has witnessed remarkable progress and garnered significant attention within the realm of quantum optics and quantum information. As researchers and technologists delve deeper into the fascinating properties of quantum systems, exploring the generation, manipulation, and utilization of nonclassical light has become a focal point of investigation. This section aims to provide an overview of the state of the art in this rapidly advancing field, highlighting the latest advancements and key developments that have propelled the research and applications of nonclassical light and single-photon sources.

2.1.1 Types of nonclassical light

Nonclassical states of light encompass a wide range of useful states, with certain types garnering significant interest among researchers. To provide clarity on their classification, nonclassical states can be primarily divided into Gaussian nonclassical states and non-Gaussian states.

Gaussian nonclassical states: Gaussian optical states are distinguished by their Gaussian-shaped Wigner characteristic function [49]: $\chi(\boldsymbol{\alpha}) = \mathrm{Tr}\big(D(\boldsymbol{\alpha})\rho\big)$ where ρ represents the density matrix of the state, $\boldsymbol{\alpha}$ represents a vector of the variables α_k, and $D(\boldsymbol{\alpha}) = \prod_k \exp\Big(\alpha_k a_k^\dagger - \text{h.c.}\Big)$ represents the displacement operator for optical modes with creation operators $a_k^\dagger$. Significantly, Gaussian states can be fully described by their first and second moments (i.e. the mean fields and covariance matrices) [50]. Another crucial characteristic of Gaussian states is that they remain Gaussian under any quantum process with a quadratic Hamiltonian [51]. Because all classical optical components have linear or quadratic Hamiltonian, dynamics of Gaussian states, when interacting with classical optical components, is both well-studied [52] and efficiently simulatable on classical machines [53].

Notably, while many Gaussian states possess classical properties, there exist exceptions, such as the squeezed states of light. Squeezed states are characterized by reduced quantum noise in one quadrature at the expense of increased noise in the conjugate quadrature. Benefiting from the reduced noise in the target quadrature, squeezed light plays a vital role in enhancing the sensitivity of quantum sensors, overcoming limitations imposed by the Heisenberg principle [54–57].

Non-Gaussian states: Non-Gaussian states are defined as any quantum states that are not Gaussian. These states hold paramount importance in the realm of continuous-variable quantum computing because at least one non-Gaussian element is required for any continuous-variable quantum computer to be universal [51, 58, 59]. However, their significance is accompanied by challenges, as non-Gaussian states are in general much harder to generate [60, 61].

In contrast to Gaussian states, all non-Gaussian pure states invariably exhibit nonclassical characteristics [62, 63]. One important type of non-Gaussian state is the Fock state of light (excluding vacuum states), characterized by a well-defined number of photons occupying a specific mode. They can be viewed as a special type of squeezed states with extreme squeezing in the amplitude but ill-defined

phase, and thus attain the ultimate quantum limit in the estimation of the loss parameter of a bosonic channel [64]. Moreover, Fock states are also common resources for generating entangled states through phenomena like the Hong-Ou-Mandel effect. Furthermore, because single photons interact minimally with the environment, they are good candidate as qubits for quantum computing [65,66]. Overall, nonclassical states of light constitute an active and important field of research, with ongoing researches exploring additional types of nonclassical states and their diverse applications.

In addition to Fock states, entangled non-Gaussian states also play a vital role in the family of nonclassical light. Besides the wide range of applications of single-mode non-Gaussian states, the entanglement uniquely permits a regime of heralded measurements in which a measurement of one component determines without destroying the state of the other components. Therefore, entangled states serve as key building blocks in quantum communication and quantum error correction protocols [66–68].

2.1.2 Platforms of nonclassical light

While generating high-fidelity nonclassical states of light can be challenging, significant progress has been made on numerous platforms. It is worth mentioning that an exhaustive list of all possible platforms is beyond the scope of this thesis, but this subsection aims to offer a concise overview of some of the most commonly used ones.

The earliest approach to generate quantum light is by pumping light through bulk nonlinear materials [69–71]. While different materials may induce different physical processes on light fields, one particularly important phenomenon is the parametric down-conversion which converts one single input light field into two correlated output light fields. Parametric down-conversion materials are well-suited for heralded schemes and entanglement generation, making them still among the most commonly used sources for single and entangled photons up to date [72–74]. One drawback of parametric down-conversion as a photon source is that due to the inherent weak nonlinearity, it is either that the pumping is weak with low probability of generating photon pairs, or that the pumping is strong so that more than one pair of photon can be generated at the same time. This probabilistic nature introduces a limitation in the overall efficiency of generating desired photon pairs.

To overcome the low efficiency problem, deterministic schemes are preferred. One approach to generate on-demand nonclassical light is to take advantage of stimulated emission or fast spontaneous emission in isolated systems such as single atoms [10, 15], defects in diamond [75] or quantum dots [76]. Despite their relatively shorter history, isolated systems show promising experimental progress in deterministically generating single photons with high purity [19, 20, 22, 77–80]. One possible limitation of isolated systems is the difficulty of confining the generated photons in any specific spatial mode. The isolated systems are also potentially vulnerable to the thermal environment.

Given that there has not been a perfect nonclassical light source, there are more proposals using emerging platforms. While experiments on these platforms may still be in their early stages, each platform offers unique advantages that make them worthy of dedicated research. One such candidate are superconducting circuits, where a Josephson junction is effectively a third-order (Kerr-like) nonlinear medium interacting with microwave photons. Recently, experiments successfully realized broadband squeezed microwaves with single-mode squeezing on par with the best resonator-based squeezers [81] and on-demand directional photon emission [82] using superconducting circuits. One unique advantage of superconducting circuits is that they are relatively easy to be scaled up and incorporated into superconducting systems for quantum information and quantum communication. However, the main disadvantage is that a cryogenic environment is required.

Another emerging platform are optomechanical systems, which consist of one optical cavity coupled with one mechanical oscillator, such that a Kerr-like nonlinearity is realized through radiation pressure. In contrast to superconducting circuits, optomechanical systems do not necessarily operate in cryogenic conditions. Recent advancements have even achieved light squeezing at room temperature [83]. Another advantage of optomechanical systems is that the frequency of the light field is determined by the length of the cavity, which offers higher tunability than nonlinear systems relying on inherent energy-level structure of the material. However, the main drawback lies in the ongoing challenge of achieving a coupling rate faster than photon dissipation [29, 45, 84, 85], which, in turn, limits the practical realization of applications demanding high nonlinearity (e.g. photon generation) to a theoretical stage.

2.2 Perturbative methods

In Sec. 2.1, the significance of nonlinear optics, especially those exhibiting non-Gaussian dynamics, has been underscored. However, alongside the experimental challenges involved in generating non-Gaussian light (as discussed in Sec. 2.1.2), it is noteworthy that non-Gaussian operations often render the attainment of exact solutions to the system dynamics unfeasible. This lack of solutions not only hinders a theoretical understanding of the quantum system but also obstructs the design of optimal control for such a system. In this section, I present two widely employed methods that offer a pathway to navigate this conundrum: the Dyson series and the Magnus series. Both methods provide perturbative solutions to the time evolution operator $U(t_0, t)$ induced by a potentially time-dependent system Hamiltonian $H(t)$, which satisfies the Schrödinger equation $idU/dt = HU$.

2.2.1 Dyson series

The Dyson expansion of an evolution operator $U(t_0, t)$, induced by the Hamiltonian $H(t)$, can be succinctly expressed as follows [86]

$$\begin{aligned} U(t_0, t) =& \mathbb{1} + \sum_{k=1}^{\infty} \mathcal{D}_k(t_0, t) \\ =& \mathbb{1} + \sum_{k=1}^{\infty} (-i)^k \int_{\boldsymbol{t}^{(k)} \in \mathbb{T}_k} H(t_k) \dots H(t_1) d\boldsymbol{t}^{(k)} \end{aligned} \tag{2.1}$$

where $\boldsymbol{t}^{(k)} = (t_1, \dots, t_k)$ represents a vector of time variables, and $\mathbb{T}_k$ is the k-simplex domain $t > t_k > \dots > t_1 > t_0$ in which the time variables are time-ordered. Notably, this expansion applies irrespective of the Hermitian nature of the Hamiltonian, making it applicable both to closed systems with unitary evolution operators and open systems with non-unitary evolution operators.

When time-dependence is omitted, the contribution of the k-th order to the Dyson series is proportional to the k-th power of the Hamiltonian H. Therefore, when the Hamiltonian H is unbounded, namely the eigenvalues of the Hamiltonian extend to infinity, the convergence of the Dyson series is not assured. While an exhaustive analysis of the convergence properties of unbounded operators lies beyond the scope of this thesis, interested readers can consult specialized resources such as references [87, 88]. A

concrete example that showcases the divergence of the Dyson series at each order except the lowest is also presented in the reference [89].

While the convergence of the Dyson series remains a difficult question, in many optical experiments, including the generation of single photons, the typical number of photons involved is limited. In such cases, the associated Hilbert space can be truncated to finite dimension, leading to a bounded Hamiltonian that guarantees convergence of the Dyson series [90][1]. Furthermore, the Dyson series is asymptotic in the sense that truncating it to finite orders can provide sufficiently accurate descriptions of the system dynamics [92]. In particular, truncated Dyson series have been applied to several quantum optical systems including two-level systems [93,94] and spontaneous parametric down-conversion systems [95].

One advantage of the Dyson series lies in its simplicity. Numerical benchmarks have demonstrated that Dyson series truncated to low orders can significantly speed up the computation of evolution operators compared to other commonly employed methods [96]. While truncation to low order in Dyson series only provides accurate results over short time intervals, it is feasible to approximate the total evolution operator $U(t_0, t)$ over longer durations by the product of n evolution operators over shorter time intervals as

$$U(t_0,t) \approx \tilde{U}\left(\frac{n-1}{n}t, t\right)\tilde{U}\left(\frac{n-2}{n}t, \frac{n-1}{n}t\right)\ldots\tilde{U}\left(0, \frac{1}{n}t\right) \tag{2.2}$$

where $\tilde{U}((j-1)t/n, jt/n)$ $(j = 1, \ldots, n, t_n = t)$ is the truncated Dyson series of the evolution operator over the time interval $((j-1)t/n, jt/n)$. This approach takes advantage of the speed enhancement provided by the truncation of Dyson series to low orders for the evolution operator $U((j-1)t/n, jt/n)$ over each shorter time period, while still maintaining high accuracy for the overall evolution operator $U(t_0, t)$ [96–98].

On the other hand, a notable limitation of the truncated Dyson series lies in its inability to preserve essential physical attributes inherent to the evolution operator. For example, the truncated Dyson series do not necessarily preserve the trace of the system state. Moreover, the time symme-

[1] When the Hamiltonian can be expressed as a finite-dimensional matrix, Dyson series is also referred to as Peano-Baker series [91].

try $U(t_0,t) = U^{-1}(t,t_0)$ becomes compromised when approximated through the truncated Dyson series. Additionally, when applied to systems governed by Hermitian Hamiltonians, the Dyson series truncated to second or higher orders may fail to maintain the unitarity of the evolution operator. These limitations potentially lead to difficulties in theoretical researches.

2.2.2 Magnus expansion

The Magnus expansion of an evolution operator $U(t_0,t)$, induced by the Hamiltonian $H(t)$, takes the following form [99]

$$U(t_0,t) = \exp\left(-i\mathcal{M}_j(t_0,t)\right) \ , \tag{2.3}$$

where the exponents $\mathcal{M}_j$ can be recursively generated through the equations [100]

$$\begin{aligned}
\mathcal{M}_1(t_0,t) &= \int_{t_0}^{t} H(t_1)dt_1 \ , \\
\mathcal{M}_k(t_0,t) &= (-i)^{k-1}\sum_{j=1}^{k-1}\frac{B_j}{j!}\sum_{\substack{s_1+\ldots+s_j=k-1\\ s_1\geq 1,\ldots,s_j\geq 1}}\int_{t_0}^{t}\mathrm{ad}_{\mathcal{M}_{s_1}(u)}\ldots\mathrm{ad}_{\mathcal{M}_{s_j}(u)}H(u)du \ ,
\end{aligned} \tag{2.4}$$

the linear operator ad is defined as $\mathrm{ad}_{\mathcal{M}}(H) = [\mathcal{M},H]$, and the real constants B_j are the Bernoulli numbers derived from the exponential generating function $x/(e^x-1) = \sum_{j=0}^{\infty} B_j x^j/j!$. To illustrate, the expressions for the second and third order Magnus terms are as follows

$$\begin{aligned}
\mathcal{M}_2(t_0,t) &= -\frac{i}{2}\int_{\boldsymbol{t}^{(2)}\in\mathbb{T}_2}[H(t_2),H(t_1)]d\boldsymbol{t}^{(2)} \\
\mathcal{M}_3(t_0,t) &= -\frac{1}{6}\int_{\boldsymbol{t}^{(3)}\in\mathbb{T}_3}[H(t_3),[H(t_2),H(t_1)]]+[[H(t_3),H(t_2)],H(t_1)]d\boldsymbol{t}^{(3)} \ ,
\end{aligned} \tag{2.5}$$

where $\boldsymbol{t}^{(k)}$ and $\mathbb{T}_k$ are defined following Eq. (2.1).

There exists a bijective correspondence between the Magnus expansion and the Dyson series: each Magnus term $\mathcal{M}_k$ can be expressed as a finite polynomial of the Dyson terms $\mathcal{D}_1,\ldots,\mathcal{D}_k$, and conversely, each Dyson term $\mathcal{D}_k$ can be expressed as a finite polynomial of the Magnus terms $\mathcal{D}_1,\ldots,\mathcal{D}_k$ [100–102]. Similar to the Dyson series, the convergence of the Magnus series is not guaranteed when the Hamiltonian is unbounded [103]. However, the Magnus series has a finite radius of convergence even

when the Hamiltonian is bounded [104–106]. Nonetheless, in the perturbative regime where characteristic frequency of the Hamiltonian $H(t)$ is small relative to $1/t$, truncated Magnus series are widely considered as reliable approximations to the evolution operator $U(t_0, t)$, and have been successfully applied in diverse scenarios [107–111]. Furthermore, the Magnus expansion, combined with the technique in Eq. (2.2), offers a means to approximate evolution over extended time intervals [112].

An eminent advantage of the Magnus expansion lies in its ability to preserve the physical attributes of the evolution operator. Specifically, it preserves properties like the trace of the system state, the evolution operator's time symmetry (i.e. $U(t_0, t) = U^{-1}(t, t_0)$), and the unitarity of the evolution operator induced by a Hermitian Hamiltonian. Furthermore, when truncated to the same order, the Magnus expansion (if converges), provides a more accurate approximation to the evolution operator compared to the Dyson series [96].

2.3 Optomechanics

2.3.1 The optomechanical Hamiltonian

In this thesis, I investigate a generic model of an optomechanical system consisting of a Fabry–Pérot cavity with two highly reflective mirrors positioned on opposite sides (refer to Fig. 2.1). One mirror is fixed in space, while the other mirror is free to move along the axis of the cavity. The system involves the coupling of one cavity mode with a resonance frequency ω_{c} to a mechanical mode with a resonance frequency ω_{m} through radiation pressure. By considering the limit of a large optical frequency (i.e. $\omega_{\mathrm{c}} \gg \omega_{\mathrm{m}}$), the scattering of photons and phonons into other modes can be neglected. As a result, the system Hamiltonian is given by[2]

$$H_{\mathrm{OM}} = \omega_{\mathrm{c}} a^\dagger a + \omega_{\mathrm{m}} b^\dagger b - g_0 a^\dagger a (b^\dagger + b) \,, \tag{2.6}$$

where $a, a^\dagger$ are the creation and annihilation operators for the optical mode, and $b, b^\dagger$ are the creation and annihilation operators for the mechanical mode, respectively. The parameter g_0 represents the

[2] In this thesis I work in the natural unit where $\hbar = 1$.

optomechanical coupling rate. The driving Hamiltonian reads

$$H_{\mathrm{d}} = \xi^*(t)a + \xi(t)a^\dagger \,, \tag{2.7}$$

where a complex-valued driving function $\xi(t)$ characterizes the frequency and any other time-dependence of the pumping of the cavity through an external light source, such as a temporal modulation. The temporal shape of the driving function $\xi(t)$ can be chosen with regular pulse-shaping techniques.

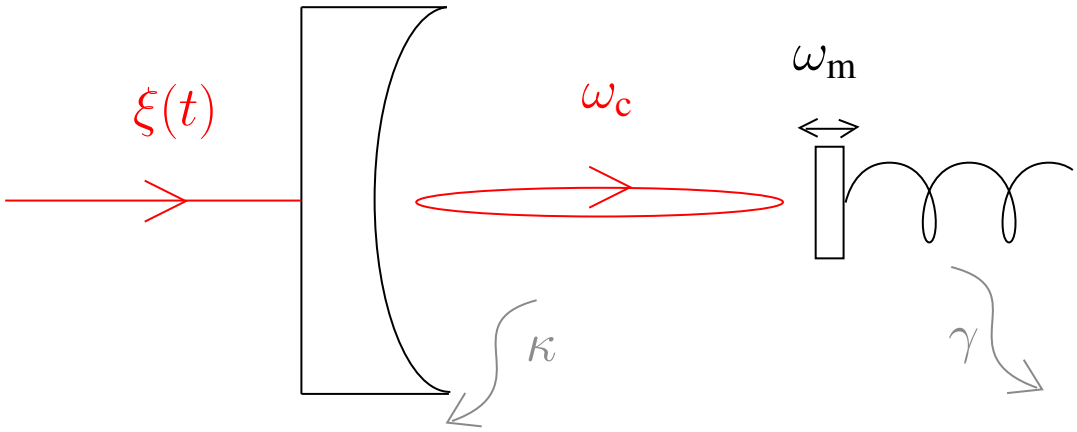


Figure 2.1: A schematic of the optomechanical system under consideration in this thesis. The system contains a Fabry–Pérot cavity consisting of one fixed mirror and one movable mirror. The cavity supports a single optical mode with resonance frequency ω_{c} and the movable mirror supports a single mechanical mode with resonance frequency ω_{m}. The coupling between the optical mode and the mechanical motion is achieved through radiation pressure, where the light field exerts a force on the movable mirror. Any optical pumping field with driving function $\xi(t)$ (see Eq. (2.7)) enters the cavity only through the fixed mirror to avoid undesired motion in the movable mirror. Both the optical and the mechanical degrees of freedom may suffer from dissipation at rate κ and γ respectively.

The interaction term in the Hamiltonian can be interpreted in two ways. Firstly, it accounts for the radiation pressure force that is proportional to the intensity of the light field (i.e. $\propto a^\dagger a$), which leads to a displacement in the mechanical oscillator. Secondly, it describes the shift in the optical resonance frequency, which is proportional to the displacement in the mechanical oscillator (i.e. $\propto b^\dagger + b$). By combining these two perspectives, it is natural to expect that an increase in the light intensity will result in a shift in the cavity resonance frequency proportional to the intensity increase, thus exhibiting the optical Kerr effect.

2.3.2 Polaron transform and energy level structure

To better understand the optical nonlinearity in optomechanical systems, it helps to diagonalize the system Hamiltonian in Eq. (2.6). This can be achieved by making the polaron transformation [29] defined by the unitary operator

$$U_{\mathrm{P}} = \exp\left(\frac{g_0}{\omega_{\mathrm{m}}} a^\dagger a (b^\dagger - b)\right) . \tag{2.8}$$

In this frame, the transformation of the photonic and phononic creation operators can be expressed as

$$\begin{aligned} U_{\mathrm{P}}^\dagger a^\dagger U_{\mathrm{P}} &= a^\dagger \exp\left(\frac{g_0}{\omega_{\mathrm{m}}}(b - b^\dagger)\right) , \\ U_{\mathrm{P}}^\dagger b^\dagger U_{\mathrm{P}} &= b^\dagger + \frac{g_0}{\omega_{\mathrm{m}}} a^\dagger a , \end{aligned} \tag{2.9}$$

which represent the creation of quasiparticles known as dressed photons and dressed phonons in the lab frame (i.e. in the frame of Eq. (2.6)). The system Hamiltonian $U_{\mathrm{P}}^\dagger H_{\mathrm{OM}} U_{\mathrm{P}}$ is diagonalized and is given by

$$\tilde{H}_{\mathrm{OM}} = \left(\omega_{\mathrm{c}} - \frac{g_0^2}{\omega_{\mathrm{m}}} a^\dagger a\right) a^\dagger a + \omega_{\mathrm{m}} b^\dagger b , \tag{2.10}$$

where the optomechanical interaction term has been replaced by a Kerr-type nonlinearity (i.e. $(a^\dagger a)^2$) in the optical subsystem.

The eigenstates of the transformed Hamiltonian $\tilde{H}_{\mathrm{OM}}$ are given by the direct product of Fock states in each subsystem. However, these Fock states in the polaron frame do not equate to the optical and the mechanical Fock states in the original frame. Specifically, a photonic excitation (i.e. $a^\dagger |0\rangle$) in the polaron frame corresponds to a dressed photon in the lab frame instead of a pure photon. This correspondence applies to dressed phonons as well. To avoid any potential confusion, in this section (Sec. 2.3), photonic and phononic excitations in the polaron frame are referred to as dressed photons and dressed phonons, respectively. Conversely, in the lab frame, they are denoted as physical photons and physical phonons. Such differentiation is pivotal for maintaining clarity in the subsequent analysis.

While the eigenstates exhibit different forms in the original and polaron frames, the unitarity of the polaron operator U_{P} in Eq. (2.8) ensures they share identical eigenvalues and thus identical energy

spectra. Consequently, the eigenvalues both Hamiltonians $\tilde{H}_{\mathrm{OM}}$ and H_{OM} are given by

$$E_{\mathrm{OM}}^{(n,m)} = n\left(\omega_{\mathrm{c}} - n\frac{g_0^2}{\omega_{\mathrm{m}}}\right) + m\omega_{\mathrm{m}} \,, \tag{2.11}$$

where n and m denote the number of dressed photons and dressed phonons respectively. Therefore, the transition energy from energy level $n = p, m = q$ to level $n = r, m = s$ is given by

$$T_{p,q\to r,s} = E_{\mathrm{OM}}^{(r,s)} - E_{\mathrm{OM}}^{(p,q)} = (r-p)\omega_{\mathrm{c}} - (r^2-p^2)\frac{g_0^2}{\omega_{\mathrm{m}}} + (s-q)\omega_{\mathrm{m}} \,. \tag{2.12}$$

Crucially for the generation of nonclassical optical states, the optical part of the spectrum is not evenly spaced (as depicted in Fig. 2.2, for example). In particular, when the system parameters satisfy the condition $\omega_{\mathrm{c}} \gg \omega_{\mathrm{m}} \gg g_0^2/\omega_{\mathrm{m}}$, the unequal energy structure provides a distinct advantage for the creation of Fock states of dressed photons. Because each dressed photon contains precisely one physical photon (i.e. $U_{\mathrm{P}}^{\dagger} a^{\dagger} U_{\mathrm{P}} \propto a^{\dagger}$), the generation of Fock states of physical photons within optomechanical systems is also enabled. For instance, a single-photon state can be generated due to the following logics: The transition frequency from a vacuum state to that containing a dressed photon is given by $T_{0,0\to1,0} = \omega_{\mathrm{c}} - g_0^2/\omega_{\mathrm{m}}$. In contrast, transitioning from a single-dressed-photon state to a two-dressed-photon state deviates from $T_{0,0\to1,0}$ by a frequency $\Delta T = 2g_0^2/\omega_{\mathrm{m}}$, which gives $T_{1,0\to2,0} = \omega_{\mathrm{c}} - 3g_0^2/\omega_{\mathrm{m}}$. Due to the large separation in the frequencies, the energy difference ΔT between the transitions can not be offset by the excitation of dressed phonons. Theoretically, it is possible to simultaneously pump n dressed photons into the cavity such that the energy offset

$$T_{0,0\to n,0} - nT_{0,0\to1,0} = (n^2-n)\frac{g_0^2}{\omega_{\mathrm{m}}} \tag{2.13}$$

can be compensated by the excitation of one dressed phonon. However, this high-order process occurs with inherently small amplitude, thereby causing minimal perturbation to the primary process (i.e. the excitation of a single dressed photon). Therefore, in an optomechanical system with parameters satisfying the condition $\Delta T \ll \omega_{\mathrm{m}}$, a driving field with frequency $\omega_{\mathrm{c}} - g_0^2/\omega_{\mathrm{m}}$ can pump one and only one photon into the cavity. Similarly, the preparation of a multi-photon state within the cavity becomes feasible by selecting a driving frequency $\omega_{\mathrm{d}} = T_{0,0\to n,0}/n = \omega_{\mathrm{c}} - ng_0^2/\omega_{\mathrm{m}}$. Suppression

of undesirable sidebands can be achieved whenever the energy offset $\Delta T = (n+1)g_0^2/\omega_\mathrm{m}$ for the excitation of one more dressed photon cannot be compensated by the excitation of dressed phonons.

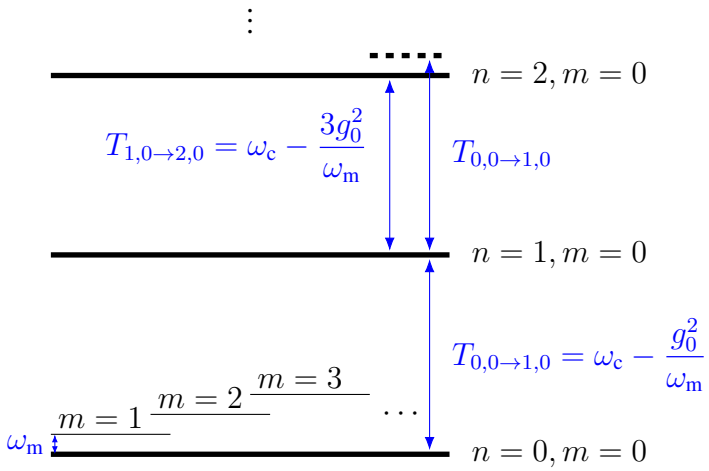


Figure 2.2: Schematic energy-level diagram of the optomechanical system in the polaron frame (refer to Eq. (2.10)). The thick solid lines represent the photonic energy levels (i.e. when $m = 0$), and the thin solid lines represent the energy substructures introduced by the polarons (i.e. when $m \neq 0$). The arrows indicate transition energies between different energy levels. The dashed thick line represents an artificial energy level that has a energy difference with the level $n = 1, m = 0$ equal to the energy difference between the level $n = 0, m = 0$ and the level $n = 1, m = 0$. This artificial level is forbidden in the optomechanical system whenever it does not overlap with any of the energy sublevels induced by polarons.

While the qualitative analysis offers valuable insight into the generation of photonic Fock states, the exact process reveals greater complexity. The following three factors contribute to this complexity. Firstly, the qualitative discussion presupposes operations within the polaron frame using pure optical driving, but in practical scenarios, pure optical driving is typically realized in the laboratory frame. Within the polaron frame, the Hamiltonian that delineates pure optical driving in the laboratory frame is given by:

$$U_\mathrm{P}^\dagger H_\mathrm{d} U_\mathrm{P} = \xi^*(t) a \exp\left(\frac{g_0}{\omega_\mathrm{m}}(b^\dagger - b)\right) + \xi(t) a^\dagger \exp\left(\frac{g_0}{\omega_\mathrm{m}}(b - b^\dagger)\right) . \tag{2.14}$$

In the transformed driving Hamiltonian, terms related to photon creation and annihilation are dressed with displacement of the mechanical degree of freedom. Therefore, a pure optical driving in the laboratory frame leads to simultaneous excitation and de-excitation of dressed photons and dressed phonons, thus permiting transitions that are otherwise forbidden as elaborated in Fig. 2.2.

Secondly, for the occupation of undesirable energy levels to be negligible, it is crucial that the energetic

violation significantly exceeds the driving amplitude (i.e., $2g_0^2/\omega_\mathrm{m} \gg \left|\xi(t)\right|$). However, such a low driving strength also leads to slow rate for the occupation of the desired energy level. This can pose challenges when the system experiences losses.

Last but not least, the discussion so far has assumed an idealized cavity with a perfectly sharp resonance frequency. However, in practical scenarios, engineering optomechanical cavities with linewidths κ that are significantly smaller than the optomechanical coupling strength g_0 presents considerable challenges [29, 84, 85]. The presence of non-negligible cavity linewidth can affect the suppression of otherwise energetically forbidden processes, and thus lead to an imperfect preparation of target states.

In summary, the appropriate scaling of optomechanical parameters (i.e., $\omega_\mathrm{c} \gg \omega_\mathrm{m} \gg g_0^2/\omega_\mathrm{m} \gg \left|\xi(t)\right|, \kappa$) and the effective suppression of phonon excitations are crucial for achieving high-quality optical Fock state generation in optomechanical systems. While currently still not achieved, the experimental realization of these conditions, as well as the development of schemes that can preserve state generation quality when some of the conditions are violated, can greatly facilitate advancements in this field.

2.4 Propagation of closed optomechanical systems

The dynamics of an undriven optomechanical system with Hamiltonian H_OM (refer to Eq. (2.6)) can be solved exactly [31, 113], and the corresponding propagator, assuming an initial time $t_0 = 0$, reads

$$\begin{aligned} U_\mathrm{OM}(t) = U_\mathrm{OM}(0,t) = &\exp\left(-i\omega_\mathrm{c} a^\dagger a t\right) \exp\left(i\frac{g_0^2}{\omega_\mathrm{m}^2}(a^\dagger a)^2\left(\omega_\mathrm{m} t - \sin(\omega_\mathrm{m} t)\right)\right) \times \\ &\times \exp\left(\frac{g_0}{\omega_\mathrm{m}}(1 - e^{-i\omega_\mathrm{m} t}) a^\dagger a b^\dagger - \mathrm{h.c.}\right) \exp\left(-i\omega_\mathrm{m} b^\dagger b t\right) . \end{aligned} \tag{2.15}$$

However, the interplay between the cubic interaction and the coherent driving presents a challenge to find an exact solution to the dynamics of the driven interacting system with Hamiltonian $H_\mathrm{tot} = H_\mathrm{OM} + H_\mathrm{d}$ (refer to Eq. (2.7)). Fortunately, benefiting from the relatively low frequency of the optomechanical coupling, perturbative techniques offer a viable approach to solve the system dynamics. In the subsequent sections, I introduce a perturbative method as outlined in reference [112].

2.4.1 Interaction picture

To take advantage of the slow optomechanical coupling, it is helpful to factorize the total evolution operator U_{tot}, induced by the Hamiltonian $H_{\text{tot}} = H_{\text{OM}} + H_{\text{d}}$ (refer to Eq. (2.6) and Eq. (2.7)), into the product of two components U_0 and U_{I}. The first component U_0 is induced by the Hamiltonian H_0 that can be solved exactly. The second component U_{I} is induced by a Hamiltonian H_{I} that can be solved perturbatively in the optomechanical coupling strength g_0 through techniques discussed in Sec. 2.2. The Schrödinger equation for the total evolution operator under this factorization is given by

$$\begin{aligned} i\frac{dU_{\text{tot}}(t)}{dt} =& i\frac{dU_0(t)}{dt}U_{\text{I}} + iU_0(t)\frac{dU_{\text{I}}(t)}{dt} \\ =& H_0(t)U_0(t)U_{\text{I}}(t) + U_0(t)H_I(t)U_{\text{I}}(t) \\ =& \left(H_0(t) + U_0(t)H_I(t)U_0^\dagger(t)\right)U_{\text{tot}}(t)\ . \end{aligned} \tag{2.16}$$

It can thus be deduced that the desired factorization of the total evolution operator can be achieved by decomposing the total Hamiltonian in to the form $H_{\text{tot}} = H_0 + U_0 H_I U_0^\dagger$, with

$$\begin{aligned} H_0(t) &= \omega_{\text{c}} a^\dagger a + \omega_{\text{m}} b^\dagger b + \xi^*(t)a + \xi(t)a^\dagger\ , \\ H_{\text{I}}(t) &= -U_0^\dagger(t) g_0 a^\dagger a (b^\dagger + b) U_0(t)\ , \end{aligned} \tag{2.17}$$

where the first component H_0 describes the non-interacting part of the system dynamics, and the Hamiltonian H_{I} is the optomechanical coupling term in the interaction picture defined by the evolution operator U_0.

The evolution operator U_0 for the non-interacting dynamics can be solved through the method of Lie algebra as [114, 115]

$$\begin{aligned} U_0(t) &= e^{i\zeta(t)} e^{-i\omega_{\text{c}} n_{\text{c}} t} e^{-i\omega_{\text{m}} n_{\text{m}} t} e^{f(t)a^\dagger - f^*(t)a}\ \text{, with} \\ f(t) &= \int_0^t e^{i\omega_{\text{c}}\tau}\xi(\tau)d\tau\ , \\ \zeta(t) &= \frac{1}{2}\int_0^t \left(e^{i\omega_{\text{c}}\tau}\xi(\tau)f^*(\tau) - h.c.\right)d\tau\ , \end{aligned} \tag{2.18}$$

where $n_{\text{c}} = a^\dagger a$ and $n_{\text{m}} = b^\dagger b$ represent the photonic and phononic number operators, respectively.

As a result, the interaction Hamiltonian H_I in Eq. (2.17) is given by

$$H_{\mathrm{I}}(t) = -g_0 \left(a^\dagger + f^*(t)\right) \left(a + f(t)\right) \left(be^{-i\omega_{\mathrm{m}}t} + b^\dagger e^{i\omega_{\mathrm{m}}t}\right) . \tag{2.19}$$

The perturbative solution to the evolution operator U_{I} induced by the Hamiltonian H_{I} is detailed in following sections.

2.4.2 Effective Hamiltonian

While a general solution of the evolution operator $U_{\mathrm{I}}(t)$ for an arbitrary time t can be constructed, the calculation process can be substantially simplified when the duration of the evolution is predetermined. Specifically, for the purpose of preparing nonclassical optical states, it is advantageous to choose a time interval that corresponds to an integer multiple of the mechanical oscillation period, denoted as $t = NT$, with $T = 2\pi/\omega_{\mathrm{m}}$ and N being a positive integer. The rationale behind this choice lies in the fact that the term proportional to $a^\dagger a b^\dagger$ in Eq. (2.15) equals to zero after each full mechanical period. Consequently, when there is no external driving, correlations between the mechanical oscillator and the light field vanish after each full mechanical period, in which case the preparation of pure optical states does not necessitate probabilistic protocols based on measurement results on the mechanical degree of freedom.

Because the generation of nonclassical states relies solely on the inherent nonlinearity in the optomechanical coupling (refer to Sec. 2.3.2), the total evolution time $t = NT$ has to be comparable to the inverse of the optomechanical coupling rate. Consequently, it is necessary to approximate the evolution operator using a truncated series, as detailed in Sec. 2.2. One natural choice of factorization reads

$$U_{\mathrm{I}}(0, NT) = U_{\mathrm{I}}((N-1)T, NT) \ldots U_{\mathrm{I}}(0, T) . \tag{2.20}$$

This factorization can be further simplified if the interaction Hamiltonian H_{I} exhibits periodicity after each full mechanical period. In such a scenario, the evolution operator U_{I} displays a translational symmetry, given by $U_{\mathrm{I}}(T, T+t) = U_{\mathrm{I}}(0, t)$ for any time t. Therefore, it is sufficient to approximate only the evolution operator $U_{\mathrm{I}}(T)$ as a function of the driving parameters, rather than obtaining the

complete set of evolution operators for each j in Eq. (2.20).

Given the factorization in Eq. (2.20), it is advantageous to employ the Magnus expansion (detailed in Sec. 2.2.2), which approximates the operator $U_{\mathrm{I}}(T)$ in the form of an exponential operator $\exp(-iH_{\mathrm{eff}}T)$, where the time-independent operator H_{eff} represents the effective Hamiltonian [116–118] (also known as the average Hamiltonian) over the time range $(0, T)$. This formulation enables the generation of the overall evolution operator over N mechanical periods through a compound effective Hamiltonian that can be calculated from the effective Hamiltonian over each period by recursively applying the Baker-Campbell-Hausdorff (BCH) formula [119]. The first few terms of the BCH formula are given below:

$$\log\left(e^{A}e^{B}\right) = A + B + \frac{1}{2}[A, B] + \frac{1}{12}([A, [A, B]] + [B, [B, A]]) + \dots \tag{2.21}$$

for arbitrary operators A and B. Such a technique of approximating the evolution over an longer interval by sequentially applying effective Hamiltonians over shorter durations is also known as Trotterization [120, 121].

Given that the effective Hamiltonians are preceded by a small constant (i.e. the optomechanical coupling g_0), high-order terms involving nested commutators can be effectively neglected. Consequently, it is possible to engineer a total effective Hamiltonian in such a way that undesirable terms in the effective Hamiltonian for each period cancel out to leading orders, while the terms corresponding to processes conducive to nonclassical optical states are maximized.

2.4.3 Perturbative expansion

In the reference [112], Magnus expansions of periodic evolution operators $U_{\mathrm{I}}(T)$ are presented and discussed for two distinct driving functions, namely $\xi_1(t)$ and $\xi_2(t)$, where ξ_j are defined as follows

$$\xi_j(t) = 2Ee^{-i(\omega_{\mathrm{c}}t-\psi)}\cos(j\omega_{\mathrm{m}}t)\ . \tag{2.22}$$

Both driving functions are bichromatic, with each component having an amplitude E and a temporal phase ψ. Notably, the two frequency components, $\omega_{\mathrm{c}} + j\omega_{\mathrm{m}}$ and $\omega_{\mathrm{c}} - j\omega_{\mathrm{m}}$, are oppositely detuned

from the optical resonance frequency by integer multiples of the mechanical frequency.

The detuned driving components induce the exchange of photons and phonons within the optomechanical system. For a driving field that is detuned by a single mechanical frequency, the mechanical oscillator must either provide or absorb one phonon for light to enter the cavity. Consequently, this driving pattern favors the first-order processes represented by $\int H_{\mathrm{I}} dt$ in Eq. (2.4), given that the interaction Hamiltonian H_{I} is proportional to the first-order operators b and $b^\dagger$ of the mechanical mode. Similarly, the doubly-detuned driving favors second-order processes, represented by $\mathcal{M}_2$ in Eq. (2.5).

The utilization of oppositely detuned components with equal driving amplitude serves the purpose of suppressing mechanical excitations, which, in the leading two orders, manifest as classical dynamics that can overshadow the desired nonclassical dynamics. While an intuitive interpretation is not provided, the claim of suppression can be justified through explicit calculations of the Magnus terms corresponding to mechanical excitation in each case. For a singly-detuned driving with a frequency of $\omega_{\mathrm{c}} \pm \omega_{\mathrm{m}}$, the first-order contribution contains terms $\pm 2 g_0 E^2 \pi (b + b^\dagger)/\omega_{\mathrm{m}}^3$. Similarly, for a doubly-detuned driving with a frequency of $\omega_{\mathrm{c}} \pm 2\omega_{\mathrm{m}}$, the second-order contribution consists of terms $\pm g_0^2 E^2 \pi (b^2 + (b^\dagger)^2)/(2\omega_{\mathrm{m}}^4)$. In both cases, mechanical excitation is supressed when the oppositely detuned components have equal amplitudes.

Unlike the driving amplitude, there is no necessity for the phases of the two components to be equal. Nonetheless, in practical terms, employing two driving components with distinct time-dependence of the phases may result in a more involved experimental setup, potentially introducing additional sources of errors. Furthermore, unequal phases reduce the effective amplitude of the composite driving field, resulting in a prolonged duration required to pump a photon into the cavity. Therefore, it is advisable to use equal phases for both driving components.

For the purpose of this thesis (as discussed in Sec. 3.2.1), the doubly-detuned driving ξ_2 holds particular relevance. Thus, the evolution operator derived in reference [112] is presented as follows for reference.

With the explicit driving profile outlined in Eq. (2.22), after each mechanical period $T = 2\pi/\omega_{\mathrm{m}}$, the

evolution operator U_0 reduces to an optical phase rotation operator

$$U_0(T) = \exp\left(-2i\pi\frac{\omega_\mathrm{c}}{\omega_\mathrm{m}}n_\mathrm{c}t\right) . \tag{2.23}$$

The first-order Magnus term $\mathcal{M}_1(T) = 0$ vanishes after each mechanical period. The second-order Magnus term can be written as

$$\begin{aligned}
\mathcal{M}_2(T) &= \pi\frac{g_0^2}{\omega_\mathrm{m}^2}(-\frac{29E^4}{60\omega_\mathrm{m}^4} + \mathcal{M}_2^\mathrm{C} + \mathcal{M}_2^\mathrm{I}) \text{ , with} \\
\mathcal{M}_2^\mathrm{C} &= -2n_\mathrm{c}^2 - \frac{4E^2}{3\omega_\mathrm{m}^2}n_\mathrm{c} + \frac{E^2}{3\omega_\mathrm{m}^2}(a^2e^{-2i\psi} + (a^\dagger)^2e^{2i\psi}) , \\
\mathcal{M}_2^\mathrm{I} &= -i\frac{E}{\omega_\mathrm{m}}(ae^{-i\psi} - a^\dagger e^{i\psi})\Big(b^2 + (b^\dagger)^2\Big) ,
\end{aligned} \tag{2.24}$$

where the operator $\mathcal{M}_2^\mathrm{C}$ represents purely optical processes, and the operator $\mathcal{M}_2^\mathrm{I}$ is an interaction term. The third order Magnus term contains a term $\mathcal{M}_3^\mathrm{M}$ representing purely mechanical processes, and an interaction term $\mathcal{M}_3^\mathrm{I}$, and can be written as

$$\begin{aligned}
\mathcal{M}_3(T) &= \pi\frac{g_0^3}{\omega_\mathrm{m}^3}(\mathcal{M}_3^\mathrm{M} + \mathcal{M}_3^\mathrm{I}) \text{ , with} \\
\mathcal{M}_3^\mathrm{M} &= \frac{4E^2}{3\omega_\mathrm{m}^2}\frac{\Big(b^\dagger + (2+\sqrt{3})b\Big)^3 + \Big(b + (2+\sqrt{3})b^\dagger\Big)^3}{27+15\sqrt{3}} , \\
\mathcal{M}_3^\mathrm{I} &= \mathcal{M}_{3,1}^\mathrm{I} + \mathcal{M}_{3,2}^\mathrm{I} + \mathcal{M}_{3,3}^\mathrm{I} ,
\end{aligned} \tag{2.25}$$

where

$$\begin{aligned}
\mathcal{M}_{3,1}^\mathrm{I} &= \left(\frac{12E^3}{5\omega_\mathrm{m}^3}\eta^3P_\mathrm{c} + \frac{7E}{3\omega_\mathrm{m}}(n_\mathrm{c}P_\mathrm{c} + P_\mathrm{c}n_\mathrm{c})\right)X_\mathrm{m} , \\
\mathcal{M}_{3,2}^\mathrm{I} &= i\frac{E}{\omega_\mathrm{m}}X_\mathrm{c}\frac{\Big(b^\dagger - (2+\sqrt{3})b\Big)^3 - \Big(b - (2+\sqrt{3})b^\dagger\Big)^3}{27+15\sqrt{3}} , \\
\mathcal{M}_{3,3}^\mathrm{I} &= 2i\frac{E^2}{\omega_\mathrm{m}^2}\Big((a^\dagger)^2e^{2i\psi} - a^2e^{-2i\psi}\Big)P_\mathrm{m} ,
\end{aligned} \tag{2.26}$$

and

$$\begin{aligned}
P_\mathrm{c} &= i(ae^{-i\psi} - a^\dagger e^{i\psi}), \quad X_\mathrm{c} = ae^{-i\psi} + a^\dagger e^{i\psi} , \\
P_\mathrm{m} &= i(b - b^\dagger), \qquad\qquad X_\mathrm{m} = b + b^\dagger .
\end{aligned} \tag{2.27}$$

The operators P and X represent the momentum and position operators for the mechanical operators $b^{(\dagger)}$ and optical phase-dependent operators $a^{(\dagger)}e^{(-)-i\psi}$, respectively.

While the Magnus terms $\mathcal{M}_2^{\mathrm{I}}$ and $\mathcal{M}_3^{\mathrm{I}}$ reveal intricate interactions between the mechanical and optical degrees of freedom, they are generally counterproductive to the generation of nonclassical states. Consequently, this thesis does not delve deeply into the physical significance of these terms. Instead, the primary focus lies in the design of optical driving schemes aimed at suppressing these processes, which is of paramount importance.

Furthermore, in reference [112], the term $\mathcal{M}_3^{\mathrm{M}}$ is identified as a valuable component for generating mechanical nonclassical states, while the term $\mathcal{M}_2^{\mathrm{C}}$ is deemed to induce unnecessary optical excitation that can potentially hinder the desired processes through higher-order interactions. Conversely, in the context of optical nonclassical state generation, the significance shifts, with $\mathcal{M}_2^{\mathrm{C}}$ assuming relevance while the term $\mathcal{M}_3^{\mathrm{M}}$ needs to be suppressed. A comprehensive discussion concerning the relationship between the Magnus terms and the generation of optical nonclassical states is provided in Sec. 3.2.2 and Sec. 3.2.3.

2.5 Propagation of open optomechanical systems

In Sec. 2.3.2, the significance of considering system loss for the preparation of nonclassical optical states has been highlighted. Additionally, exploring the emitted light from the optomechanical cavity can be insightful. Consequently, it is advisable to incorporate the system's interaction with the environment when modeling the optomechanical system. This section introduces two distinct approaches to open systems, one for analyzing the system's behavior in the presence of dissipation, and the other for examining the characteristics of the emitted light.

2.5.1 Lindblad master equation

One approach to modeling system dissipation is through the Lindblad master equation [122–124] for system density matrix ρ, which reads as

$$\begin{aligned} \dot{\rho} &= -i[H,\rho] + \sum_i \mathcal{D}[L_i]\rho \ , \text{ with} \\ \mathcal{D}[L_i]\rho &= \frac{1}{2}\left(2L_i\rho L_i^\dagger - L_i^\dagger L_i\rho - \rho L_i^\dagger L_i\right) \ , \end{aligned} \tag{2.28}$$

where the Hamiltonian H, the dissipation rates γ_i, and the Lindblad operators L_i depend on the specific model of the dissipative system. The master equation models the dissipative dynamics of a system by tracing out the environment degrees of freedom. Thus, compared to a full model that encompasses an infinite number of modes in an environment, a master equation typically offers a more concise and practical solution in terms of both theoretical analysis and numerical simulations of the system alone. Although the master equation has assumptions that may limit its applicability in certain scenarios, it is noteworthy that optomechanical experiments typically fulfill these criteria [29]. The key assumptions are as follows:

- **The model:** The composite system (denoted by ρ_{tot}) of environment and the dissipative system is modeled by the system under consideration (denoted by ρ_{sys}) surrounded by a heat bath (denoted by ρ_{bath}).

- **Stationary environment:** The heat bath is significantly larger than the system under consideration, such that the state of the environment remains unaltered by the perturbation from the system throughout the entire evolution, i.e. $\rho_{\text{bath}}(t) = \rho_{\text{bath}}(0)$.

- **Initial state separability:** The system under consideration and the environmental degree of freedom are initially independent, i.e. $\rho_{\text{tot}}(0) = \rho_{\text{sys}}(0) \otimes \rho_{\text{bath}}$.

- **Weak coupling:** The coupling between the system and the environmental degree of freedom is weak, ensuring that the composite system remains separable throughout the evolution (i.e. $\rho_{\text{tot}}(t) = \rho_{\text{sys}}(t) \otimes \rho_{\text{bath}}$).

- **Markov Assumption:** The system relaxation time (inverse of the system decay rate) is much longer than the bath correlation time (inverse of the system resonance frequency). Consequently, any information emitted from the system to the environment immediately vanishes, and thus the future states of the system under consideration only depends on the current system state, but not the past states.

- **Rotating-wave approximation:** Processes that are far off resonance with the system (fast-oscillating processes) are negligible and have no impact on the system dynamics.

A study of the validity of these approximations can be found, for example, in the reference [125].

For a dissipative quantum harmonic oscillator described by the Hamiltonian $H = \omega c^\dagger c$ interacting with a thermal bath characterized by an average occupation number $\bar{n}_\mathrm{b}$ at constant rate κ, the corresponding Lindblad operators simplify to $L_1 = \sqrt{\kappa(\bar{n}_\mathrm{b}+1)}c$ and $L_2 = \sqrt{\kappa\bar{n}_\mathrm{b}}c^\dagger$ [125, 126]. These two Lindblad operators represent single-boson emission and absorption in the system, resulting in energy exchange and thermalization of the oscillator. The optomechanical system under consideration in this thesis consists of two coupled harmonic oscillators. To simplify the discussion, it is usually assumed that each oscillator is coupled to its own distinct heat bath [29]. Furthermore, due to the typically negligible light-matter interaction in free space, the interaction between these baths occurs solely through the optomechanical coupling. Consequently, in the limit of weak optomechanical coupling (i.e. $g_0 \ll \kappa, \gamma$), the master equation governing its dynamics can be expressed as:

$$\dot{\rho} = i[H_\mathrm{OM} + H_\mathrm{d}, \rho] + \left(\mathcal{D}[\sqrt{\kappa}a] + \mathcal{D}[\sqrt{\gamma(\bar{n}_\mathrm{b}+1)}b] + \mathcal{D}[\sqrt{\gamma\bar{n}_\mathrm{b}}b^\dagger]\right)\rho \tag{2.29}$$

when the system is coupled to a thermal bath with zero photon and an average of $\bar{n}_\mathrm{b}$ phonons.

However, in the strong coupling regime, the dissipation of the two subsystems cannot be considered as independent events. Specifically, when the coupling rate becomes comparable to the mechanical frequency, the mechanical oscillator experiences significant perturbations from the optical field, causing it to deviate from the characteristics of a quantum harmonic oscillator. In such instances, it becomes

necessary to instead adopt the dressed-state master equation [127]:

$$\dot{\rho} = -i[H_{\mathrm{OM}} + H_{\mathrm{d}}, \rho] + \sum_{j=1}^{4} \mathcal{D}_j \rho \,, \tag{2.30}$$

where

$$\begin{aligned}
\mathcal{D}_1 =& \mathcal{D}[\sqrt{\kappa} a] \,, \\
\mathcal{D}_2 =& \mathcal{D}\left[\sqrt{\gamma(\bar{n}_{\mathrm{b}} + 1)}\left(b - \frac{g_0}{\omega_{\mathrm{m}}} a^\dagger a\right)\right] \,, \\
\mathcal{D}_3 =& \mathcal{D}\left[\sqrt{\gamma \bar{n}_{\mathrm{b}}}\left((b^\dagger - \frac{g_0}{\omega_{\mathrm{m}}} a^\dagger a\right)\right] \,, \\
\mathcal{D}_4 =& \mathcal{D}\left[\sqrt{\frac{4\gamma g_0^2}{\omega_{\mathrm{m}}^3}} a^\dagger a\right] \,,
\end{aligned} \tag{2.31}$$

with T_{b} representing the temperature of the thermal bath, and k_{B} being the Boltzmann constant. The temperature T_{b} and the bath occupation number $\bar{n}_{\mathrm{b}}$ can be related by the equation

$$\bar{n}_{\mathrm{b}} = \frac{1}{\exp\left(\frac{\omega_{\mathrm{m}}}{k_{\mathrm{B}} T_{\mathrm{b}}}\right) - 1} \,. \tag{2.32}$$

While the single-photon dissipation remains unaltered, the single-phonon dissipation in Eq. (2.29) is subject to a first-order (i.e. $\propto g_0$) shift proportional to the photon number. Moreover, a term representing a second-order effect (i.e. $\propto g_0^2$) emerges, accounting for dephasing of the optical field at a rate proportional to the temperature of the mechanical thermal bath. The inclusion of these first- and second-order effects introduces numerical discrepancies compared to the standard master equation in Eq. (2.29), particularly when the coupling strength is approximately on the same order of magnitude as the mechanical frequency [128].

Lastly, it is worth mentioning that the dressed-state master equation can also lead to unphysical predictions as the coupling strength increases. In such cases, it is advisable to extend the master equation further to incorporate the non-local effects of the optical dissipator [129]. However, it is important to note that in the majority of experimental studies of optomechanics, the optical frequency is considerably larger than all other frequencies in the Hamiltonian in Eq. (2.6). Therefore, the standard master equation in Eq. (2.29) and the dressed-state master equation in Eq. (2.30) adequately capture

the relevant dynamics for the scope of this thesis.

2.5.2 Input-output formalism and cascaded system

In addition to the Lindblad master equation, the quantum Langevin equation (discussed below) serves as a valuable tool for effectively capturing the dynamics of open systems [130]. Unlike the master equation approach, the quantum Langevin equation explicitly incorporates the environmental degrees of freedom. Consequently, solving the Langevin equation numerically is generally more challenging due to the involvement of numerous bath modes. However, it offers a pathway for analyzing the emission field of the system into the heat bath.

Similar to the case of the master equation, the Langevin equation presented in Eq. (2.33) is also subject to several assumptions. The key assumptions are as follows:

- **The model:** The composite system consists of a heat bath that is coupled to the dissipative system of interest. The heat bath comprises a continuum of mutually uncoupled quantum harmonic oscillators spanning frequencies from 0 to infinity. The bath encompasses all relevant physical effects, rendering the total system closed.

- **Linear coupling:** The coupling between the dissipative system and the bath is linear in the position quadrature of the system and the momentum quadrature of the bath[3].

- **Rotating-wave approximation:** Processes that are far off resonance with the system are negligible and have no impact on the system dynamics.

- **Flat coupling:** The coupling strength between the system and the heat bath is assumed to be constant in the vicinity of the resonance frequency of the system. This assumption is also referred to as first Markov approximation because it is necessary for ensuring that the final form of the quantum Langevin equation is independent of the system operators in the past.

[3]Technically, any linear coupling between the quadrature observables of the system and the heat bath modes is allowed as long as all bath modes are consistently coupled to the same quadrature of the system. This may introduce a phase in the Langevin equation, representing the phase of the laboratory frame, without altering the underlying physics.

In general, Langevin equations are commonly formulated in the Heisenberg picture, which assumes that operators evolve with time while the states remain time-independent. Therefore, for the purpose of this section, I adopt the Heisenberg picture as the framework of reference. For an optomechanical system that interacts with mutually uncoupled photonic and phononic heat baths, the quantum Langevin equation for any system operator c can be expressed as:

$$\begin{aligned}\dot{c} = &-i[c, H_{\mathrm{OM}}] + \frac{\kappa}{2}\left(2a^\dagger c a - a^\dagger a c - c a^\dagger a\right) + \frac{\gamma}{2}\left(2b^\dagger c b - b^\dagger b c - c b^\dagger b\right) + \\ &+ \sqrt{\kappa}\left(a_{\mathrm{in}}^\dagger [c, a] - [c, a^\dagger] a_{\mathrm{in}}\right) + \sqrt{\gamma}\left(b_{\mathrm{in}}^\dagger [c, b] - [c, b^\dagger] b_{\mathrm{in}}\right) ,\end{aligned} \tag{2.33}$$

The first term on the right hand side of Eq. (2.33) corresponds precisely to the Heisenberg equation of motion for closed systems. The second (third) term represents a single-photon (single-phonon) dissipation that resembles the Lindblad operators $\mathcal{D}[\sqrt{\kappa}a]$ ($\mathcal{D}[\sqrt{\kappa}b]$) in the master equation. The last two terms proportional to the input operators a_{in} and b_{in} account for the entry of any bosonic field or quantum fluctuation into the system, which is traced out in the Lindbladian approach. These additional input terms form a crucial distinction between the Langevin equation and the master equation, providing a method to solve for the output fields (a_{out} and b_{out}) using the input-output equation:

$$a_{\mathrm{out}} = \sqrt{\kappa}a + a_{\mathrm{in}} , \qquad b_{\mathrm{out}} = \sqrt{\gamma}b + b_{\mathrm{in}} , \tag{2.34}$$

When the Langevin equation in Eq. (2.33) can be solved exactly, such as through linearization [41], the solution to the Langevin equation in conjunction with the input-output equation provide a means to compute various output statistics, including the emission intensity $n_{\mathrm{out}} = \langle a_{\mathrm{out}}^\dagger a_{\mathrm{out}} \rangle$. However, when the focus shifts to quantum effects, where linearization of the Langevin equation is not feasible, finding a solution becomes significantly more challenging. One approach to address this challenge is to first solve the system dynamics using the master equation approach and subsequently compute the system output based on the obtained solution. Nonetheless, a subtlety arises because the master equation (which traces out the bath) and the Langevin equation (which includes the bath) operate in different Hilbert spaces, which poses challenges when performing actual calculations.

An alternative approach to studying the output field is to model the system and the emitted field together as a cascaded system [131]. Figure 2.3 depicts a scheme of a simple cascaded system containing two

components. In this configuration, the output field of the first component (System 1) is directed into the second component (System 2) in a one-way manner, such that the backaction of the second component on the first component is neglected. Mathematically, this can be expressed as the equation

$$a_{2,\text{in}} = a_{1,\text{out}} = a_{1,\text{in}} + \sqrt{\kappa_1} a_1 \ , \tag{2.35}$$

where a_1 (a_2), κ_1 (κ_1), $a_{1,\text{in}}$ ($a_{2,\text{in}}$), $a_{1,\text{out}}$ ($a_{2,\text{out}}$) represent the annihilation operator, the decay rate, the input operator, and the output operator of the first (second) system, respectively. The Langevin equation for any operator c of the composite system is thus given by

$$\begin{aligned}
\dot{c} =& -i[c, H_1 + H_2] + \sum_{j=1,2} \frac{\kappa_j}{2} \left(2a_j^\dagger c a_j - a_j^\dagger a_j c - c a_j^\dagger a_j \right) + \sum_{j=1,2} \sqrt{\kappa_j} \left(a_{j,\text{in}}^\dagger [c, a_j] - [c, a_j^\dagger] a_{j,\text{in}} \right) \ , \\
=& -i[c, H_1 + H_2] + \sum_{j=1,2} \frac{\kappa_j}{2} \left(2a_j^\dagger c a_j - a_j^\dagger a_j c - c a_j^\dagger a_j \right) + \\
&+ \sqrt{\kappa_1} \left(a_{1,\text{in}}^\dagger [c, a_1] - [c, a_1^\dagger] a_{1,\text{in}} \right) + \sqrt{\kappa_2} \left((a_{1,\text{in}}^\dagger + \sqrt{\kappa_1} a_1^\dagger)[c, a_2] - [c, a_2^\dagger](a_{1,\text{in}} + \sqrt{\kappa_1} a_1) \right) \ .
\end{aligned} \tag{2.36}$$

It is worth noting that for any operator c_1 of the first system (i.e. when $[c_1, a_2] = [c_1, a_2^\dagger] = 0$), the Langevin equation for the cascaded system reduces to the Langevin equation for the first system alone. However, the evolution of the operators of the second system always depends on the first system, which aligns with the concept of one-way coupling.

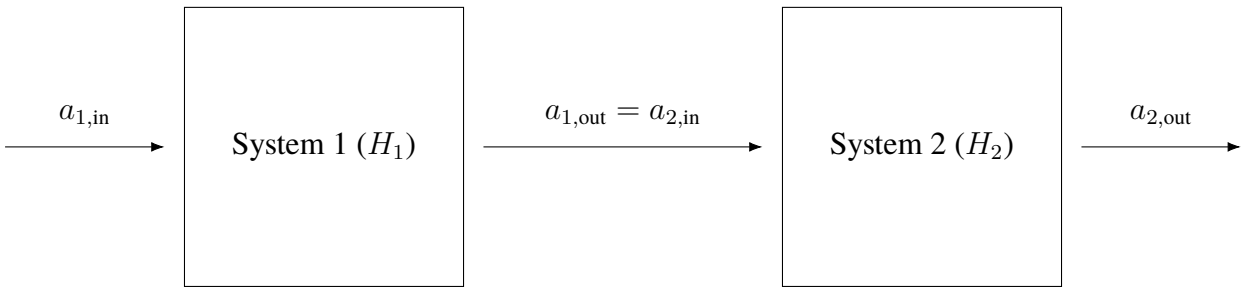


Figure 2.3: A schematic of a cacaded system containing two components. The output field of the first system is directed into the second system.

While the Langevin equation in Eq. (2.36) remains unsolvable through numerical tools due to the presence of the infinite-dimensional input operator $a_{1,\text{in}}$, it is possible to derive a corresponding master equation (in the Schrödinger picture) for the cascaded system. A comprehensive tutorial for the general case can be found, for example, in reference [132], but this thesis focuses specifically on the case where

the heat bath can be modeled by a vacuum state. In such case, the master equation of the cascaded system reads

$$\dot{\rho} = -i[H_1 + H_2, \rho] + \sum_{j=1,2} \frac{\kappa_j}{2} \left(2a_j \rho a_j^\dagger - a_j^\dagger a_j \rho - \rho a_j^\dagger a_j\right) + \sqrt{\kappa_1 \kappa_2} \left([a_2, \rho a_1^\dagger] - [a_2^\dagger, a_1 \rho]\right) . \tag{2.37}$$

The output state from the first system can thus be obtained by solving the master equation for the composite system and subsequently tracing out the degree of freedom associated with the first system.

2.6 Photon blockade and autocorrelation

In analogy with the Coulomb blockade of electrons, the photon blockade effect occurs if a single photon in a cavity provides an energetic barrier for a second photon to enter the cavity. As such, a driven-dissipative cavity exhibiting photon blockade can be viewed as a photon turnstile. Therefore, a cavity exhibiting photon blockade can serve as a potential single-photon source which is an important resource in many fields, including quantum computation [133, 134] and quantum communication [135]. The photon blockade phenomenon has been investigated within various platforms, such as Kerr-type nonlinear cavity [136, 137], cavity-quantum-electrodynamics systems [138–141], superconducting circuits [142–144] and optomechanical systems [43, 145, 146].

In order to effectively study the photon blockade effect, it is helpful to identify a quantifier for its strength. Quantum states of light can generally be characterized in terms of correlation functions $\langle A(t+\tau)B(t)\rangle$, where τ denotes the time-delay between the points in time at which the observables A and B are measured. In the context of the photon blockade, one is interested in the probability to find a second photon, immediately after the first photon has been detected. It is thus necessary to employ equal-time correlation functions with $\tau = 0$.

A suitable, and commonly used figure of merit is the equal-time second-order autocorrelation function, which is given by

$$g^{(2)}(t) = \frac{\langle \hat{n}^2 \rangle - \langle \hat{n} \rangle}{\langle \hat{n} \rangle^2} , \tag{2.38}$$

with the photon-number operator $n = a^\dagger a$ and the expectation operator $\langle \cdot \rangle$ with respect to the system

state $\rho(t)$. The autocorrelation function $g^{(2)}(t)$ vanishes exactly if there is at most a single photon in the system at time t, and a low value of $g^{(2)}(t)$ is thus a good indication of strong photon blockade.

Despite its simple form, the time evolution of the autocorrelation function is not easy to analytically determine for optomechanical systems. This is because the system dynamics cannot be solved exactly due to the cubic interaction term. To address the problem, it is helpful to consider the photon blockade effect in a perturbative regime in which the occupation probability of Fock states containing three or more photons is negligible as compared to the single-photon and two-photon occupations. When such higher-photon occupations are suppressed, the autocorrelation function in Eq. (2.38) can be expressed as

$$g^{(2)}(t) \approx \frac{2p_2(t)}{(p_1(t) + 2p_2(t))^2} := \tilde{g}^{(2)}(t) \,, \tag{2.39}$$

in terms of the occupation probabilities $p_1(t)$ and $p_2(t)$ of the single- and two-photon Fock state respectively.

Chapter 3

Nonclassical light in dissipationless optomechanical systems

The material presented in this chapter stems from research I undertook at Imperial College and draws inspiration from the work of my colleague, Ludovico Latmiral [112]. Specifically, the fundamental methodology detailed in Sec. 3.2.2 was initially introduced in [112]. The application of this methodology to generate optical nonclassical states, along with the main discussions in this chapter, form the core content of a paper published in Physical Review Research with the title "Deterministic preparation of nonclassical states of light in cavity optomechanics" [147].

3.1 Introduction

In Sec. 2.3, the intrinsic anharmonicity of optomechanical systems has been extensively discussed, highlighting their significant potential for generating quantum states of light. It is pointed out that the suppression of mechanical excitation is among the major challenges in achieving high-quality nonclassical light. One approach to address this issue involves driving the system with a weak light field, thereby ensuring that undesired processes occur at an arbitrarily low amplitude. Nevertheless, this resolution unavoidably results in a long preparation time for the target states, making it susceptible to system dissipation.

In this chapter, an alternative solution is proposed. Through the implementation of optimal driving techniques, effective suppression of both the mechanical excitation and the light-matter correlation to leading orders is demonstrated. Importantly, this suppression is independent of the driving amplitude, enabling the utilization of larger amplitudes that surpass the optomechanical coupling strength. Consequently, it becomes feasible to deterministically prepare close-to-pure, nonclassical light within a significantly shorter timeframe. To exemplify the efficacy of the approach, I showcase the generation of two-photon Fock states as well as the coherent superposition of these states with the vacuum state.

In the first stage, the driving profile is designed based on the assumption of an ideal scenario, where the mechanical oscillator is initially in its ground state and the dissipation in the system is considered to be negligible. Subsequently, a numerical analysis is conducted to investigate the robustness of the prepared states in the presence of system imperfections. This analysis takes into account three key factors: a initial non-vacuum thermal state of the mechanical oscillator, optical dissipation and mechanical thermalization that occur during the evolution of the system. By considering these factors separately, the assessment allows for a comprehensive evaluation of the practical applicability of the proposed scheme in realistic settings.

This chapter is structured as follows. In Sec. 3.2, the theoretical design of the driving profile is presented. In particular, Sec. 3.2.1 is devoted to the choice of the fundamental driving profile, but allows for flexibility in the temporal variation of the free parameters within the driving function. Subsequently, in Sec. 3.2.2 and Sec. 3.2.3, the driving parameters are optimized using the Magnus solution (as described in Sec. 2.2.2), aiming to achieve an optimal effective Hamiltonian for target state generation up to second and third order in the perturbation parameter, respectively. The resulting driving pattern is summarized in Sec. 3.2.4. Next, in Sec. 3.3, the optimized driving pattern is verified numerically for the generation of a two-photon Fock state (in Sec. 3.3.1) and its superposition state with the vacuum state (in Sec. 3.3.2). Finally, in Sec. 3.5, the robustness of the results obtained in the presence of system imperfections is examined.

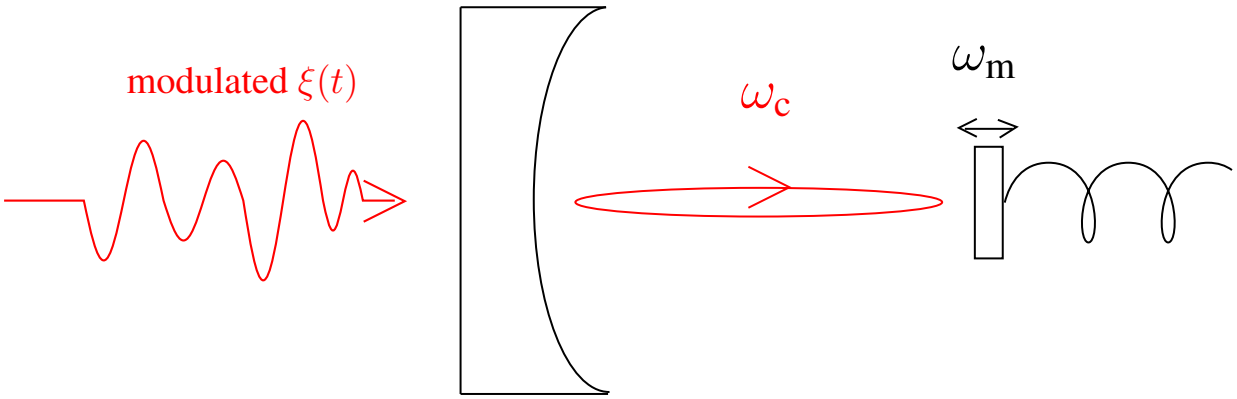


Figure 3.1: A schematic of the optomechanical system under consideration in this Chapter. The optomechanical system is driven by a temporally modulated, coherent light field. The cavity and the mechanical dissipation are neglected when design optimal driving.

3.2 Design of optimal driving

In this section, a generic type of optomechanical system as depicted in Fig. 3.1 is considered. The total Hamiltonian for the driven system is given by the sum $H_{\mathrm{OM}} + H_{\mathrm{d}}$ with the bare system Hamiltonian H_{OM} and the driving Hamiltonian H_{d} defined as[1]

$$\begin{aligned} H_{\mathrm{OM}} =& \omega_{\mathrm{c}} a^\dagger a + \omega_{\mathrm{m}} b^\dagger b - g_0 a^\dagger a (b^\dagger + b) \\ H_{\mathrm{d}} =& \xi^*(t) a + \xi(t) a^\dagger \end{aligned} \tag{3.1}$$

The scalar driving function $\xi(t)$ in the driving Hamiltonian H_{d} is flexible and can be chosen accordingly.

The dynamics of the non-dissipative part of the system are described by the evolution operator $U_{\mathrm{tot}}(t)$, which satisfies the equation $i\dot{U}_{\mathrm{tot}} = (H_{\mathrm{OM}} + H_{\mathrm{d}})U_{\mathrm{tot}}$. The subsequent part of this section focuses on designing the driving function $\xi(t)$ such that, after a specific duration t_{f}, the evolution operator reduces to $U_{\mathrm{tot}}(t_{\mathrm{f}}) \approx U_{\mathrm{c}} \otimes \mathbb{1}_{\mathrm{m}}$. In this evolution, the optical state evolves to the desired target state following the effective evolution operator $U\mathrm{c}$, while the mechanical state undergoes a trivial identity evolution denoted by $\mathbb{1}_{\mathrm{m}}$.

[1] The definitions are the same as in Eq. (2.6) and Eq. (2.7), but copied for readers' convenience.

3.2.1 Driving profiles

The range of states achievable strongly depends on the chosen driving profile $\xi(t)$. In particular, more complicated driving can modify the system dynamics with greater potential for state preparation. However, it is important to note that such complex driving profiles often necessitate more intricate experimental setups, thereby increasing the system's vulnerability to errors in the components. Hence, for the purposes of subsequent discussions, it is preferable to employ a driving profile with a sufficiently simple spectrum. This choice aims to strike a balance between system flexibility and experimental robustness.

Suitable driving profiles can be determined based on the fundamental properties of the optomechanical interaction, described by $a^\dagger a(b^\dagger + b)$. This interaction couples the absorption and emission of a phonon to the photon number operator $n_\mathrm{c} = a^\dagger a$. The first-order interaction process only involves a photon number operator that does not contribute to the creation of nonclassicality. Hence, it will not be helpful to use driving that supports the absorption and emission of single phonons. On the other hand, as discussed in Sec. 2.3.2, the second-order processes introduce an effective optical Kerr-like nonlinearity ($\propto n_\mathrm{c}^2$), which enables the generation of nonclassical light. Consequently, a driving profile that promotes the absorption and emission of phonon pairs is preferred to attain nonclassical effects in the optical cavity.

A simple yet effective driving profile that satisfies the given criterion is represented by the equation

$$\xi(t) = e^{-i\omega_\mathrm{c} t}\left(E_1 e^{i(2\omega_\mathrm{m} t+\psi_1)} + E_2 e^{i(-2\omega_\mathrm{m} t+\psi_2)}\right) \tag{3.2}$$

with a positively detuned component and a negatively detuned component. Both components are detuned from the optical resonance frequency ω_c that amount to twice the mechanical frequency ω_m. The parameters E_1 and E_2 represent real-valued amplitudes of the two oppositely detuned components, while ψ_1 and ψ_2 represent their respective phases with respect to the laboratory frame.

Although the driving function in Eq. (3.2) favors the desired processes, it also results in excitations in the mechanical oscillator and introduces unnecessary sources of experimental errors, as discussed in Sec. 2.4.3. Therefore, it is desirable to adopt a balanced driving with equal amplitude and phase (i.e.

$E_1 = E_2$ and $\psi_1 = \psi_2$) such that the driving function reads

$$\xi(t) = Ee^{-i(\omega_c t - \psi)} \left(e^{2i\omega_m t} + e^{-2i\omega_m t} \right) . \tag{3.3}$$

The real-valued amplitude E and phase ψ are not determined yet, and the freedom to choose these parameters will be utilized for the design of suitable driving patterns.

3.2.2 Effective Hamiltonian to second order

The dynamics of the driven-interacting system cannot be solved exactly due to the cubic nature of the interaction. Nevertheless, by transforming into the interaction picture, it becomes possible to perturbatively solve the system dynamics, as discussed in Sec. 2.4.

Since the cavity frequency ω_c is experimentally determined by the length of the optomechanical cavity, which is a tunable parameter, one can take ω_c to be an integer multiple of ω_m. In this case, the propagator of non-interacting system[2]

$$U_0(t) = e^{i\zeta(t)} e^{-i\omega_c n_c t} e^{-i\omega_m n_m t} e^{f(t)a^\dagger - f^*(t)a} \tag{3.4}$$

is periodic with a period $T = 2\pi/\omega_m$ equal to the mechanical period. Furthermore, when the driving parameters are changed only after integer multiples of mechanical periods, the evolution operator U_I induced by the interaction Hamiltonian[3]

$$H_I(t) = -g_0 \left(a^\dagger + f^*(t) \right) \left(a + f(t) \right) \left(be^{-i\omega_m t} + b^\dagger e^{i\omega_m t} \right) \tag{3.5}$$

becomes periodic with period T. The total propagator of the system can thus be characterized as the product of the evolution operators $\exp\left(-iH_{e,j}T\right)$ with the Hamiltonian $H_{e,j}$ defined solely by the driving profile of the current period (refer to Sec. 2.4.2). This simplification of the total propagator facilitates the preparation of the target state via the optimization of driving functions.

[2] The equation is the same as defined in in Eq. (2.18), but copied here for readers' convenience.
[3] The same as defined in Eq. (2.19).

Following the perturbative solutions presented in Sec. 2.4.3, after each complete mechanical period, the propagator $U_{\mathrm{I}}(t)$ induced by the interaction Hamiltonian can be expressed as $\exp\bigl(-i\mathcal{M}_2(T)\bigr)$ up to the second order in the optomechanical coupling strength g_0. The Magnus term $\mathcal{M}_2(T)$ defined in Eq. (2.24) comprises a global phase $\propto E^4$, a cavity operator $\mathcal{M}_2^{\mathrm{C}}$, and an interaction operator $\mathcal{M}_2^{\mathrm{I}}$. For the purpose of generating nonclassical states, the global phase is considered irrelevant and hence disregarded in the subsequent discussion.

The cavity operator $\mathcal{M}_2^{\mathrm{C}}$ contains several terms that are very useful for the generation of nonclassical states. The terms $(a^\dagger)^2$ and a^2 describe the creation and annihilation of pairs of photons. The quartic operator n_{c}^2 results in a deviation from the evenly spaced level structure of the quantum harmonic oscillator. The effectively larger spacing between higher lying levels enables the population of the two-photon Fock state from the vacuum state. Simultaneously, it ensures that the population of the four-photon Fock state and higher-lying states are far off-resonant and negligible.

On the other hand, in second order there are also processes that can impede the generation of non-Gaussian states. The term linear in n_{c} that is contained in the cavity operator $\mathcal{M}_2^{\mathrm{C}}$ increases the constant spacing between energy levels of the quantum harmonic oscillator and thus reduces the effective anharmonicity resulting from the n_{c}^2 term. Furthermore, the interaction term $\mathcal{M}_2^{\mathrm{I}}$ results in correlations between the cavity and the mechanical oscillator to build up.

With the driving profile specified in Eq. (3.3), it is not possible to have these undesired terms vanish without also having terms describing the creation and annihilation of pairs of photons vanish. Consequently, the objective of the forthcoming analysis is to devise a series of driven and undriven intervals, where the effective Hamiltonian, denoted as H_{f}, governing the dynamics across these intervals incorporates the desired terms while excluding the undesired processes.

The dynamics of each period of driven dynamics is characterized in terms of an effective Hamiltonian

$$H_{\mathrm{e}} = \frac{\mathcal{M}_2(T)}{T}\,, \tag{3.6}$$

but since the driving can vary from period to period, there is a distinct effective Hamiltonian for each period. These individual effective Hamiltonians serves as starting point for constructing an overall

effective Hamiltonian, denoted as H_{f}, which captures the dynamics of multiple periods of driven dynamics. In general, constructing H_{f} requires accounting for the non-commutativity of the involved operators, necessitating the use of the BCH series in Eq. (2.21). However, given the specific driving profile in Eq. (3.2), the leading contribution to the individual effective Hamiltonian is of order $g_0^2/\omega_{\mathrm{m}}^2$. Consequently, the first non-trivial contribution to the Baker-Campbell-Hausdorff series, which appears at order $g_0^4/\omega_{\mathrm{m}}^4$, is smaller than the highest order (i.e. $g_0^2/\omega_{\mathrm{m}}^2$) already included in the individual effective Hamiltonians, as well as smaller than the highest order (i.e. $g_0^3/\omega_{\mathrm{m}}^3$) to be included later-on. Therefore, within the desired level of accuracy, the complete effective Hamiltonian H_{f} is given by the sum of individual effective Hamiltonians H_{e} over each mechanical period.

The interaction term $\mathcal{M}_2^{\mathrm{I}}$ in Eq. (2.24) depends on the phase ψ of the driving field defined in Eq. (3.2), via the momentum operator $P_{\mathrm{c}}(\psi)$ given in Eq. (2.27). After N periods of driven dynamics, where each of the j-th period is characterized by a constant driving strength E_j and constant phase ψ_j, the interaction term in the full effective Hamiltonian H_{f} thus becomes proportional to the sum $\sum_{j=1}^{N} E_j P_{\mathrm{c}}(\psi_j)$. As a result, any sequence of driving periods satisfying the condition $\sum_{j=1}^{N} E_j \exp\left(i\psi_j\right) = 0$ ensures that there are no interaction effects up to the second order at the end of the dynamics.

On the other hand, the creation and annihilation of pairs of photons in the optical term $\mathcal{M}_2^{\mathrm{C}}$ depend on the driving field via $E^2 \exp(\pm 2i\psi)$. Therefore, it is desirable to identify choices for the driving fields that maximize $\sum_j^N E_j^2 \exp\left(2i\psi_j\right)$ under the constraint $\sum_j^N E_j \exp\left(i\psi_j\right) = 0$. To leading order, this prescription results in an effective Hamiltonian over N mechanical periods given by

$$H_{\mathrm{f}} = \frac{1}{T}\sum_{j=1}^{N} \mathcal{M}_2^{\mathrm{C}}(E_j, \psi_j) = \frac{N\pi}{T}\frac{g_0^2}{\omega_{\mathrm{m}}^2}\left(\left(\frac{\eta_{\boldsymbol{\psi}}^2}{3\omega_{\mathrm{m}}^2}a^2 + \mathrm{h.c.}\right) - 2n_{\mathrm{c}}^2 - \frac{4\eta_0^2}{3\omega_{\mathrm{m}}^2}n_{\mathrm{c}}\right) , \tag{3.7}$$

where

$$\eta_{\boldsymbol{\psi}}^2 = \frac{1}{N}\sum_{j=1}^{N} E_j^2 e^{-2i\psi_j} \text{ , and } \eta_0^2 = \frac{1}{N}\sum_{j=1}^{N} E_j^2 \text{ .} \tag{3.8}$$

The presented effective Hamiltonian offers a promising framework for generating nonclassical states, overcoming the limitations imposed by linear optics through the incorporation of Kerr-like nonlinearity, namely the term n_{c}^2. Yet, in practice, it is desirable to have a nonlinearity n_{c}^2 that is strong compared to the linear term n_c in order to obtain a spectrum of the diagonal part of H_{f} in Eq. (3.7) with strongly

uneven spacing between neighbouring energy levels as discussed in Sec. 2.3.2. In particular, it is noteworthy that the linear term $\propto n_c$ in the effective Hamiltonian becomes increasingly significant with increasing driving strength, unlike the nonlinear term $\propto n_{\mathrm{c}}^2$ which remains constant. To achieve the desirable energy level spectrum, it is thus essential to establish a mechanism that effectively mitigates the amplification of the linear term while preserving the strength of the nonlinear term.

The central idea that allows the suppression of the linear term to be achieved is to note that rotating the driving field in the phase space relative to the system frame is equivalent to phase rotation of the system while keeping the driving field static [112]. Consequently, a phase shift represented by the change in the parameter ψ_j has an approximately same effect as the free evolution induced by the photon number operator n_{c}.

To formalize this notion, it is helpful to note that the interaction Hamiltonian in Eq. (3.5), denoted as $H_{\mathrm{I}}(\psi)$ with explicit phase dependence, satisfies the following relation

$$\begin{aligned} H_{\mathrm{I}}(\psi) =& R(\psi) H_{\mathrm{I}}(0) R^{\dagger}(\psi) \ , \ \text{with} \\ R(\psi) =& e^{i\psi n_{\mathrm{c}}} \ , \end{aligned} \tag{3.9}$$

and thus the effective Hamiltonians H_{e} and H_{f} in Eq. (3.6) and Eq. (3.7) also obey this relation. As a result, the propagator induced by the effective Hamiltonian $H_{\mathrm{e}}(\psi)$ can be expressed as:

$$e^{-iH_{\mathrm{e}}(\psi)t} = R(\varphi) e^{-iH_{\mathrm{e}}(\psi-\varphi)t} R^{\dagger}(\varphi) \ , \tag{3.10}$$

with a phase φ that can be chosen at will.

Utilizing the identity $R^{\dagger}(\varphi_{j+1}) R(\varphi_j) = R^{\dagger}(\phi_j)$, where $\phi_j = \varphi_{j+1} - \varphi_j$, the product of two propagators corresponding to consecutive periods simplifies to:

$$U^{(j+1)} U^{(j)} = R(\varphi_{j+1}) e^{-iH_{\mathrm{e}}(\psi_{j+1}-\varphi_{j+1})T} R^{\dagger}(\phi_j) e^{-iH_{\mathrm{e}}(\psi_j-\varphi_j)T} R^{\dagger}(\varphi_j) \ . \tag{3.11}$$

Consequently, the complete propagator over N periods can be expressed as:

$$U = R(\varphi_{N+1}) \prod_{j=1}^{N} R^{\dagger}(\phi_j) e^{-iH_{\mathrm{e}}(\psi_j - \varphi_j)T} , \tag{3.12}$$

in which the initial and final relations $R^{\dagger}(0) = \mathbb{1}$ and $R(\varphi_N) = R(\varphi_{N+1}) R^{\dagger}(\phi_N)$ have been applied.

The first factor $R(\varphi_{N+1})$ in Eq. (3.12) represents an effective free phase evolution occurring after all the time intervals of driven dynamics. Since this factor represents a rotation in phase space, it does not affect the nonclassical nature of the final states.

Each factor $R^{\dagger}(\phi_j) e^{-iH_{\mathrm{e}}(\psi_j - \varphi_j)T}$ in Eq. (3.12) consists of a term $e^{-iH_{\mathrm{e}}(\psi_j - \varphi_j)T}$ induced by the effective Hamiltonian and a term of free phase evolution induced by n_{c}. As the term linear in n_{c} in the effective Hamiltonian H_{e} is accompanied by a small coefficient on the order of $g_0^2/\omega_{\mathrm{m}}^2$, this is equivalent to an evolution induced by an effective Hamiltonian with a modified term n_{c}. Specifically, the approximation

$$R^{\dagger}(\phi_j) e^{-iH_{\mathrm{e}}(\psi_j - \varphi_j)T} \simeq e^{-i(H_{\mathrm{e}}(\psi_j - \varphi_j)T) + i\phi_j n_c} \tag{3.13}$$

is sufficiently good for the purpose of state preparation given that the condition $\phi_j g_0^2/\omega_{\mathrm{m}}^2 \ll 1$ is satisfied.

Now the effective Hamiltonian for each period contains an extra term $\propto n_c$ in addition to H_{e}, and the freedom to choose values for the phase angles ψ_j and ϕ_j can be used to ensure that undesired terms cancel. For any choice of the driving parameters E_j and ψ_j satisfying

$$\sum_{j=1}^{N} E_j e^{-i(\psi_j - \varphi_j)} = 0 , \text{ and } \sum_{j=1}^{N} E_j^2 e^{-2i(\psi_j - \varphi_j)} \neq 0 , \tag{3.14}$$

the effective Hamiltonian after N periods reduces to

$$N H_{\mathrm{f}} = \frac{N\pi}{T} \frac{g_0^2}{\omega_{\mathrm{m}}^2} \left(\left(\frac{\eta_{\boldsymbol{\psi}-\boldsymbol{\varphi}}^2}{3} a^2 + \mathrm{h.c.} \right) - 2n_{\mathrm{c}}^2 \right) - \frac{1}{T} \sum_{j=1}^{N} \left(\frac{4\pi E_j^2 g_0^2}{3\omega_{\mathrm{m}}^4} - \phi_j \right) n_c + O\left(\sum_{j=1}^{N} \frac{g_0^2 \phi_j}{\omega_{\mathrm{m}}^2} \right) , \tag{3.15}$$

with

$$\eta^2_{\boldsymbol{\psi}-\boldsymbol{\varphi}} = \frac{1}{N}\sum_{j=1}^{N} E_j^2 e^{-2i(\psi_j-\varphi_j)} \,. \tag{3.16}$$

With the specific choice of $\phi_j = 4\pi E_j^2 g_0^2/(3\omega_{\mathrm{m}}^4)$, the terms linear in n_c vanish to leading order during each period, and the higher-order contributions $\sim O(g_0^2\phi_j/\omega_{\mathrm{m}}^2)$ become negligible compared to the leading-order term. Since ϕ_j is the accumulated phase shift of the driving pattern, this amounts to the individual phases

$$\varphi_j = \frac{4\pi g_0^2}{3\omega_{\mathrm{m}}^2}\sum_{l=1}^{j-1}\frac{E_l^2}{\omega_{\mathrm{m}}^2} \tag{3.17}$$

that increase by amounts determined by the driving amplitude E_j.

While it is theoretically sufficient for the effective Hamiltonian to match the desired Hamiltonian at the end of the interval of interest, it is preferable to achieve this match at intermediate time points as well. Therefore, I consider a driving protocol in which the total time window of duration NT is divided into $N/2$ blocks, each with a duration of $2T$. The dynamics within each block are induced by the desired effective Hamiltonian within the perturbative approximation.

Within each block, a constant driving amplitude is considered (i.e. $E_{2j-1} = E_{2j}$ for each j). Consequently, one optimal choice of the phases can be identified as follows

$$\begin{aligned}
\psi_{2j-1} = \varphi_{2j-1} &= \frac{4\pi g_0^2}{3\omega_{\mathrm{m}}^2}\sum_{l=1}^{j-1}\frac{2E_{2l}^2}{\omega_{\mathrm{m}}^2} \,, \\
\psi_{2j} = \pi + \varphi_{2j} &= \pi + \frac{4\pi g_0^2}{3\omega_{\mathrm{m}}^2}\left(\frac{E_{2j}^2}{\omega_{\mathrm{m}}^2} + \sum_{l=1}^{j-1}\frac{2E_{2l}^2}{\omega_{\mathrm{m}}^2}\right) \,.
\end{aligned} \tag{3.18}$$

This choice of the driving profiles not only satisfies Eq. (3.14), but also maximizes the coefficient before the quadratic terms a^2 and $(a^\dagger)^2$ by ensuring $\eta^2_{\boldsymbol{\psi}-\boldsymbol{\varphi}} = \eta_0^2$ where $\eta_{\boldsymbol{\psi}-\boldsymbol{\varphi}}$ and η_0 are defined in Eq. (3.16) and Eq. (3.8), respectively. By employing this choice, the resulting effective Hamiltonian over N periods of driven dynamics can be expressed as

$$NH_{\mathrm{g}} = \frac{\pi}{T}\frac{g_0^2}{\omega_{\mathrm{m}}^2}\sum_{j=1}^{\frac{N}{2}}\left(\frac{2E_{2j}^2}{3\omega_{\mathrm{m}}^2}\left(a^2+(a^\dagger)^2\right) - 4n_{\mathrm{c}}^2\right) \,. \tag{3.19}$$

This can serve as a starting point for state preparation, but it is worthwhile to explore higher-order per-

turbative corrections. Such an investigation would significantly enhance the accuracy of state preparation with only slightly more complex driving patterns.

3.2.3 Third-order corrections

Although the model considered in Sec. 3.2 does not explicitly impose a constraint on the maximum evolution time, in practice, the robustness of the state-preparation protocol diminishes as the evolution time increases, owing to the presence of system dissipation. Consequently, it is preferable to minimize the overall evolution time. Because the rate of pumping photons into the optomechanical cavity is primarily limited by the driving strength, shorter evolution time can be achieved by employing a driving strength as strong as possible. However, it is also essential to note that stronger driving also amplifies errors in the truncated Magnus series, thus compromising the performance of the designed driving scheme. Hence, it is necessary to take into account higher-order effects. The central objective of this section is to refine the driving pattern to effectively accommodate the inclusion of the third-order Magnus terms $\mathcal{M}_3$ as defined in Eq. (2.25).

To aid readers' comprehension, I provide a summary of the third-order Magnus term $\mathcal{M}_3$, which comprises a mechanical term denoted as $\mathcal{M}_3^{\mathrm{M}}$ and an interaction term denoted as $\mathcal{M}_3^{\mathrm{I}}$. Specifically, the interaction term $\mathcal{M}_3^{\mathrm{I}}$ can be expressed as the sum $\mathcal{M}_{3,1}^{\mathrm{I}}+\mathcal{M}_{3,2}^{\mathrm{I}}+\mathcal{M}_{3,3}^{\mathrm{I}}$, with the three components defined in Eq. (2.26).

With the driving pattern derived above in Sec. 3.2.2, the effective Hamiltonian, for the dynamics over two periods of driving with constant driving amplitude, is given by

$$2H_{\mathrm{p}} = 2H_{\mathrm{g}} + \frac{2}{T}\frac{g_0^3}{\omega_{\mathrm{m}}^3}\left(\mathcal{M}_3^{\mathrm{M}} + \mathcal{M}_{3,3}^{\mathrm{I}}(\psi=0)\right) , \tag{3.20}$$

in which H_{g} corresponds to the second-order effective Hamiltonian defined in Eq. (3.19). In this context, the term $\mathcal{M}_{3,3}^{\mathrm{I}}(\psi=0)$ denotes the operator $\mathcal{M}_{3,3}^{\mathrm{I}}$ evaluated at $\psi=0$, which is also equal to its evaluation at $\psi=\pi$. The contributions from $\mathcal{M}_{3,1}^{\mathrm{I}}$ and $\mathcal{M}_{3,2}^{\mathrm{I}}$ in $\mathcal{M}_3^{\mathrm{I}}$ average out within the effective Hamiltonian H_{p}. However, there remains a finite correction originating from the term $\mathcal{M}_{3,3}^{\mathrm{I}}$ within the interaction term $\mathcal{M}_3^{\mathrm{I}}$, along with a contribution by the term $\mathcal{M}_3^{\mathrm{M}}$ to the effective Hamiltonian arising

from the mechanical oscillator.

In order to minimize undesired effects, it is important to eliminate not only the interaction term $\mathcal{M}^{\mathrm{I}}_{3,3}$ but also the mechanical term $\mathcal{M}^{\mathrm{M}}_{3}$ from the full effective Hamiltonian. This is because the presence of the term $\mathcal{M}^{\mathrm{M}}_{3}$ induces excitations in the mechanical oscillator, and as the excitations of the mechanical oscillator increase, the impact of interactions on the optical field in higher-order corrections becomes more prominent. Hence, the primary focus in the subsequent paragraphs is on modifying the driving pattern to minimize these terms as much as possible.

One feasible approach is by observing that a half-period of free evolution for the mechanical oscillator corresponds to a phase shift of π in the mechanical creation and annihilation operators, $b^\dagger$ and b. Both $\mathcal{M}^{\mathrm{M}}_{3}$ and $\mathcal{M}^{\mathrm{I}}_{3,3}(\psi = 0)$ are odd functions in b and $b^\dagger$. Therefore, by employing a sequence consisting of two periods of dynamics induced by $\mathcal{M}^{\mathrm{M}}_{3} + \mathcal{M}^{\mathrm{I}}_{3,3}(\psi = 0)$, with a half-period of free evolution in between, an effective cancellation is achieved. Equivalently, any driving protocol that alternates between driven dynamics and intervals of free evolution, while satisfying the phase requirements defined in Eq. (3.18), and where the duration of free evolution is precisely half a period of free evolution, guarantees the cancellation of third-order terms deviating from the desired effective Hamiltonian H_{g}.

In practice, however, achieving an exact free evolution of the mechanical oscillator is not feasible due to the inherent interaction between the mechanical oscillator and the light field. The following paragraphs thus serve to show that an interval of undriven dynamics can be used to achieve a similar effect.

Following the solution to the evolution of undriven optomechanical systems in Eq. (2.15), the propagator for the undriven dynamics over half a mechanical period reads

$$U_{\mathrm{OM}}\left(\frac{T}{2}\right) = \exp\left(\pi i \frac{g_0^2}{\omega_{\mathrm{m}}^2} n_{\mathrm{c}}^2\right) e^{-2\frac{g_0}{\omega_{\mathrm{m}}} n_c (b - b^\dagger)} e^{-\pi i n_m} \,, \tag{3.21}$$

given that the optical resonance frequency is an even multiple of the mechanical resonance frequency. The adjoint of this propagator satisfies the relation

$$U^\dagger_{\mathrm{OM}}\left(\frac{T}{2}\right) = U_{\mathrm{OM}} \exp\left(-2\pi i \frac{g_0^2}{\omega_{\mathrm{m}}^2} n_{\mathrm{c}}^2\right) \,. \tag{3.22}$$

A sequence with two driven dynamics intervals, and a preceding undriven interval before each driven period, leads to the propagator

$$\begin{aligned}
&\exp\left(-2iH_{\mathrm{p}}T\right)U_{\mathrm{OM}}^{\dagger}\left(\frac{T}{2}\right)\exp\left(-2iH_{\mathrm{p}}T\right)U_{\mathrm{OM}}\left(\frac{T}{2}\right)\\
=&\exp\left(-2iH_{\mathrm{p}}T\right)U_{\mathrm{OM}}^{\dagger}\left(\frac{T}{2}\right)\exp\left(2\pi i\frac{g_0^2}{\omega_{\mathrm{m}}^2}n_{\mathrm{c}}^2\right)\exp\left(-2iH_{\mathrm{p}}T\right)U_{\mathrm{OM}}\left(\frac{T}{2}\right)\\
\approx&\exp\left(-2iH_{\mathrm{p}}T\right)U_{\mathrm{OM}}^{\dagger}\left(\frac{T}{2}\right)\exp\left(-2iH_{\mathrm{p}}T+2\pi i\frac{g_0^2}{\omega_{\mathrm{m}}^2}n_{\mathrm{c}}^2\right)U_{\mathrm{OM}}\left(\frac{T}{2}\right)\ ,
\end{aligned}\tag{3.23}$$

where terms of order g_0^4 in the Baker-Campbell-Hausdorff relation are neglected. Within the same approximation, the effective Hamiltonian over the four intervals (i.e. five mechanical periods) is defined by

$$5TH_{\mathrm{q}}=2T\left(H_{\mathrm{p}}+U_{\mathrm{OM}}^{\dagger}\left(\frac{T}{2}\right)H_{\mathrm{p}}U_{\mathrm{OM}}\left(\frac{T}{2}\right)-\frac{\pi}{T}\frac{g_0^2}{\omega_{\mathrm{m}}^2}n_{\mathrm{c}}^2\right)\tag{3.24}$$

where the equality $[U_{\mathrm{OM}}(T/2),n_{\mathrm{c}}^2]=0$ has been implicitly applied. Hence, the introduction of half intervals of free evolution serves as an effective unitary transformation on the effective Hamiltonian H_{p}, accompanied an additional term representing the optical Kerr-like nonlinearity. To leading orders (i.e. g_0^3), this unitary transformation of the effective Hamiltonian can be written as

$$\begin{aligned}
&U_{\mathrm{OM}}^{\dagger}\left(\frac{T}{2}\right)\left(H_{\mathrm{g}}+\frac{1}{T}\frac{g_0^3}{\omega_{\mathrm{m}}^3}\left(\mathcal{M}_3^{\mathrm{M}}+\mathcal{M}_{3,3}^{\mathrm{I}}(\psi=0)\right)\right)U_{\mathrm{OM}}\left(\frac{T}{2}\right)\\
\approx&U_{\mathrm{OM}}^{\dagger}\left(\frac{T}{2}\right)H_{\mathrm{g}}U_{\mathrm{OM}}\left(\frac{T}{2}\right)-\frac{1}{T}\frac{g_0^3}{\omega_{\mathrm{m}}^3}\left(\mathcal{M}_3^{\mathrm{M}}+\mathcal{M}_{3,3}^{\mathrm{I}}(\psi=0)\right)\\
\approx&\left(H_{\mathrm{g}}+\frac{2}{3T}\frac{g_0^3}{\omega_{\mathrm{m}}^3}\mathcal{M}_{3,3}^{\mathrm{I}}(\psi=0)\right)-\frac{1}{T}\frac{g_0^3}{\omega_{\mathrm{m}}^3}\left(\mathcal{M}_3^{\mathrm{M}}+\mathcal{M}_{3,3}^{\mathrm{I}}(\psi=0)\right)\ ,
\end{aligned}\tag{3.25}$$

in which the terms $\mathcal{M}_3^{\mathrm{M}}$ and $\mathcal{M}_{3,3}^{\mathrm{I}}$ acquire negative signs under the unitary transformation defined by the propagator $U_{\mathrm{OM}}(T/2)$. Consequently, these negative terms cancel out the corresponding positive terms in the first term (i.e. H_{p}) of Eq. (3.24), resulting in the elimination of undesired processes in the mechanical degree of freedom in leading orders. However, for the interaction terms, this cancellation is not perfect due to the additional correction term generated by the transformation of the second-order effective Hamiltonian H_{g}. This residual interaction in the effective Hamiltonian is also proportional to the interaction term $\mathcal{M}_{3,3}^{\mathrm{I}}(\psi=0)$ but is reduced by a factor of three compared to what could be

achieved without intervals of free evolution.

The incorporation of half-periods of undriven dynamics offers a significant enhancement in the accuracy of the desired effective Hamiltonians. However, a careful reassessment of the decomposition of the full evolution operator into multiple evolution operators over shorter periods (for example, see Eq. (2.20)) is required. When half-periods of evolution are inserted in between driven periods, the evolution operator over time $\mathcal{T}$ takes the form

$$\begin{aligned} U_{\mathrm{I}}\Big(0,\mathcal{T}\Big) =& U_{\mathrm{I}}\Big(0,T\Big)U_{\mathrm{I}}\Big(T,2T\Big)U_{\mathrm{I}}\Big(2T,\frac{5}{2}T\Big)U_{\mathrm{I}}\Big(\frac{5}{2}T,\frac{7}{2}T\Big)U_{\mathrm{I}}\Big(\frac{7}{2}T,\frac{9}{2}T\Big)U_{\mathrm{I}}\Big(\frac{9}{2}T,5T\Big)\,, \\ =& U_{\mathrm{I},1}\Big(0,T\Big)U_{\mathrm{I},2}\Big(0,T\Big)U_{\mathrm{I},0}\Big(0,\frac{1}{2}T\Big)U_{\mathrm{I},3}\Big(\frac{1}{2}T,\frac{3}{2}T\Big)U_{\mathrm{I},4}\Big(\frac{1}{2}T,\frac{3}{2}T\Big)U_{\mathrm{I},0}\Big(\frac{1}{2}T,T\Big)\,, \end{aligned} \tag{3.26}$$

where the subscript j in $U_{\mathrm{I},j}$ indicates the potentially different driving parameters adopted for each driven period. In the most general case, the equality

$$U_{\mathrm{I},3}\Big(\frac{1}{2}T,\frac{3}{2}T\Big)U_{\mathrm{I},4}\Big(\frac{1}{2}T,\frac{3}{2}T\Big)U_{\mathrm{I},0}\Big(\frac{1}{2}T,T\Big) = U_{\mathrm{I},3}\Big(0,T\Big)U_{\mathrm{I},4}\Big(T,2T\Big)U_{\mathrm{I},0}\Big(0,\frac{1}{2}T\Big) \tag{3.27}$$

is not guaranteed. However, with the specific driving function discussed in this section, the evolution operators on the two sides of the equation coincide, and the rationale for this is elucidated below. Noticing that because the driving function has a period $T/2$ while the interaction Hamiltonian H_{I} in Eq. (3.5) has a period T, half-periods of undriven dynamics effectively introduce a phase of π between the driving field and the optomechanical system. In this picture, while all other parameters are kept constant, the evolution $U_{\mathrm{I}}(\frac{1}{2}T,\frac{3}{2}T)$ given the driving function $\xi(t)$ is equivalent to an evolution $\tilde{U}_{\mathrm{I}}(0,T)$ given the driving function $\xi(t-(T/2))$, and similarly, $U_{\mathrm{I}}(T/2,T)$ is equivalent to $\tilde{U}_{\mathrm{I}}(0,T/2) = U_{\mathrm{I}}(0,T/2)$. Because the driving function $\xi(t-(T/2))$ reduces to $-\xi(t)$ given the driving function in Eq. (3.3), the optical mode gains a phase of π (i.e. $a \to -a$). Therefore, the cancellation of terms $\propto e^{\pm i\psi}$ in Eq. (3.7) (with $N = 2$) is not affected as it only depends on the relative phase between each pair of consecutive driven periods. Additionally, because the effective Hamiltonian H_{p} (refer to Eq. (3.20)) for the evolution operator $\tilde{U}_{\mathrm{I}}(0,2T)$ is an even function of the optical mode operators (a and $a^{\dagger}$), it is also the effective Hamiltonian inducing the evolution operator $\tilde{U}_{\mathrm{I}}(0,2T)$, and thus the evolution operator $U_{\mathrm{I}}(T/2,5T/2)$.

In addition to the decomposition of the evolution operator,a careful reassessment of the discussion presented in Sec. 3.2.2 is also necessary. In particular, in the discussion of Eq. (3.12), the effective optical phase rotation arises from the change in driving amplitude during the subsequent driven period. However, due to the inclusion of half-periods of undriven dynamics, this change of driving amplitude may now occur after a half-period of undriven dynamics, rather than immediately following the previous driven period. Fortunately, because the propagator $U_{\mathrm{OM}}(T/2)$ commutes with the operator $R(\phi_j)$ in Eq. (3.9), the dynamics within any time window of two periods of driven dynamics can still be described by the propagator $\exp\left(-iH_{\mathrm{g}}T\right)$ with H_{g} defined in Eq. (3.19). Therefore, the discussion resulting in Eq. (3.12) naturally includes the case of half-periods of undriven dynamics.

3.2.4 Optimized driving pattern

By implementing a driving protocol consisting of a pair of time windows, each with two periods of driven dynamics followed by half a period of undriven dynamics (as sketched in Fig. 3.2), the effective Hamiltonian for the dynamics over $\mathcal{T} = 5T$ is defined by

$$H_{\mathrm{eff}} = \left(\frac{g_0^2}{\omega_{\mathrm{m}}^2} H^{(2)} + \frac{g_0^3}{\omega_{\mathrm{m}}^3} H^{(3)} \right) , \tag{3.28}$$

with

$$\begin{aligned} \mathcal{T} H_{\mathrm{eff}}^{(2)} &= \pi \frac{4E^2}{3\omega_{\mathrm{m}}^2} \left(a^2 + (a^\dagger)^2 \right) - 10\pi n_{\mathrm{c}}^2 , \\ \mathcal{T} H_{\mathrm{eff}}^{(3)} &= \pi \frac{8E^2}{3\omega_{\mathrm{m}}^2} \left((a^\dagger)^2 - a^2 \right) \left(b - b^\dagger \right) . \end{aligned} \tag{3.29}$$

While the effective Hamiltonian presented in Eq. (3.19) could have been taken as the starting point for the subsequent analysis, the enhanced suppression of undesired processes achieved by using a slightly more elaborate driving protocol makes Eq. (3.28) the preferred choice.

The devised driving profiles ensure the significant suppression of undesired processes, allowing the amplitude of the driving field to be selected based on the desired target state. To achieve high-fidelity state preparation, it is beneficial to consider a series of five intervals $\mathcal{T}$ of driven dynamics and optimize the driving amplitudes for each of these intervals.

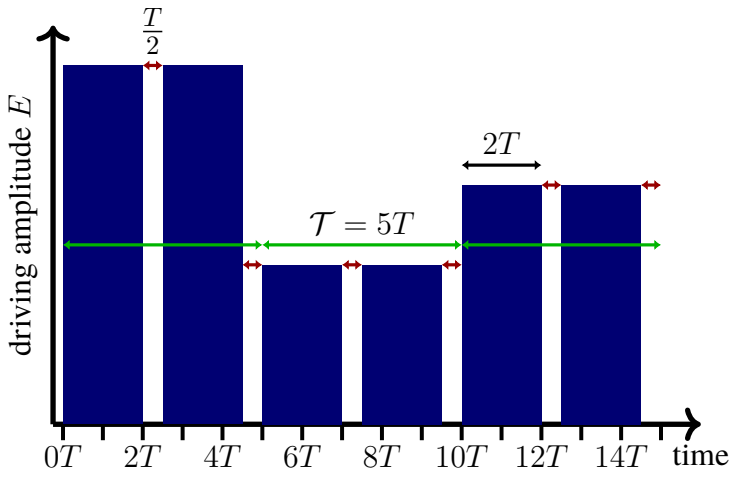


Figure 3.2: Schematic example of a driving pattern of duration $15T = 3\mathcal{T}$. The protocol is comprised of three intervals of length $\mathcal{T} = 5T$ (green, long arrows) characterized by a constant value of the driving amplitude E. Each of these intervals consists of a pair of time-windows of length $2T$ of driven dynamics (black arrow), each of which is followed by half a period of undriven dynamics (red, short arrows). The driving amplitudes shown in the plot serve solely as examples; in actuality, these amplitudes are numerically optimized for each specific target state.

Since such optimizations require the analysis of system dynamics with several different patterns of driving amplitudes, efficiency in the numerical propagation is essential. Therefore, I employ the effective Hamiltonian $H_{\text{eff}}^{(2)}$ in Eq. (3.29). This level of approximation excludes any interaction between the cavity field and the mechanical oscillator, enabling the numerical simulation to focus solely on the dynamics of the cavity field. In the following section, I provide two examples. These examples demonstrate how to prepare a target state using optimized driving patterns.

3.3 Numerical results

The driving scheme presented in Sec. 3.2 provides a mechanism to identify driving patterns that facilitate the desired evolution towards nonclassical pure states of light. This scheme surpasses the constraints imposed by the need to utilize a driving amplitude weaker than the optomechanical anharmonicity ($\propto g_0^2/\omega_{\text{m}}$). In this section, the generation of a two-photon Fock state and its superposition state with the vacuum are demonstrated through optimized driving pattern.

Firstly, numerical optimization is conducted within a truncated Hilbert space for the cavity field, constrained to the lowest 30 Fock states. To maintain the negligible significance of higher-order terms

omitted in Sec. 3.2, limitations on the maximum permissible driving amplitude E are imposed (see Sec. 3.4 for more discussion). Following this, numerical simulations are performed to validate the accuracy of the optimized driving patterns. These simulations include both the cavity and mechanical field within a truncated Hilbert space, comprising the lowest 60 optical Fock states and 30 mechanical Fock states, respectively. All simulation results are computed via the Python toolbox QuTiP [148,149], and the parameters adopted for each simulation are presented in Appendix B.1.

The accuracy of the state preparation is examined through the fidelity, as delineated in [66], and is given below as[4]

$$F(|\psi_{\text{fin}}\rangle, |\psi_{\text{tar}}\rangle) = \left|\langle\psi_{\text{fin}}|\psi_{\text{tar}}\rangle\right| . \tag{3.30}$$

This metric specifies the degree of similarity between the final state $|\psi_{\text{fin}}\rangle$ and the target state $|\psi_{\text{tar}}\rangle$.

3.3.1 Fock state preparation

Given the aptitude of the existing control scheme in producing photon pairs, the creation of the photonic Fock state $|2\rangle$ from an optical ground state $|0\rangle$ emerges as a fitting task. To minimize any undesirable interaction between the mechanical and the optical degrees of freedom, the oscillator is also assumed to be initially at its ground state.

Fig. 3.3 depicts the dynamics of the cavity field under optimised driving, spanning an evolution time of $16\mathcal{T}$, with a maximum admissible driving strength $E_{\text{max}} = 4\omega_{\text{m}}$ and a coupling strength $g_0 = \omega_{\text{m}}/26$. Subplots (a) and (b) present the occupation of the lowest six Fock states as functions of time. Due to the suppression of the creation of single photons, as elaborated in Sec. 3.2, the populations of odd Fock states are markedly smaller by orders of magnitude compared to those of even Fock states. Throughout the dynamics, significant populations of the states $|4\rangle$ and $|6\rangle$ are observed, indicating that despite the suppression of excitations to higher-lying states, occupancy in these states does occur. The undesired occupation suggests that the chosen driving amplitude is large compared to the unequal spacing

[4] Another prevalent definition of fidelity, as showcased in [150]. This alternate definition is essentially the square of the fidelity (i.e. F^2) adopted in this thesis and in the reference [66]. Although the former version may be perceived as more intuitive, given its linkage to transition probabilities [151], this chapter adheres to the definition provided in [66] to maintain consistency with the conventions of QuTiP, the computational toolbox employed for this study.

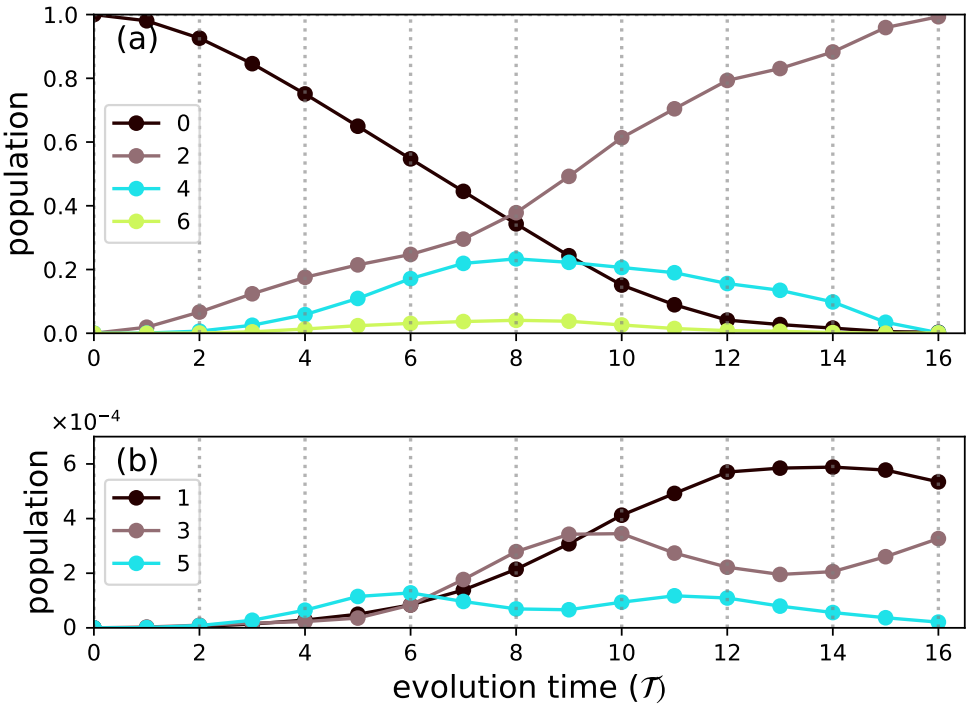


Figure 3.3: Plots of populations of Fock states in the cavity. Subplot (a) plots populations of even Fock states and subplot (b) plots populations of odd Fock states. The coupling strength is $g_0 = \omega_{\mathrm{m}}/26$, the driving strengths E are optimized with a maximally admissible value $E_{\mathrm{max}} = 4\omega_{\mathrm{m}}$, and the length of evolution is $t_f = 16\mathcal{T}$. A data point is plotted after each five mechanical periods $\mathcal{T}$. The final state is almost a Fock state $|2\rangle$.

in the system energy spectrum. Nonetheless, the application of a numerically optimized driving pattern yields dynamics wherein these non-desirable states remain unoccupied in the final state, thereby attaining a high final fidelity $F = 0.997$.

In an idealized scenario characterized by lossless dynamics, optimal results are anticipated in the limit of long evolution times and weak optomechanical interaction (i.e. $t \to \infty$ while $g_0 \to 0$), as this limit signifies the regime where the underlying perturbative treatment becomes exact. However, practical implementation necessitates confining the dynamics within a limited time frame to mitigate the influence of dissipative effects on state preparation. Shorter evolution times typically mandate stronger interaction, which can potentially conflict with the perturbative approximation, necessitating a balanced approach.

For any given evolution time, one would thus expect to find an optimal value of the interaction constant g_0. Figure 3.4 illustrates the fidelity F (solid) obtained with optimized driving and the correspond-

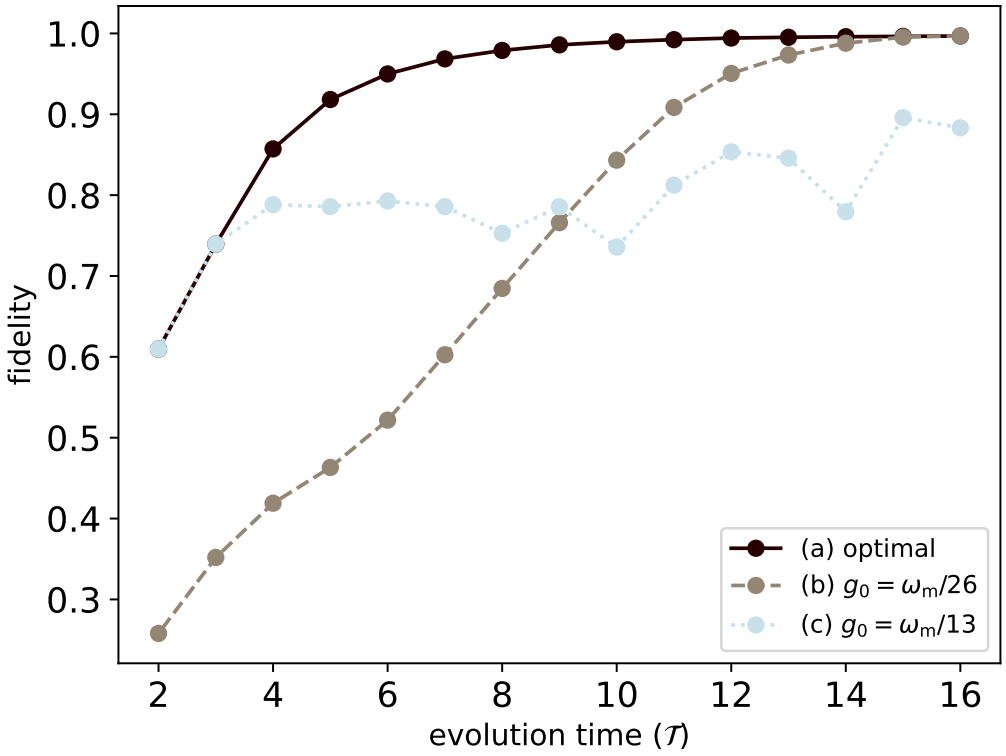


Figure 3.4: Plot of the fidelity F_n against the evolution time t_f in $\mathcal{T}$ when $E_{max} = 4\omega_m$. (a) For each time point, the coupling strength g_0 is optimized to achieve the highest possible fidelity. (b) The coupling strength is fixed to be $g_0 = \omega_m/26$. (c) The coupling strength is fixed to be $g_0 = \omega_m/13$. The combination of interaction strength and evolution time has a great impact on the final fidelity F.

ing interaction strength deemed optimal for each given evolution time t_f, ranging from $2\mathcal{T}$ to $16\mathcal{T}$. Additionally, the fidelity F obtained with optimized driving profiles at fixed interaction strengths of $g_0 = \omega_m/13$ (dotted) and $g_0 = \omega_m/26$ (dashed) are juxtaposed for comparison[5]. Comparison of the three curves highlights the considerable enhancement in fidelity of state preparation through the selection of a suitable combination of interaction strength and evolution time. Notably, the curve representing optimal combinations of coupling strengths and evolution times aligns with the (dashed) curve for a constant coupling strength $g_0 = \omega_m/26$ at prolonged evolution times (i.e. $t_f \sim 16\mathcal{T}$). On the other hand, the highest fidelity achievable at the fixed coupling strength $g_0 = \omega_m/26$ registers at $F = 0.843$ for the evolution time $t_f = 10\mathcal{T}$, whereas, with an optimal coupling strength $g_0 \approx 0.048\omega_m$, fidelity remains near unity at $F = 0.990$.

As depicted in Fig. 3.4, the stronger optomechanical interaction $g_0 = \omega_m/13$ proves beneficial over

[5]The two boundary values are chosen such that the fidelity is close to its maximum at corresponding evolution time ($T = 2\mathcal{T}, 16\mathcal{T}$) in the plot. In particular, $T = 2\mathcal{T}$ is the shortest evolution time that can be improved through optimization, and $T = 16\mathcal{T}$ is the shortest evolution time that permits the final fidelity to reach 0.99.

the weaker interaction $g_0 = \omega_{\mathrm{m}}/26$ when the evolution time is short (i.e. $t_{\mathrm{f}} \leq 8\mathcal{T}$). However, the maximum achievable fidelity is ultimately limited due to diminished accuracy of the perturbative method. This impact becomes particularly evident when coupling strength is $g_0 = \omega_{\mathrm{m}}/13$, where the data points (connected by dotted lines) do not follow a monotonic curve as the evolution time increases. When the perturbative approximation fails, numerical optimization based on the theoretical evolution operator falls into local minima. This results in high theoretical values but causes the simulated state fidelity values to decrease. The collapse of the perturbative model has another implication. It suggests that the numerical results in Fig. 3.4 may not showcase the highest possible values among all similar theoretical minima. Consequently, the insights provided by the state fidelities given strong optomechanical couplings are better interpreted as offering a qualitative perspective rather than exact quantitative conclusions. For a comprehensive analysis of the range where the perturbative assumptions remain valid, readers are directed to Sec. 3.4.

3.3.2 Superposition preparation

Analogous to the creation of Fock states, the current framework can be adapted to identify driving patterns for generating coherent superpositions of Fock states. This is illustrated by the target state:

$$|\Psi_\vartheta\rangle = \frac{1}{\sqrt{2}}\left(|0\rangle + e^{i\vartheta}|2\rangle\right) . \tag{3.31}$$

In addition to optimizing the driving profile, the subsequent optimization also takes into account the relative phase ϑ, presenting two viable approaches. The first strategy involves identifying the target state best aligned with all balanced superpositions of the Fock states $|0\rangle$ and $|2\rangle$, followed by propelling the final state to the desired state through classical means. However, implementing such an operation within an optomechanical cavity may pose experimental challenges. Apart from classical approaches, an undriven period of dynamics can also lead to an evolution operator $U_{\mathrm{OM}}(T) = \exp\left(2\pi i g_0^2/\omega_{\mathrm{m}}^2 (a^\dagger a)^2\right)$ (refer to Eq. (2.15)) and produce a comparable effect. However, this method necessitates up to $(\omega_{\mathrm{m}}/g_0)^2/8$ mechanical periods to achieve a phase rotation of $\vartheta = \pi$. This duration may prove impractical in the presence of any system dissipation, especially when the coupling strength g_0 is small. Given these considerations, a second strategy which optimizes the driving parameters in

relation to a predetermined phase ϑ emerges as a valuable alternative. Both strategies are explored and detailed further in the subsequent sections.

Firstly, a driving profile that yields a state $|\Psi_\vartheta\rangle$ in the minimal achievable time is searched for, where the relative phase ϑ is not predetermined. Analogous to the Fock states scenario, the driving strengths are optimized for a maximum permissible driving strength $E_{\text{max}} = 4$ and a coupling strength $g_0 = \omega_{\text{m}}/26$. Given that the average number of photons involved in generating an equal superposition state $|\Psi_\vartheta\rangle$ is generally fewer than that required for a Fock state $|2\rangle$, the evolution time can be shortened while maintaining high fidelity between the generated and target states. Numerical optimization indicates that a minimum time of $t_{\text{f}} = 10\mathcal{T}$ is required to secure a fidelity exceeding 0.99 with an equal superposition state. The relative phase corresponding to the highest fidelity is identified as $\vartheta = -1.86$, and the system state dynamics in this context are illustrated in Fig. 3.5. Similar to the observations in Fig. 3.3, the populations of odd Fock states remain orders of magnitude smaller than those of even Fock states. Nevertheless, a notable reduction is observed in the maximum population of each Fock state (excluding the vacuum state) throughout the evolution compared to the instances in Fig. 3.3. This observation substantiates the assertion that fewer photons are engaged during the evolution.

When compared to generating a superposition state with an optimized phase ϑ, the preparation of a superposition state $|\Psi_\vartheta\rangle$ with a predetermined ϑ introduces an additional constraint on the driving profile. Consequently, it is anticipated that the latter would typically necessitate a longer evolution time to attain comparable fidelity values. To substantiate this assertion, one can optimize the driving parameters for the shortest evolution time needed to achieve a fidelity $F(R(\varphi_{N+1})\,|\psi_{\text{fin}}\rangle\,, |\Psi_0\rangle) > 0.99$. Here, $|\psi_{\text{fin}}\rangle$ represents the final state computed from the second-order effective Hamiltonian $H_{\text{eff}}^{(2)}$ in Eq. (3.29), and the driving-dependent rotation operator $R(\varphi_{N+1})$ is defined in Eq. (3.12). For instance, the optimization results reveal that a superposition state $|\Psi_0\rangle$ demands a time of $t_{\text{f}} = 14\mathcal{T}$ to reach a fidelity of $F = 0.998$, namely, requiring an additional time of $4\mathcal{T}$ compared to the scenario depicted in Fig. 3.5.

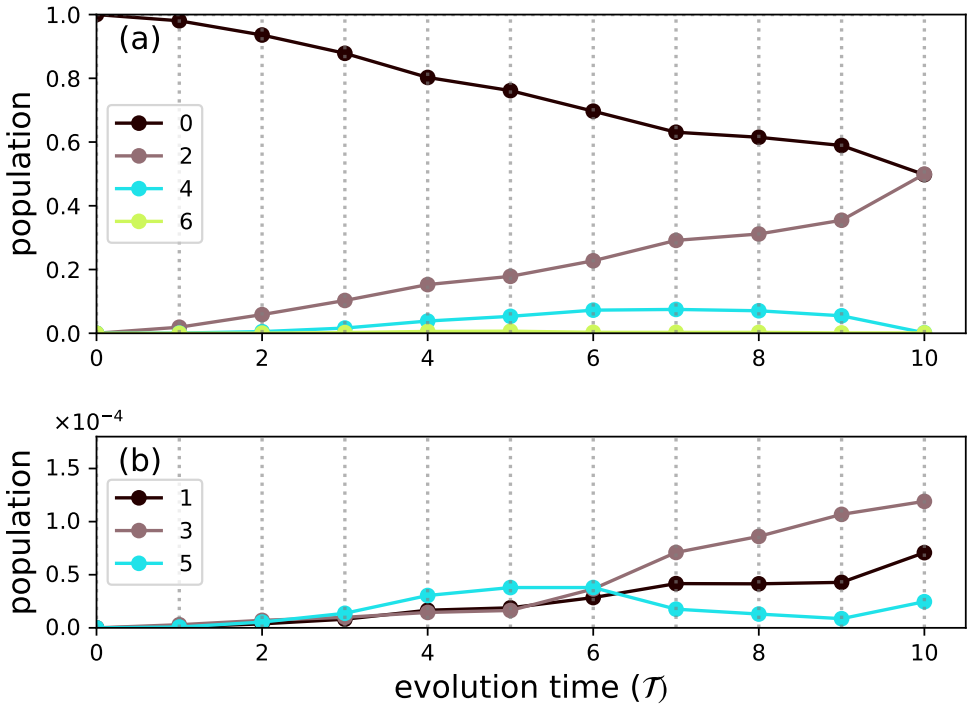


Figure 3.5: Plots of populations of Fock states in the cavity. Subplot (a) plots populations of even Fock states and subplot (b) plots populations of odd Fock states. The relative coupling strength $g_0 = \omega_{\mathrm{m}}/26$, the relative driving strengths η are optimized with a maximally admissible value $E_{\mathrm{max}} = 4$, and the length of evolution is $t_f = 10\mathcal{T}$. A data point is plotted after each five mechanical periods $\mathcal{T}$. The final state is almost an equal superposition state $1/\sqrt{2}\left(|0\rangle + e^{-1.86i}\,|2\rangle\right)$.

3.4 Model accuracy

In the preceding section, an assumption was made that a maximum admissible driving strength $E_{\mathrm{max}} = 4\omega_{\mathrm{m}}$ was set for illustrating target state preparation. However, this designated value may not be universally optimal. Particularly, when dealing with large values of the coupling strength g_0, the higher-order terms dependent on the driving strength E can induce noticeable deviations in system dynamics. For instance, the second-order BCH terms (refer to Eq. (2.21)), which originate from the approximation in Eq. (3.13) are approximately of order $E^2 g_0^2/\omega_{\mathrm{m}}^4$ smaller than the second-order effective Hamiltonian $H_{\mathrm{eff}}^{(2)}$ as delineated in Eq. (3.29). Consequently, these terms have a non-trivial contribution when the relative driving strength E/ω_{m} is comparable to the inverse of the relative coupling strength ω_{m}/g_0.

To delve deeper into the accuracy of the theoretical framework under varied driving parameter sets, Fig. 3.6 compares theoretically predicted outcomes with results from full numerical simulations. Each set of parameters is derived by maximizing the fidelity between the final state, invoked by the second-

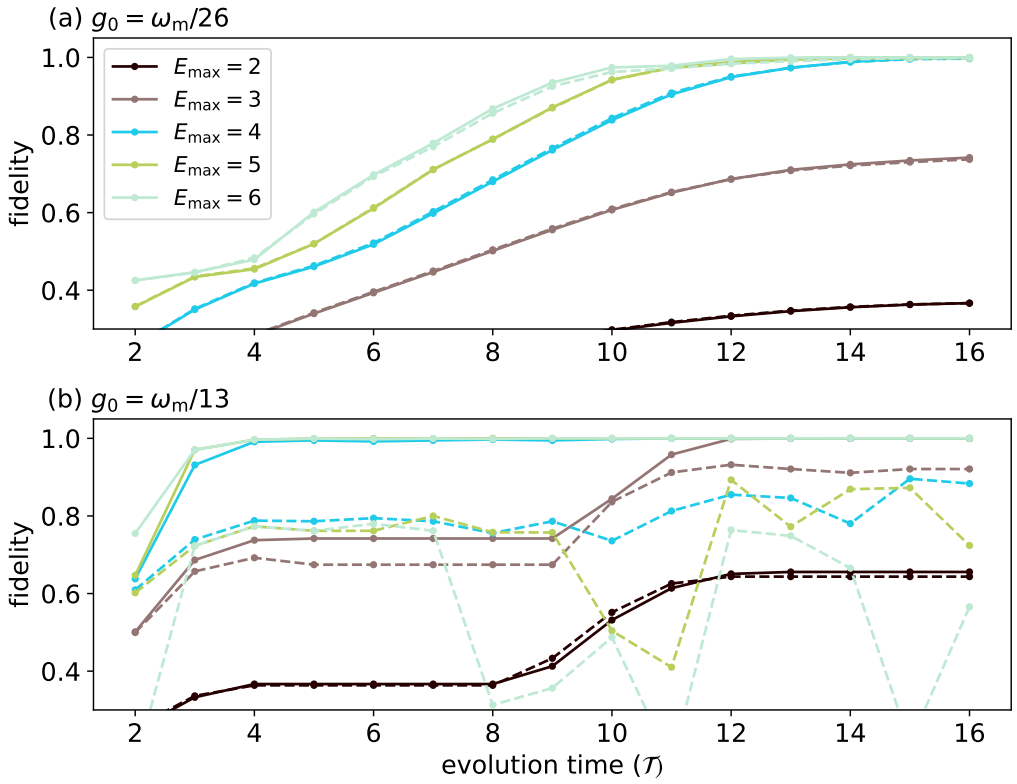


Figure 3.6: Plot of theoretical results (solid lines) and numerical results (dashed lines) of the fidelity between the final state and a two-photon Fock state. Each data point represents the fidelity of the final state when the driving function is optimized for the generation of two-photon Fock state at the given time on x-axis. Subplot(a) and (b) represent cases where $g_0 = \omega_m/26$ and $g_0 = \omega_m/13$ respectively, and the maximum admissible driving strengths are as shown in the plot legend.

order effective Hamiltonian $H_{\text{eff}}^{(2)}$ and a two-photon state $|2\rangle$. The maximized fidelity (solid) is then contrasted with the fidelity (dashed) between the final system state, obtained from full numerical simulation, and the target state $|2\rangle$ for maximum admissible driving strengths $E_{\text{max}} = 2, ..., 6$ and evolution times $t_f = 2\mathcal{T}, ..., 16\mathcal{T}$. Given that the average number of photons in the driving increases from $E_{\text{max}}^2 = 16$ to $E_{\text{max}}^2 = 36$, simulations are conducted in a Hilbert space incorporating the lowest 120 optical Fock states and 60 mechanical Fock states to mitigate truncation errors.

Figure 3.6 (a) depicts the fidelities of the final states for an optomechanical coupling $g_0 = \omega_m/26$. The theoretical fidelities display a monotonic increase with increasing evolution time across all driving strengths and align well with numerical fidelities when the maximum driving strength is $E_{\text{max}} \leq 5$. Within this regime, the maximum disparity between the numerical and theoretical fidelities is quantified as $\Delta F = 0.005$. However, when exposed to a higher maximum driving strength of $E_{\text{max}} = 6$, a subtle deviation between the numerical and theoretical fidelity values is observable, with the largest

discrepancy being $\Delta F = 0.012$. This increment in error serves as an indication of the perturbative assumption starting to falter.

Additionally, it is noteworthy that the fidelity errors depicted in Fig. 3.6 (a) revert to below the value $\Delta F = 0.005$ for $E_{\text{max}} = 6$ once the evolution time surpasses $t_{\text{f}} = 14\mathcal{T}$. This phenomenon can be attributed to the fact that only driven periods characterized by substantial driving strength (e.g. $E > 5\omega_{\text{m}}$) contribute to the error. However, as revealed by the optimized driving profiles showcased in Fig. 3.6 (a) for extended evolution times (i.e. $t_{\text{f}} \geq 14\mathcal{T}$), they converge into local minima associated with fewer periods of strong driving (refer to Appendix B.1). This outcome implies the advantage of adopting for low initial values of the driving strength E during the optimization process.

Figure 3.6 (b) delineates the fidelities of the final states with optomechanical coupling doubled to $g_0 = \omega_{\text{m}}/13$. Given that numerical simulations in subplot (a) already indicate a potential breakdown in the perturbative assumption at $E_{\text{max}} = 6$, the substantial deviations between theoretical and numerical fidelities witnessed in subplot (b) at maximum driving strengths exceeding $E_{\text{max}} = 3$ can be explained in the same manner. Nonetheless, subplot (b) reveals a discernible, though less pronounced, discrepancy between the two fidelity values even at the reduced driving strength of $E_{\text{max}} = 2$, with the maximal observed error being $\Delta F = 0.020$ at $t_{\text{f}} = 9\mathcal{T}$. This observation implies that terms of higher order in coupling strength, but not in driving strength, such as $H_{\text{eff}}^{(3)}$ in Eq. (3.29), contribute to the error. Conducting a numerical simulation of the dynamics induced by the effective Hamiltonian H_{eff} in Eq. (3.28) (i.e. including the third-order contribution) diminishes the fidelity error to $\Delta F = 0.016$ for $t_{\text{f}} = 9\mathcal{T}$. Beyond the impact of third-order processes alone, higher-order processes instigate mechanical excitations in the initial phase of the dynamics, consequently influencing the optical degree of freedom through third-order processes in the subsequent stages of the dynamics. A comprehensive examination of these effects would necessitate a detailed analysis of the fourth and higher-order terms in the effective Hamiltonian, which falls outside the purview of this thesis.

3.5 Experimental imperfections

While preceding sections primarily focused on the dynamics of closed systems and the limitations of perturbative methods, the interaction of the optomechanical system with surrounding environmental degrees of freedom (for example, see Fig. 3.7) also introduces imperfections in the preparation of the target state. The intracavity light field interacts with the extracavity field through a partially reflective mirror, which also permits the entry of the pump. The mechanical oscillator engages with the thermal environment either before the initiation of the target-state-preparation process (i.e. at $t < 0$) or during the state preparation (i.e. $t \in (0, t_{\rm f})$). The former interaction results in a thermal initial state, while the latter and the optical dissipation can be modeled through the master equation[6]

$$\dot{\rho} = -i[H_{\rm OM} + H_{\rm d}, \rho] + \sum_{j=1}^{4} \mathcal{D}_j \rho \,. \tag{3.32}$$

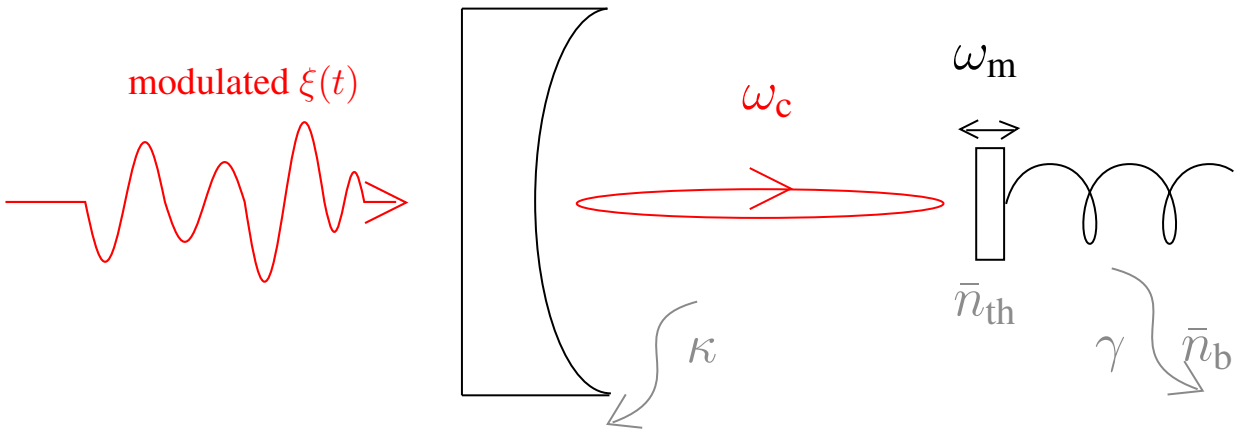


Figure 3.7: Optomechanical system considered in this section include optical dissipation, mechanical dissipations, or initial thermal occupation. The optical and mechanical dissipation rates are denoted as κ and γ, the thermal occupation of the heat bath related to mechanical dissipation is denoted as $\bar{n}_{\rm b}$, and the initial thermal occupation of the optomechanical oscillator is denoted as $\bar{n}_{\rm th}$.

Ideally, one would quantify the robustness of the state preparation in the presence of various imperfections by assessing the fidelities of the final states under corresponding experimental noises. However, technical constraints introduce further complexities, necessitating a more nuanced discussion before analyzing the robustness of the state preparation process.

The technical limitation stems from the necessity of employing the density matrix representation in-

[6]The equations is the same as in Eq. (2.30).

stead of the state vector representation to accommodate the classical mixedness of the system state in the presence of dissipation. This shift in representation, elevating the dimension from $n \times m$ to $n^2 \times m^2$, considerably hampers computational efficiency, particularly when the mechanical degree of freedom requires simulation within an expanded Hilbert space due to mechanical thermalization. To address this constraint, I formulate an approach to estimate the fidelity of the final state theoretically, as delineated in the subsequent procedure.

Generally, the master equation in Eq. (3.32) can be reformulated as follows:

$$\dot{\rho} = (\mathcal{H}_0 + \mathcal{H}_{\text{int}} + \mathcal{L})\rho \,, \tag{3.33}$$

where the superoperators $\mathcal{H}_j$ are defined by $\mathcal{H}_j\rho = -i[H_j, \rho]$ and are induced by the non-interaction Hamiltonian $H_0 = \omega_{\text{c}} a^\dagger a + \omega_{\text{m}} b^\dagger b + \xi(t)a^\dagger + \xi^*(t)a$ and the interaction Hamiltonian $H_{\text{int}} = -g_0 a^\dagger a(b^\dagger + b)$ respectively. The Lindbladian superoperator $\mathcal{L} = \sum_{j=1}^{4} \mathcal{D}_j$ is induced by the Lindblad operators defined in Eq. (2.31).

By adopting a procedure akin to the one in Sec. 2.4.1, the propagator of the open system can be expressed as $\mathcal{V}_{\text{tot}} = \mathcal{V}_0\mathcal{V}_1$. Here, the propagator $\mathcal{V}_0$ for the non-interacting part of the dynamics is defined by the equation $\mathcal{V}_0\rho = U_0\rho U_0^\dagger$ through the non-interaction unitary U_0 in Eq. (3.4) and the interaction propagator $\mathcal{V}_1$ is induced by the superoperator $\mathcal{H}_{\text{I}} + \mathcal{L}_{\text{I}}$ where

$$\begin{aligned} \mathcal{H}_{\text{I}}\rho &= -i[H_{\text{I}}, \rho] \,, \\ \mathcal{L}_{\text{I}} &= \sum_{j=1}^{4} \tilde{\mathcal{D}}_j \,, \end{aligned} \tag{3.34}$$

with the interaction Hamiltonian H_{I} defined in Eq. (3.5), $\tilde{\mathcal{D}}_j$ being the superoperators $\mathcal{D}_j$ with all instances of a ($a^\dagger$) replaced by $a + f(t)$ ($a^\dagger + f^*(t)$), with

$$f(t) = \int_0^t e^{i\omega_{\text{c}}\tau}\xi(\tau)d\tau \tag{3.35}$$

defined in Eq. (2.18). Provided the dissipation rates κ, γ are sufficiently small to satisfy the inequalities $\kappa g_0 T \ll 1$ and $\gamma g_0 T \ll 1$, the interaction propagator $\mathcal{V}_1$ can then be approximated by the product

$\mathcal{V}_{\text{diss}}\mathcal{V}_{\text{I}}$, with the non-dissipating superoperator $\mathcal{V}_{\text{I}}\rho = U_{\text{I}}\rho U_{\text{I}}^{\dagger}$ induced by the interaction Hamiltonian H_{I} and the dissipation propagator $\mathcal{V}_{\text{diss}}$ induced by the Lindbladian $\mathcal{L}_{\text{I}}$ in Eq. (3.34).

The propagator $\mathcal{V}_{\text{diss}}$ can be solved using the Magnus expansion (refer to Eq. (2.3)). The first-order Magnus term is given as follows

$$\mathcal{L}_{\text{eff}}T = T(\mathcal{D}[\sqrt{\kappa}a] + \mathcal{D}[\sqrt{\gamma(\bar{n}_{\text{b}}+1)}b] + \mathcal{D}[\sqrt{\gamma\bar{n}_{\text{b}}}b^{\dagger}] + \mathcal{D}[\sqrt{\lambda}(ae^{-i\psi} + a^{\dagger}e^{i\psi})]) \,, \tag{3.36}$$

with

$$\lambda = \frac{g_0^2E^2\gamma}{2\omega_{\text{m}}^4}\left(\frac{4}{\ln\left(1+\bar{n}_{\text{b}}^{-1}\right)} + (2\bar{n}_{\text{b}}+1)\right) \,. \tag{3.37}$$

Higher order terms from the second onward can be neglected if the inequalities $\kappa^2E^4T^2 \ll \omega_{\text{m}}^4$ and $\gamma^2E^4T^2 \ll \omega_{\text{m}}^4$ are satisfied. As a result, given that $\mathcal{V}_0(T) = 0$ (refer to Eq. (2.23) and Sec. 3.2.2), the propagator for each driven period can be found as

$$\mathcal{V}_{\text{tot}}(T) = e^{\mathcal{L}_{\text{eff}}T}\mathcal{V}_{\text{I}}(T) \,. \tag{3.38}$$

This implies that the total propagator over each mechanical period can be approximated by initially evolving the system using the Hamiltonian for the closed system for one period, followed by evolving the resultant state using the Lindbladian $\mathcal{L}_{\text{eff}}$ for another period. Analogously, the undriven half-periods of evolution for the open system can be approximated by first evolving the system with the closed-system Hamiltonian for half a period and then evolving the resultant state with the undriven Lindbladian $\mathcal{L}$ for another half a period.

With the above approximation, it becomes feasible to approximate the final state in an open system using solely the evolution operator $U_{\text{I}}(T)$, which can be solved using the Magnus expansion, the exact evolution operators for the undriven half period, and the exact Lindblad operators. To enhance the precision of the results, the ensuing analysis in this section employs a computer-generated Magnus expansion of the evolution operator U_{I} up to the fifth order in the coupling strength g_0.

The influence of system dissipation on state preparation can be assessed with the help of the open-system propagator $\mathcal{V}_{\text{tot}}(\boldsymbol{\gamma})$, where $\boldsymbol{\gamma} = \{\kappa, \gamma, \bar{n}_{\text{b}}\}$ denotes the vector of dissipation parameters. Within

this context, it is useful to define fidelity as the measure between any two density matrices, given by

$$F(\rho_1, \rho_2) = \mathrm{Tr}\left(\sqrt{\sqrt{\rho_1}\rho_2\sqrt{\rho_1}}\right) . \tag{3.39}$$

Given a vacuum initial state $\rho_0 = |0\rangle\langle 0| \otimes |0\rangle\langle 0|$, one can find the fidelity

$$F_{\mathrm{l}} = F(\mathcal{V}_{\mathrm{tot}}(\boldsymbol{\gamma})\rho_0, \rho_{\mathrm{tar}}) \tag{3.40}$$

between the final state $\mathcal{V}_{\mathrm{tot}}(\boldsymbol{\gamma})\rho_0$ and the target state ρ_{tar}. In comparison, the fidelity

$$F_{\mathrm{i}} = F(\mathcal{V}_{\mathrm{tot}}(\boldsymbol{\gamma})\rho_0, \mathcal{V}_{\mathrm{tot}}(\mathbf{0})\rho_0) \tag{3.41}$$

assesses the similarity between the final state in the presence of dissipation and its counterpart in an ideal, dissipation-free scenario. The fidelity F_{l} quantifies the imperfection of the driving profile, accounting for both errors from the perturbative expansion and those arising from system dissipation, while the fidelity F_{i} exclusively gauges the impact of system dissipation on the achieved state, independent of the target state. Together, these fidelities offer a comprehensive perspective on the robustness of system dissipations on the state preparation process.

While the prior discussion mainly focuses on system dissipation during the state preparation, similar arguments can be extended to the dynamics when the mechanical oscillator starts from a thermal initial state. In such a scenario, the fidelities F_{l} and F_{i} for a thermal intial state ρ_{th} can be expressed as

$$\begin{aligned} F_{\mathrm{l}} =& F(\mathcal{V}_{\mathrm{tot}}(0)\rho_{\mathrm{th}}, \rho_{\mathrm{tar}}) , \\ F_{\mathrm{i}} =& F(\mathcal{V}_{\mathrm{tot}}(0)\rho_{\mathrm{th}}, \mathcal{V}_{\mathrm{tot}}(0)\rho_0) . \end{aligned} \tag{3.42}$$

Subsequent sections delve deeper into the impacts of experimental noises. Specifically, the analysis is performed using control pulses deemed optimal for an ideal, noiseless system. Three example pairs of parameter values for coupling strength and evolution time are considered, namely $(\omega_{\mathrm{m}}/26, 16\mathcal{T})$, $(\omega_{\mathrm{m}}/21, 10\mathcal{T})$ and $(\omega_{\mathrm{m}}/16, 5\mathcal{T})$. For each of these sets, the maximum permissible driving strength is consistently set to be $E_{\mathrm{max}} = 4\omega_{\mathrm{m}}$, and the details of the optimized driving profiles for these sets can

be found in Appendix B.1. To reduce truncation errors, when mechanical thermalization is considered (i.e. in Sec. 3.5.1 and Sec. 3.5.3), the simulation is performed in a Hilbert space with up to 60 phonons, while the maximum number of photons is kept at 60.

3.5.1 Thermal initial states

This section primarily focuses on scenarios with dissipationless, unitary dynamics, but with the mechanical oscillator initially a thermal state, denoted as

$$\rho_{\text{th}}(\bar{n}_{\text{th}}) = \sum_{n=0}^{\infty} \frac{\bar{n}_{\text{th}}^{n}}{(\bar{n}_{\text{th}}+1)^{n+1}} |n\rangle\langle n| \,, \tag{3.43}$$

with $\bar{n}_{\text{th}}$ being the average phonon occupation number of the thermal state.

Figure 3.8 (a) presents the fidelities F_{l} of the final states, using thermal mechanical initial states $\bar{\rho}_{\text{th}}(\bar{n}_{\text{th}})$ and the driving profiles in Appendix B.1. For a thermal phonon occupation of zero (i.e. $\bar{n}_{\text{th}} = 0$), variations in the fidelities achieved by simulating the three optimized driving profiles arise from the inherent limitations of the theoretical model, as discussed in Sec. 3.4. In particular, the parameter set with the highest coupling strength ($g_0 = \omega_{\text{m}}/16$) resides in a domain where a pronounced deviation (specifically $1 - F_{\text{l}} = 0.108$) from the predictions of the perturbative approach is observed. While the fidelity F_{l} appears low, it remains to be determined if a strategy characterized by a short evolution time and high coupling strength displays enhanced resilience against undesired experimental noises. In these scenarios, target state preparations that are more resilient to system dissipations can be achieved through refined optimal control methodologies, potentially by extending the perturbative solution to higher orders.

When the mechanical initial state is not at its ground state, the fidelities of final states from all three driving profiles decrease significantly, reaching $F_{\text{l}} < 0.9$ when $\bar{n}_{\text{th}} > 4$. Although the probability of observing a two-photon Fock state within the cavity exceeds that from a coherent state (with $F \approx 0.520$), generating two-photon pure states would require conditional measurements on the oscillator. This again calls for in-depth analysis of higher-order terms in the perturbative solution. Consequently, the current theoretical framework is most effective when the oscillator approaches its ground state,

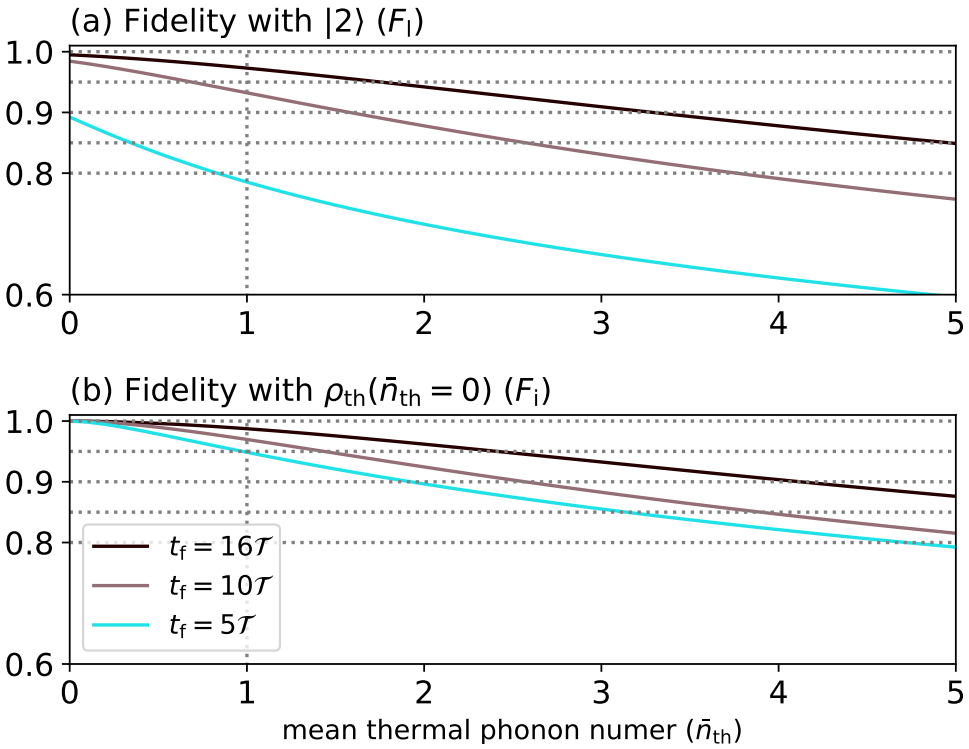


Figure 3.8: Plots of the fidelities (a) F_l and (b) F_i against mean thermal phonon numbers $\bar{n}_{th}$ of initial states for optimized driving profiles with parameters (g_0, E_{max}, t_f) equal to (i) $(\omega_m/26, 4\omega_m, 16\mathcal{T})$, (ii) $(\omega_m/21, 4\omega_m, 10\mathcal{T})$, and (iii) $(\omega_m/16, 4\omega_m, 5\mathcal{T})$, respectively. All fidelities remain higher than 0.9 when $\bar{n}_{th} < 1$ except for the case of $(\omega_m/16, 4\omega_m, 5\mathcal{T})$ where the fidelity F_l drops below 0.8. The exception may arise from the higher order entanglement that is amplified by excitations in the mechanical oscillator.

particularly when $\bar{n}_{th} < 1$, where the state fidelity for the driving profile at $t_f = 16\mathcal{T}$ remains above $F_l = 0.973$ and for $t_f = 10\mathcal{T}$, it remains above $F_l > 0.932$.

Figure 3.8 (b) illustrates the fidelities F_i of the final states given the same three driving profiles as in Fig. 3.8 (a). It can be observed that thermal excitations reduce the state fidelities stronger for faster protocols. This stems from the requirement of shorter dynamics to either have increased coupling strengths or driving strengths. Increasing either parameter results in larger coefficients for interaction terms, such as $H_{eff}^{(3)}$, in the perturbative solution given by Eq. (3.29). Any undesired interaction between the cavity and the oscillator gets amplified by a pronounced phononic occupation, leading to reduced final fidelities.

Lastly, the dynamics of the system for the quickest driving profile (i.e. when $t_f = 5\mathcal{T}$) are numerically simulated in a Hilbert space consisting a maximum number of 60 photons and 60 phonons. The results can be compared with the data in Fig. 3.8 as a benchmark of the theoretical approximation in Eq. (3.38).

Numerical simulation gives the fidelities with respect to the numerical result of final state in a closed system, reading $F_{\mathrm{i}} = 0.947, 0.891, 0.778$, when thermal occupation of the mechanical oscillator takes the values $\bar{n}_{\mathrm{th}} = 1, 2, 5$, respectively. The approximated fidelities presented in Fig. 3.8, on the other hand, have the values $F_{\mathrm{i}} = 0.949, 0.896, 0.792$, which are always larger than the numerical results and the difference between fidelities generated from the two methods increases as the thermal occupation of the mechanical initial state increases. However, when the thermal occupation $\bar{n}_{\mathrm{th}}$ is low, the difference between the two fidelities $\Delta F_{\mathrm{i}} \approx 0.002$ is negligible within the accuracy considered in this work. While the difference increases to $\Delta F_{\mathrm{i}} \approx 0.014$ for a larger thermal occupation $\bar{n}_{\mathrm{th}} = 5$, the inaccuracy is still insignificant compared to the infidelity $1 - F_{\mathrm{i}} > 0.2$ due to system dissipation. Similar to the fidelities F_i, the fidelities F_{l} with respect to the target state $|2\rangle$ are also compared between the two methods. Numerical simulation shows the fidelities $F_{\mathrm{l}} = 0.823, 0.753, 0.625$ and the approximation in Eq. (3.38) gives $F_{\mathrm{l}} = 0.785, 0.716, 0.596$ for thermal occupations $\bar{n}_{\mathrm{th}} = 1, 2, 5$ of the mechanical initial state, respectively. In contrast to the fidelity F_{i}, there is a consistent inaccuracy of the approximation method, which can be mostly attributed to the error as studied in Sec. 3.4. It is, however, noteworthy that this inaccuracy should have a minimal effect on the driving profile with the longest duration (i.e. when $t_{\mathrm{f}} = 16\mathcal{T}$) because the Magnus expansion has been proven to be accurate within this regime (refer to Sec. 3.3.1). In summary, I conclude that the approximation in Eq. (3.29), although not perfect, is sufficient for the analysis of the impact of thermal initial states on the state preparation process, especially for identification of the range of the thermal occupation when the given driving profiles remain robust.

3.5.2 Optical loss

In this section, I explore the effect of single-photon leakage from the cavity at a rate κ, which can be modelled using the Lindbladian $\mathcal{D}_1 = \mathcal{D}[\sqrt{\kappa}a]$ (refer to Eq. (2.31)). This source of dissipation can be particularly important not only because the theoretical model in Sec. 3.2 becomes less accurate when the dissipation becomes strong, but also because the scheme requires detuned driving. When the dissipation rate, or equivalently the cavity linewidth, becomes comparable to the detuning of the driving, the distinction between the detuned driving and an on-resonance driving blurs, thus undermining the

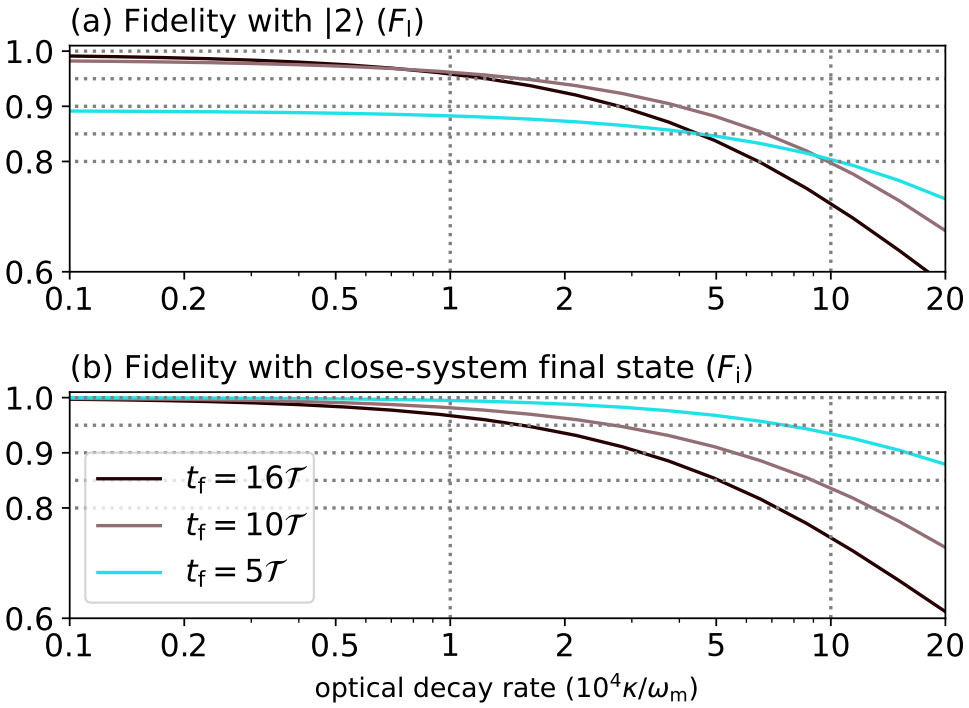


Figure 3.9: Plots of the fidelities (a) F_{l} and (b) F_{i} against relative optical decay rates $10^4\kappa/\omega_{\mathrm{m}}$ of the lossy cavity for optimized driving profiles with parameters $(g_0, E_{\mathrm{max}}, t_{\mathrm{f}})$ equal to (i) $(\omega_{\mathrm{m}}/26, 4\omega_{\mathrm{m}}, 16\mathcal{T})$, (ii) $(\omega_{\mathrm{m}}/21, 4\omega_{\mathrm{m}}, 10\mathcal{T})$, and (iii) $(\omega_{\mathrm{m}}/16, 4\omega_{\mathrm{m}}, 5\mathcal{T})$, respectively. The x-axis is in log scale while the y-axis is in linear scale. The plots suggest that the fidelity drops dramatically with the increase in optical decay rate when the decay rate exceeds $10^{-4}\omega_m$, and that shorter evolution time leads to a more resilient state.

entire proposed method. Given that an open cavity is imperative for injecting light, it is crucial to delineate a domain wherein the driven dynamics closely mirrors that in the idealized framework.

Figure 3.9 displays the fidelities F_{l} and F_{i} in relation to the optical decay rate κ, expressed in the units of $10^{-4}\omega_{\mathrm{m}}$. Just like in Fig. 3.8, the fidelities F_{l} remain below 1 even for vanishing decay rate (i.e. $\kappa \to 0$). However, unlike the scenario with initial thermal excitations, systems exhibiting stronger interactions and faster protocols become more advantageous as optical decay intensifies. In particular, Fig. 3.9 (a) indicates that although the driving profile with a shorter evolution time t_{f} results in considerably lower fidelity compared to the other profiles, the fidelity curves eventually intersect when optical dissipation approaches $\kappa \sim 10^{-3}\omega_{\mathrm{m}}$. This distinction from the case in Sec. 3.5.1 stems from the fact that the degree of imperfection in the latter (i.e., the thermal occupation number $\bar{n}_{\mathrm{th}}$) is independent of the evolution time t_{f}.

Given the driving profiles in Fig. 3.9 (a), to achieve fidelities surpassing $F_{\mathrm{l}} > 0.95$, the optical decay

rate should at most be on the order of $10^{-4}\omega_{\mathrm{m}}$. However, as shown in Fig. 3.9 (b), if an improved driving profile can be established for a shorter evolution time $t_{\mathrm{f}} = 5\mathcal{T}$ such that the two fidelities F_{i} and F_{l} are nearly equivalent, the acceptable optical decay can extend to almost one order of magnitude larger. While the best value achieved by current advancements [1] in the strong coupling regime is still one order of magnitude away from the required value, given the consistent progress over recent years, this desired regime could potentially be realized in future endeavors.

Lastly, similar to that in Sec. 3.5.1, the accuracy of the fidelities obtained from the theoretical approximation in Eq. (3.38) is compared to a full numerical simulation for the shortest driving profile. The fidelities F_{i} with the closed-system final state from full numerical simulation read $1.000, 0.995, 0.934$ for the cavity decay rates $\kappa/\omega_{\mathrm{m}} = 10^{-5}, 10^{-4}, 10^{-3}$, respectively. These values are close to the fidelities obtained from theoretical approximations, which read $1.000, 0.995, 0.937$, respectively. The fidelities F_{l} with the target state again differ between the numerical simulation and the theoretical approximation, with values $F_{\mathrm{l}} = 0.917, 0.908, 0.827$ and $F_{\mathrm{l}} = 0.891, 0.883, 0.803$ for the cavity decay rates $\kappa/\omega_{\mathrm{m}} = 10^{-5}, 10^{-4}, 10^{-3}$, respectively. The consistent errors (around $\Delta F_{\mathrm{l}} \approx 0.25$) between the two set of fidelities F_{l} under different cavity decay can be explained by the inaccuracy due to the Magnus expansion under strong driving. As a conclusion, the theoretical approximation in Eq. (3.38) is a sufficiently good approximation to recognize the range of cavity decay in which the proposed driving profiles remain robust.

3.5.3 Mechanical thermalisation

Finally, systems with zero optical decay rates but with non-negligible mechanical decay rates γ are considered. The thermalization of the mechanical oscillator can be modelled with the Lindbladian in either the standard master equation in Eq. (2.29) or the dressed-state master equation in Eq. (2.30), depending on the strength of the optomechanical coupling. Although the coupling strength $g_0 = \omega_{\mathrm{m}}/26$ may be sufficiently small such that the two master equations approximately equal, the strong optical driving interacts with the dissipation process to generate sizable photon dissipation at a rate $\propto \sqrt{E^2 g_0^2 \gamma}$ as discussed in Eq. (3.36). Therefore, the simulation in this section considers only the dressed-state master equation.

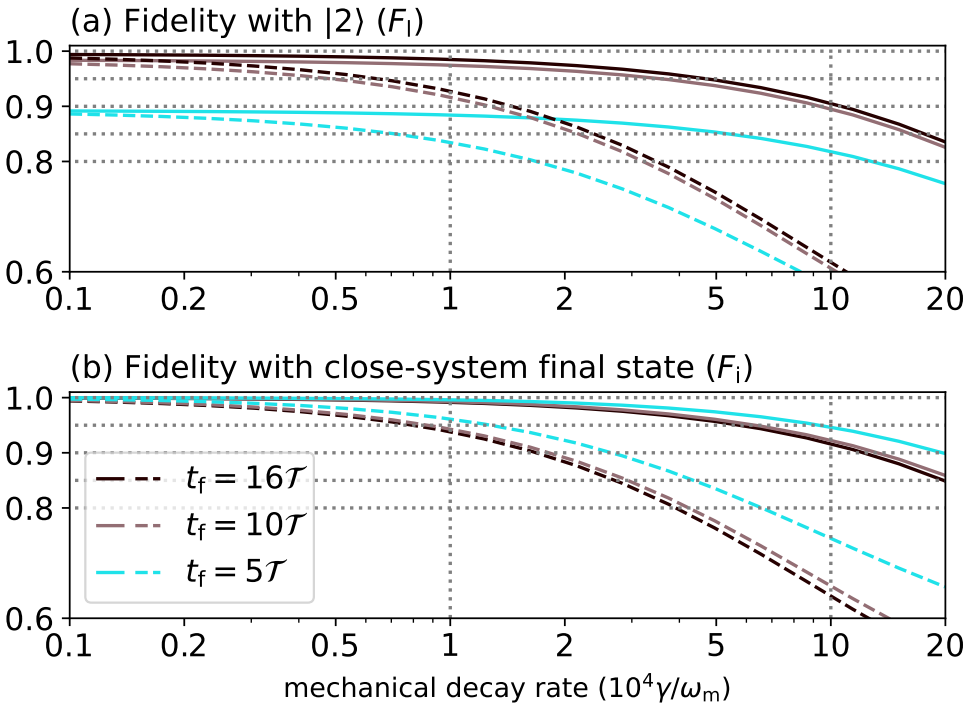


Figure 3.10: Plots of the fidelities (a) F_{l} and (b) F_{i} against relative mechanical decay rates $10^4\gamma/\omega_{\mathrm{m}}$ of the lossy cavity for optimized driving profiles with parameters $(g_0, E_{\max}, t_{\mathrm{f}})$ equal to (i) $(\omega_{\mathrm{m}}/26, 4\omega_{\mathrm{m}}, 16\mathcal{T})$, (ii) $(\omega_{\mathrm{m}}/21, 4\omega_{\mathrm{m}}, 10\mathcal{T})$, and (iii) $(\omega_{\mathrm{m}}/16, 4\omega_{\mathrm{m}}, 5\mathcal{T})$, respectively. Solid and dashed curves represent cases when the thermal bath contains on average $\bar{n}_{\mathrm{b}} = 1$ (solid), $\bar{n}_{\mathrm{b}} = 10$ (dashed) phonons respectively. The x-axis is in log scale and the y-axis is in linear scale. The plots suggest that the infidelity resulting from mechanical imperfection is negligible compared to that from optical imperfection when the thermal phonon number $\bar{n}_{\mathrm{b}} \ll 10$, but becomes noticeable otherwise.

The fidelities F_{l} and F_{i} are plotted in Fig. 3.10 (a) and (b) as functions of the mechanical decay rate γ. In addition, two different values of the mean thermal occupation number are considered, namely $\bar{n}_{\mathrm{b}} = 1, 10$ with thermal occupation number $\bar{n}_{\mathrm{b}}$ (defined in Eq. (2.32)). The plot Fig. 3.10 (b) indicates that faster protocols which require stronger optomechanical interactions are slightly favourable for higher F_{i} but the advantage is not significant when taking into the account the fact that faster protocols have lower fidelity in the dissipation-less case. Based on the plot (a), given fixed thermal bath occupation, the fidelity curves F_{l} for each driving profile do not intersect at any mechanical decay rates under consideration.

When the thermal bath contains 10 or less phonons, the effect of mechanical thermalization is completely negligible as compared to effect of optical decay when, as observed experimentally [29], the mechanical decay rate γ is significantly smaller than the optical decay rate κ. Especially when $\bar{n}_b \leq 1$,

a fidelity $F_{\mathrm{i}} > 0.95$ can be achieved with $\gamma < 10^{-3}\omega_m$ which can be realized under several existing experimental setups [29]. On the other hand, for systems that cannot maintain a low thermal phonon number $\bar{n}_b \leq 10$, the mechanical decay γ is required to be at least smaller than $10^{-4}\omega_m$ to reach a fidelity of $F_{\mathrm{i}} > 0.95$.

3.6 Conclusions and outlook

In this chapter, I have developed the tools for Fock-state preparation that serves to overcome the low success rates (less than 0.9 for two-photon Fock states [152]) of probabilistic protocols. Notably, while the nonlinear interaction between the light field and the mechanical oscillator inherently fosters growing entanglement between these systems, the driving patterns proposed in this chapter manage to generate near-ideal unitary dynamics of the light field while simultaneously ensuring that the virtues of the non-linear interactions are preserved for the realization of non-Gaussian states.

Beyond the discussed two-photon Fock and superposition states, the flexibility offered by pulse shaping also opens doors to a broader spectrum of non-Gaussian light states, beyond the two-photon Fock state and superposition states discussed here in more detail. This breadth of potential, when paired with the high fidelity achieved even amidst optical loss and mechanical heating, underscores the practical potential of our approach. It points towards the potential of deterministic state preparation in upcoming generations of optomechanical experiments, especially as stronger coupling between optical and mechanical components becomes possible.

While the driving protocols presented focus primarily on coherent optomechanical dynamics, the underpinning framework has the potential for broadening to accommodate dissipative dynamics. Such an extension could enrich our understanding by the optimization of the interplay of driving and environment engineering [153–155] and to provide insights into the dynamics of coupling light external to the cavity, as explored in studies like [40].

Chapter 4

Optomechanical nonclassical light in the presence of cavity dissipation

This chapter encompasses research I jointly conducted with my colleague, Sofia Qvarfort, at Stockholm University. The subjects discussed herein form the core content of a paper published in Physical Review Research with the title "Fast optomechanical photon blockade" [156].

4.1 Introduction

The discussion in Sec. 2.3.2 has outlined the limitations of generating optical nonclassical states using a simple driving field. To surpass the constraint of small driving strength while significantly minimizing phonon excitations, an optimized driving pattern was put forth in the last chapter. Nonetheless, it left the challenge of non-negligible system dissipation untouched. Consequently, the focus of this chapter will be on enhancing non-Gaussian state generation using an optimized driving pattern in an optomechanical system when a finite cavity linewidth is taken into account explicitly.

To illustrate the potential of optimal control in dissipative systems, this chapter focuses on improving the photon blockade effect in optomechanical systems. There is substantial literature on the photon blockade effect in optomechanical systems [43,145,146,157–163]. However, existing schemes achieve

the photon blockade effect only in the steady state, where pumping of the cavity and photon decay out of the cavity reach equilibrium. The time scale required for the preparation of a photon-blockaded state is thus at least as long as the lifetime of a photon in the cavity. In particular, in devices with a high-quality cavity, this poses a severe limitation to the repetition rate at which photon-blockaded quantum states can be prepared.

In order to exploit the photon blockade on shorter time scales, I explore the use of a suitably shaped bichromatic drive for the cavity. Rather than waiting for the occupation of two-photon states (or states with more photons) to decay, as is typically the case in schemes based on monochromatic driving, the dynamics resulting from bichromatic driving can lead to destructive interference of different amplitudes of the two-photon state. This chapter demonstrates that optimized bichromatic driving profiles can generate quantum states with an equal-time, second-order autocorrelation function value that is three orders of magnitude smaller than that achievable with monochromatic driving.

Before embarking on the details of the proposed approach, it is worth briefly mentioning a similar concept known as the unconventional photon blockade (UPB) [164–167]. In this process, additional degrees of freedom couple with the nonlinear cavity, which modifies the cavity's energy level structure. Consequently, the different pathways leading to two-photon occupation in the cavity interfere destructively. Although the fundamental physical concepts align, the additional degrees of freedom inevitably elevate the system's total dissipation rate. Given the necessity of weak driving amplitudes in UPB schemes, this increased dissipation rate typically results in lower single-photon population at steady states, which is an unnecessary compromise in this chapter's context. Moreover, existing literature primarily emphasizes UPB's potential for enhancing the quality of photon blockade at steady states, while this work underscores the efficacy of optimal control in the short-time regime. Finally, no known theory precludes the combined use of UPB and the approach proposed in this chapter, thereby potentially leveraging the benefits of both approaches as necessary.

The layout of this chapter is as follows. Section 4.2 introduces the model and presents the perturbative solution to the system dynamics in the short-time regime. Following that, numerical results are provided in Sec. 4.3. Throughout this section, the main focus is on the benefits and adaptability offered by the bichromatic driving. Several numerical examples are given to showcase possible improvements

in various aspects. In particular, the autocorrelation function when a monochromatic driving function is adopted is examined in Sec. 4.3.1, where it is shown that the monochromatic driving is insufficient for strong photon blockade at time scales shorter than the dissipation time scale. In Sec. 4.3.2, a comparison is made between monochromatic and bichromatic driving, demonstrating that a significantly stronger photon blockade can be achieved in the same timeframe with bichromatic driving. Crucially, in Sec. 4.3.3 and Sec. 4.3.4, it is shown that it is possible to increase the duration in which the autocorrelation function stays around its minimum value, as well as increasing the single-photon occupation at the cost of weaker photon blockade. Finally, Sec. 4.4 discusses the limits of the theory methods, pointing out areas that need further research and refinement.

4.2 Model and theory

4.2.1 Perturbative solution to the system dynamics

This chapter models an optomechanical system as depicted in Fig. 4.1. The model adopted in this chapter describes the optomechanical system through the Hamiltonian[1]

$$\begin{aligned} H_{\mathrm{OM}} =& \omega_{\mathrm{c}} a^\dagger a + \omega_{\mathrm{m}} b^\dagger b - g_0 a^\dagger a (b^\dagger + b) \\ H_{\mathrm{d}} =& \xi^*(t) a + \xi(t) a^\dagger \end{aligned} \tag{4.1}$$

with H_{OM} the bare optomechanical Hamiltonian and H_{d} the driving Hamiltonian. The scalar driving function $\xi(t)$ in the driving Hamiltonian H_{d} is flexible and can be chosen accordingly. Furthermore, the optomechanical system engages in dissipative coupling with the environment. There has been impressive progress in the reduction of mechanical dissipation in many optomechanical experiments [168–171], but the necessity to open the cavity to inject light implies a finite rate of photon loss from the cavity. The following discussion thus takes into account optical loss but neglects mechanical dissipation. The effects of mechanical dissipation are explored in Sec. 4.4.2.

The master equation for any state ρ undergoing optical loss at a rate κ can be derived from Eq. (2.29)

[1] The same equations as in Eq. (2.6) and Eq. (2.7), and in Sec. 3.2.

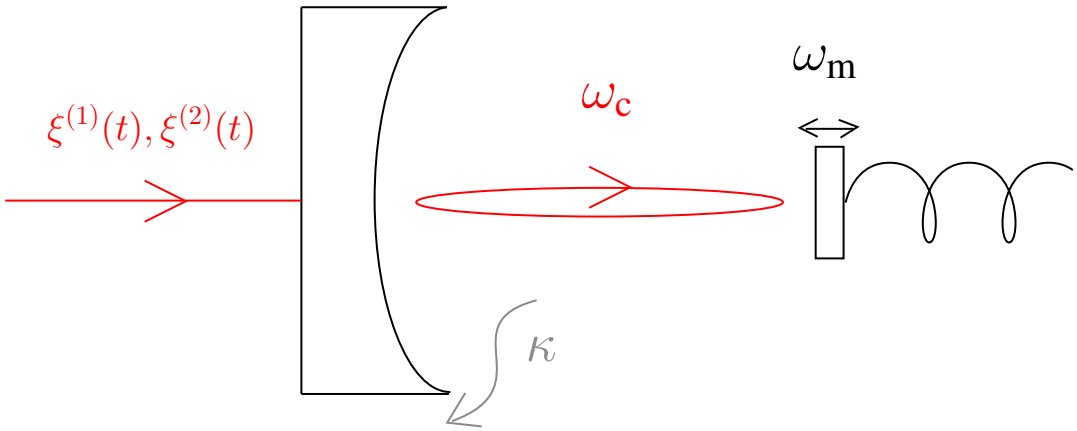


Figure 4.1: A schematic of the optomechanical system under consideration in this Chapter. The optomechanical cavity is driven by two coherent light sources with different temporal dependence. The optical dissipation (with rate κ) is explicitly included in the design of the driving, while the mechanical dissipation is neglected.

as follows:

$$\mathcal{L}\rho = -i[H_{\rm OM} + H_{\rm d}, \rho] + \mathcal{D}[\sqrt{\kappa}a]\rho \,, \tag{4.2}$$

with the Lindblad operator $\mathcal{D}$ as defined in Eq. (2.28). This equation serves as the initial step to resolve the time dependence of the photon statistics in optomechanical systems.

While it is possible to infer steady-state properties without solving the system dynamics, the objectives of this section necessitate an explicit solution to the system's equations of motion. Even though the dynamics of some system observables can be constructed in the presence of dissipation [172, 173], for the driven-dissipative system of interest in this discussion, this approach is not applicable. Consequently, it is necessary to construct these quantities through a perturbative approach. Perturbative solutions can then enable the identification of realizing photon-blockaded states as quickly as possible, which is the goal of this chapter.

To solve the dynamics, it is convenient to work in terms of the ladder superoperators defined by

$$a_{\rm L}\rho = a\rho \,, \qquad a_{\rm R}\rho = \rho a \,, \qquad b_{\rm L}\rho = b\rho \,, \qquad b_{\rm R}\rho = \rho b \,, \tag{4.3}$$

for any system state ρ. In this way, the master equation in Eq. (4.2) can be expressed as

$$\dot{\rho} = \left(\mathcal{L}_{\rm free} + \mathcal{L}_{\rm int} + \mathcal{L}_{\rm driv} + \mathcal{L}_{\rm jump} + \mathcal{L}_{\rm decay}\right)\rho \,, \tag{4.4}$$

with

$$\begin{aligned}
\mathcal{L}_{\text{free}} &= -i\left(\omega_{\text{c}}(a_{\text{L}}^{\dagger}a_{\text{L}} - a_{\text{R}}^{\dagger}a_{\text{R}}) + \omega_{\text{m}}(b_{\text{L}}^{\dagger}b_{\text{L}} - b_{\text{R}}^{\dagger}b_{\text{R}})\right) , \\
\mathcal{L}_{\text{int}} &= -ig_0\left(a_{\text{L}}^{\dagger}a_{\text{L}}(b_{\text{L}} + b_{\text{L}}^{\dagger}) - a_{\text{R}}^{\dagger}a_{\text{R}}(b_{\text{R}} + b_{\text{R}}^{\dagger})\right) , \\
\mathcal{L}_{\text{driv}} &= -i\left(\xi^{*}(t)a_{\text{L}} + \xi(t)a_{\text{L}}^{\dagger} - \xi^{*}(t)a_{\text{R}}^{\dagger} - \xi(t)a_{\text{R}}\right) , \\
\mathcal{L}_{\text{jump}} &= \kappa a_{\text{L}}a_{\text{R}} , \\
\mathcal{L}_{\text{decay}} &= -\frac{\kappa}{2}\left(a_{\text{L}}^{\dagger}a_{\text{L}} + a_{\text{R}}^{\dagger}a_{\text{R}}\right) .
\end{aligned} \tag{4.5}$$

The superoperators $\mathcal{L}_{\text{free}}$, $\mathcal{L}_{\text{int}}$, and $\mathcal{L}_{\text{driv}}$ respectively represent the free evolution, the optomechanical interaction, and the driving of the system. The superoperator $\mathcal{L}_{\text{jump}}$ denotes a quantum jump of the current state to a lower-lying state with one less photon, while the superoperator $\mathcal{L}_{\text{decay}}$ represents an exponential decay in the optical field amplitude [174, 175].

To solve the master equation in Eq. (4.4), it is useful to note that the generators can be divided into a photon-number-conserving term $\mathcal{L}_0 = \mathcal{L}_{\text{free}} + \mathcal{L}_{\text{int}} + \mathcal{L}_{\text{decay}}$, and a term $\mathcal{L}_1 = \mathcal{L}_{\text{driv}} + \mathcal{L}_{\text{jump}}$ which captures processes in which the photon number is not conserved. In the interaction picture, the time-evolution of the system can then be described by the following equation:

$$\rho(t) = \mathcal{S}_0(t)\mathcal{S}_1(t)\rho_0 , \tag{4.6}$$

with the propagator $\mathcal{S}_0$ describing the dynamics accounting for the dynamics induced by the photon-conserving term $\mathcal{L}_0$, the propagator $\mathcal{S}_1$ describing the photon-varying processes induced by the photon-varying term $\mathcal{L}_1$ in the frame defined by $\mathcal{S}_0$, and ρ_0 being the initial state of the system.

The dynamics governed by the photon-conserving term $\mathcal{L}_0$ can be determined exactly by solving the following differential equation:

$$\frac{d}{dt}\mathcal{S}_0(t)\rho_0 = \mathcal{L}_0\mathcal{S}_0(t)\rho_0 , \tag{4.7}$$

for any initial state ρ_0 of the system. The full analytic expression of the propagator $\mathcal{S}_0$ can be deduced from the exact solution to the closed system presented in Eq. (2.15), and reads as follows

$$\mathcal{S}_0(t) = \mathcal{S}_{\text{F}}(t)\mathcal{S}_{\text{D}}(t)\mathcal{S}_{\text{I}}(t)\mathcal{S}_{\text{K}}(t) \tag{4.8}$$

with propagators

$$\begin{aligned}
\mathcal{S}_{\mathrm{F}}(t) &= \exp\left(-i\omega_{\mathrm{c}}(a_{\mathrm{L}}^{\dagger}a_{\mathrm{L}} - a_{\mathrm{R}}^{\dagger}a_{\mathrm{R}})t\right)\exp\left(-i\omega_{\mathrm{m}}(b_{\mathrm{L}}^{\dagger}b_{\mathrm{L}} - b_{\mathrm{R}}^{\dagger}b_{\mathrm{R}})t\right) \,, \\
\mathcal{S}_{\mathrm{D}}(t) &= \exp\left(-\frac{\kappa}{2}(a_{\mathrm{L}}^{\dagger}a_{\mathrm{L}} + a_{\mathrm{R}}^{\dagger}a_{\mathrm{R}})t\right) \,, \\
\mathcal{S}_{\mathrm{I}}(t) &= \exp\left(f_1(t)(a_{\mathrm{L}}^{\dagger}a_{\mathrm{L}}b_{\mathrm{L}}^{\dagger} - a_{\mathrm{R}}^{\dagger}a_{\mathrm{R}}b_{\mathrm{R}}) - h.c.\right) \,, \\
\mathcal{S}_{\mathrm{K}}(t) &= \exp\left(if_2(t)\left((a_{\mathrm{L}}^{\dagger}a_{\mathrm{L}})^2 - (a_{\mathrm{R}}^{\dagger}a_{\mathrm{R}})^2\right)\right) \,,
\end{aligned} \tag{4.9}$$

and real, time-dependent functions

$$\begin{aligned}
f_1(t) &= \frac{g_0}{\omega_{\mathrm{m}}}(e^{i\omega_{\mathrm{m}}t} - 1) \,, \\
f_2(t) &= \left(\frac{g_0}{\omega_{\mathrm{m}}}\right)^2(\omega_{\mathrm{m}}t - \sin(\omega_{\mathrm{m}}t)) \,.
\end{aligned} \tag{4.10}$$

The remainder of the dynamics must be solved perturbatively. The generator $\tilde{\mathcal{L}}_1$ of the rest of the system dynamics in the frame defined by $\mathcal{S}_0$ is given by the equation

$$\tilde{\mathcal{L}}_1(t) = \mathcal{S}_0^{-1}(t)\mathcal{L}_1(t)\mathcal{S}_0(t) = -i(\xi^*\mathcal{A}_{\mathrm{L}} - \xi\mathcal{A}_{\mathrm{R}} + \xi\mathcal{A}_{\mathrm{L}}^{\dagger} - \xi^*\mathcal{A}_{\mathrm{R}}^{\dagger}) + \kappa\mathcal{A}_{\mathrm{L}}\mathcal{A}_{\mathrm{R}} \,, \tag{4.11}$$

in which

$$\begin{aligned}
\mathcal{A}_{\mathrm{L}} &= a_{\mathrm{L}}e^{-(\kappa/2+i\omega_{\mathrm{c}})t}e^{if_2(2a_{\mathrm{L}}^{\dagger}a_{\mathrm{L}}-1)}e^{f_1b_{\mathrm{L}}^{\dagger}-f_1^*b_{\mathrm{L}}} \,, \\
\mathcal{A}_{\mathrm{L}}^{\dagger} &= a_{\mathrm{L}}^{\dagger}e^{(\kappa/2+i\omega_{\mathrm{c}})t}e^{-if_2(2a_{\mathrm{L}}^{\dagger}a_{\mathrm{L}}+1)}e^{f_1^*b_{\mathrm{L}}-f_1b_{\mathrm{L}}^{\dagger}} \,, \\
\mathcal{A}_{\mathrm{R}} &= a_{\mathrm{R}}e^{(-\kappa/2+i\omega_{\mathrm{c}})t}e^{-if_2(2a_{\mathrm{R}}^{\dagger}a_{\mathrm{R}}-1)}e^{f_1^*b_{\mathrm{R}}^{\dagger}-f_1b_{\mathrm{R}}} \,, \\
\mathcal{A}_{\mathrm{R}}^{\dagger} &= a_{\mathrm{R}}^{\dagger}e^{(\kappa/2-i\omega_{\mathrm{c}})t}e^{if_2(2a_{\mathrm{R}}^{\dagger}a_{\mathrm{R}}+1)}e^{f_1b_{\mathrm{R}}-f_1^*b_{\mathrm{R}}^{\dagger}}
\end{aligned} \tag{4.12}$$

are the creation and annihilation superoperators in the frame defined by the superoperator $\mathcal{S}_0$. The propagator $\mathcal{S}_1$ induced by the generator $\tilde{\mathcal{L}}_1$ can be constructed perturbatively in the driving strength $\left|\xi(t)\right|$ and the optical decay κ using the Dyson expansion (refer to Sec. 2.2.1), which read as $\mathcal{S}_1 = \sum_{k=0}^{\infty}\mathcal{S}_1^{(k)}$. The zeroth order term $\mathcal{S}_1^{(0)}(t) = \mathbb{1}$ is the identity map, and the k-th order term $\mathcal{S}_1^{(k)}(t)$ (for $k > 0$) is given by

$$\mathcal{S}_1^{(k)}(t) = \int_{\boldsymbol{t}^{(k)}\in\mathbb{T}}\left(\prod_{j=1}^{k}\tilde{\mathcal{L}}_1(t_j)\right)d\boldsymbol{t}^{(k)} \,, \tag{4.13}$$

where $\boldsymbol{t}^{(k)} = (t_1, \ldots, t_k)$ is the vector of time-ordered time variables $t_1 > \ldots > t_k$ and $\mathbb{T}$ is the k-simplex domain $t > t_1 > \ldots > t_k > 0$.

Due to the time dependence of the propagator $\mathcal{S}_0$, it is generally not possible to evaluate the integrals in Eq. (4.13) analytically. However, to optimize the driving parameters for maximizing the strength of the photon blockade, it is sufficient to evaluate the occupation probabilities p_1 and p_2 (see discussion in Eq. (2.39)). These probabilities correspond to specific entries in the density matrix, which can be constructed without the need for explicit integration of the time-dependent superoperator $\tilde{\mathcal{L}}_1$ but rather through an integral of scalar functions. By employing established computational methods, the integral of this scalar function can be systematically evaluated, facilitating the determination of optimal driving parameters.

4.2.2 Dynamics of the autocorrelation function

Given the results in Eq. (4.8) and Eq. (4.13), the final state ρ_f can thus be written as

$$\rho_f = \sum_{k=0}^{\infty} \int_{\boldsymbol{t}^{(k)} \in \mathbb{T}} \left(\mathcal{S}_{\mathrm{F}}(t)\mathcal{S}_{\mathrm{D}}(t)\mathcal{S}_{\mathrm{I}}(t)\mathcal{S}_{\mathrm{K}}(t) \prod_{j=1}^{k} \tilde{\mathcal{L}}_1(t_j)\rho_0 \right) d\boldsymbol{t}^{(k)} \, . \tag{4.14}$$

This expression establishes a fundamental framework for understanding the system's evolution, and provides the means for solving the time dependence of the photon occupations, p_1 and p_2.

To proceed, it is helpful to represent the system states as a linear combination in the following form

$$\rho = \sum_{j=1}^{N} \left|n_{\mathrm{L},j}\right\rangle\!\left\langle n_{\mathrm{R},j}\right|_{\mathrm{c}} \otimes \left|\beta_{\mathrm{L},j}(t)\right\rangle\!\left\langle \beta_{\mathrm{R},j}(t)\right|_{\mathrm{m}} \, . \tag{4.15}$$

In each component, the optical part $|n_{\mathrm{L}}\rangle\langle n_{\mathrm{R}}|_{\mathrm{c}}$ is represented in the Fock basis with photons numbers $n_{\mathrm{L/R}}$, and the mechanical part $|\beta_{\mathrm{L}}(t)\rangle\langle\beta_{\mathrm{R}}(t)|_{\mathrm{m}}$ is represented via time-dependent coherent states with displacements $\beta_{\mathrm{L/R}}$. This approach significantly simplifies the analysis, as the final state, ρ_f, can always be expressed in terms of Eq. (4.15) with N being a finite number, whenever the infinite series in Eq. (4.14) is truncated to a finite number of terms.

To corroborate the statement, it suffices to write down the transformation of an arbitrary component $|n_{\mathrm{L}}\rangle\langle n_{\mathrm{R}}|_{\mathrm{c}} \otimes \left|\beta_{\mathrm{L}}(t)\right\rangle\!\left\langle\beta_{\mathrm{R}}(t)\right|_{\mathrm{m}}$ when acted on by each component of the propagators $\mathcal{S}_0$ and $\mathcal{S}_1$ as defined in Eq. (4.12) and Eq. (4.9). The transformations (omitting the time-dependence for brevity) are presented in the following equations:

$$
\begin{aligned}
\mathcal{A}_{\mathrm{L}}\,|n_{\mathrm{L}}\rangle\langle n_{\mathrm{R}}|_{\mathrm{c}} \otimes |\beta_{\mathrm{L}}\rangle\langle\beta_{\mathrm{R}}|_{\mathrm{m}} &= g_{\mathrm{L}}\,|n_{\mathrm{L}}-1\rangle\langle n_{\mathrm{R}}|_{\mathrm{c}} \otimes |\beta_{\mathrm{L}}+f_1\rangle\langle\beta_{\mathrm{R}}|_{\mathrm{m}}\ , \\
\mathcal{A}_{\mathrm{R}}\,|n_{\mathrm{L}}\rangle\langle n_{\mathrm{R}}|_{\mathrm{c}} \otimes |\beta_{\mathrm{L}}\rangle\langle\beta_{\mathrm{R}}|_{\mathrm{m}} &= g_{\mathrm{R}}\,|n_{\mathrm{L}}\rangle\langle n_{\mathrm{R}}-1|_{\mathrm{c}} \otimes |\beta_{\mathrm{L}}\rangle\langle\beta_{\mathrm{R}}+f_1|_{\mathrm{m}}\ , \\
\mathcal{S}_{\mathrm{F}}\,|n_{\mathrm{L}}\rangle\langle n_{\mathrm{R}}|_{\mathrm{c}} \otimes |\beta_{\mathrm{L}}\rangle\langle\beta_{\mathrm{R}}|_{\mathrm{m}} &= e^{-i\omega_{\mathrm{c}}(n_{\mathrm{L}}-n_{\mathrm{R}})t}\,|n_{\mathrm{L}}\rangle\langle n_{\mathrm{R}}|_{\mathrm{c}} \otimes \left|e^{-i\omega_{\mathrm{m}}t}\beta\right\rangle\!\left\langle e^{-i\omega_{\mathrm{m}}t}\beta\right|_{\mathrm{m}}\ , \\
\mathcal{S}_{\mathrm{D}}\,|n_{\mathrm{L}}\rangle\langle n_{\mathrm{R}}|_{\mathrm{c}} \otimes |\beta_{\mathrm{L}}\rangle\langle\beta_{\mathrm{R}}|_{\mathrm{m}} &= e^{-\kappa(n_{\mathrm{L}}+n_{\mathrm{R}})t/2}\,|n_{\mathrm{L}}\rangle\langle n_{\mathrm{R}}|_{\mathrm{c}} \otimes |\beta_{\mathrm{L}}\rangle\langle\beta_{\mathrm{R}}|_{\mathrm{m}}\ , \\
\mathcal{S}_{\mathrm{I}}\,|n_{\mathrm{L}}\rangle\langle n_{\mathrm{R}}|_{\mathrm{c}} \otimes |\beta_{\mathrm{L}}\rangle\langle\beta_{\mathrm{R}}|_{\mathrm{m}} &= e^{n_{\mathrm{L}}(f_1\beta_{\mathrm{L}}^*-\text{h.c.})/2}e^{n_{\mathrm{R}}(f_1^*\beta_{\mathrm{R}}^*-\text{h.c.})/2}\,|n_{\mathrm{L}}\rangle\langle n_{\mathrm{R}}|_{\mathrm{c}} \otimes |\beta_{\mathrm{L}}+f_1 n_{\mathrm{L}}\rangle\langle\beta_{\mathrm{R}}+f_1 n_{\mathrm{R}}|_{\mathrm{m}}\ , \\
\mathcal{S}_{\mathrm{K}}\,|n_{\mathrm{L}}\rangle\langle n_{\mathrm{R}}|_{\mathrm{c}} \otimes |\beta_{\mathrm{L}}\rangle\langle\beta_{\mathrm{R}}|_{\mathrm{m}} &= e^{if_2(n_{\mathrm{L}}^2-n_{\mathrm{R}}^2)}\,|n_{\mathrm{L}}\rangle\langle n_{\mathrm{R}}|_{\mathrm{c}} \otimes |\beta_{\mathrm{L}}\rangle\langle\beta_{\mathrm{R}}|_{\mathrm{m}}\ ,
\end{aligned}
\tag{4.16}
$$

where f_1 and f_2 are defined in Eq. (4.10) and

$$
\begin{aligned}
g_{\mathrm{L}} &= \sqrt{n_{\mathrm{L}}}e^{-(\kappa/2+i\omega_{\mathrm{c}})t}e^{if_2(2n_{\mathrm{L}}-1)}e^{(f_1\beta_{\mathrm{L}}^*-f_1^*\beta_{\mathrm{L}})/2}\ , \\
g_{\mathrm{R}} &= \sqrt{n_{\mathrm{R}}}e^{(-\kappa/2+i\omega_{\mathrm{c}})t}e^{-if_2(2n_{\mathrm{R}}-1)}e^{(f_1^*\beta_{\mathrm{R}}^*-f_1\beta_{\mathrm{R}})/2}\ ,
\end{aligned}
\tag{4.17}
$$

From Eq. (4.16), it can be deduced that the superoperators appeared in Eq. (4.14) map any finite linear combinations of the components $|n_{\mathrm{L}}\rangle\langle n_{\mathrm{R}}|_{\mathrm{c}} \otimes \left|\beta_{\mathrm{L}}(t)\right\rangle\!\left\langle\beta_{\mathrm{R}}(t)\right|_{\mathrm{m}}$ to another finite linear combination of similar components, albeit with potentially altered values of $n_{\mathrm{L/R}}$ and $\beta_{\mathrm{L/R}}$. As a result, given that the initial state is a special case when $n_{\mathrm{L/R}} = \beta_{\mathrm{L/R}} = 0$, the proof is thus complete.

An important consequence of the representation in Eq. (4.15) is that it allows for a direct extraction of occupation probabilities, p_1 and p_2, from finitely many components with $n_{\mathrm{L}} = n_{\mathrm{R}} = 1$ and $n_{\mathrm{L}} = n_{\mathrm{R}} = 2$, respectively. In the regime of weak driving where the inequality $|\xi|^2 \ll \omega_{\mathrm{m}}^2$ is satisfied, the leading order contribution to the single-photon occupation $p_1(t)$ appears in the second order (i.e. $k = 2$) of the perturbative series in Eq. (4.14) and reads

$$
p_1(t) = 2\,\mathrm{Re}\left(\int_{\boldsymbol{t^{(2)}}\in\mathbb{T}} f_{\mathrm{ee}}\,(+, t_1-t_2)\exp\left(-\frac{g_0^2}{\omega_{\mathrm{m}}^2}+\frac{\kappa}{2}(t_1+t_2-2t)\right)h^{(2)}(\boldsymbol{t^{(2)}})d\boldsymbol{t^{(2)}}\right)\ , \tag{4.18}
$$

(j,k) \ (i,l)	$(1,1)$	$(1,2)$	$(1,3)$	$(2,1)$	$(2,2)$	$(2,3)$
$(1,2)$	$-$	$+$	$+$	$+$	$-$	$+$
$(1,3)$	$+$	$-$	$+$	$-$	$+$	$+$
$(1,4)$	$+$	$+$	$-$	$-$	$+$	$+$
$(2,3)$	$+$	$+$	$-$	$-$	$-$	$-$
$(2,4)$	$+$	$-$	$+$	$-$	$-$	$-$
$(3,4)$	$-$	$+$	$+$	$-$	$-$	$-$

Table 4.1: The values of the sign variables $s_{j,k}^{(i,j)}$ in Eq. (4.21).

where

$$\begin{aligned} h^{(2)}(\boldsymbol{t^{(2)}}) &= \exp\left(i\frac{g_0^2}{\omega_{\mathrm{m}}}(t_2-t_1)\right)\zeta(t_1)\zeta^*(t_2)\,, \\ f_{\mathrm{ee}}(\pm,t) &= \exp\left(\pm\frac{g_0^2}{\omega_{\mathrm{m}}^2}\exp(i\omega_{\mathrm{m}}t)\right) \end{aligned} \tag{4.19}$$

and $\mathrm{Re}(\cdot)$ denotes the real part of the expression, $\zeta(t)=\xi(t)\exp(i\omega_c t)$ denotes the driving function in the frame rotating at the cavity resonance frequency, and the vector $\boldsymbol{t^{(4)}}=(t_1,t_2,t_3,t_4)$ of time-ordered variables and the domain $\mathbb{T}$ are defined in Eq. (4.13). The leading order contribution to two-photon occupation $p_2(t)$ at time t appears in the fourth order (i.e. $k=4$) of the series in Eq. (4.14) and can be written as

$$p_2(t)=4\,\mathrm{Re}\int_{\boldsymbol{t^{(4)}}\in\mathbb{T}}\exp\left(-\frac{2g_0^2}{\omega_{\mathrm{m}}^2}+\frac{\kappa}{2}(t_1+t_2+t_3+t_4-4t)\right)\sum_{j=1}^{3}h_j(\boldsymbol{t^{(4)}})d\boldsymbol{t^{(4)}}\,, \tag{4.20}$$

with the time-dependent functions $h_j(t,\boldsymbol{t^{(4)}})$ defined as

$$\begin{aligned} h_1(\boldsymbol{t^{(4)}}) =& h(\boldsymbol{t^{(4)}},1)\zeta^*(t_1)\zeta^*(t_2)\zeta(t_3)\zeta(t_4)\,, \\ h_2(\boldsymbol{t^{(4)}}) =& h(\boldsymbol{t^{(4)}},2)\zeta^*(t_1)\zeta(t_2)\zeta^*(t_3)\zeta(t_4)\,, \\ h_3(\boldsymbol{t^{(4)}}) =& h(\boldsymbol{t^{(4)}},3)\zeta(t_1)\zeta^*(t_2)\zeta^*(t_3)\zeta(t_4)\,, \end{aligned} \tag{4.21}$$

and

$$h(\boldsymbol{t^{(4)}},l)=\prod_{1\le j<k\le 4}f_{\mathrm{ee}}\left(s_{j,k}^{(1,l)},s_{j,k}^{(2,l)}(t_j-t_k)\right)\exp\left(-i\frac{g_0^2}{\omega_{\mathrm{m}}}s_{j,k}^{(1,l)}s_{j,k}^{(2,l)}(t_j-t_k)\right)\,, \tag{4.22}$$

and the expressions $s_{j,k}^{(i,l)}$ are either positive or minus sign as defined in Table 4.1.

The analytical results of the photon populations, p_1 and p_2, provide a practical method for identifying the value of the autocorrelation[2]

$$\tilde{g}^{(2)}(t) = \frac{2p_2(t)}{(p_1(t) + 2p_2(t))^2} \,, \tag{4.23}$$

This, in turn, reveals the explicit dependence of the photon blockade on the driving parameters.

While it is already possible to perform numerical optimization of the driving parameters to maximize the strength of photon blockade, an additional step to enhance numerical efficiency is possible through approximating the double exponential function f_{ee} in the integrand using an analytically integrable form. By adopting this approach, the inherent inefficiencies often associated with numerical integration of multiple integrals can be effectively circumvented. Because in a photon blockade scheme that relies on the unequal spacing between distinct energy levels, the optomechanical coupling g_0 is required to be sufficiently smaller than the mechanical frequency ω_{m} (see discussion in Sec. 2.3.2 for more details), it is therefore guaranteed that the inequality $g_0^4/\omega_{\text{m}}^4 \ll 1$ is satisfied. Therefore, one can expand the double exponential to first order as

$$f_{\text{ee}}(\pm, t) \approx 1 + \left(\pm \frac{g_0^2}{\omega_{\text{m}}^2} \exp(i\omega_{\text{m}} t) \right) + O\left(\frac{g_0^4}{\omega_{\text{m}}^4} \right) \,, \tag{4.24}$$

leading to a manageable formula for the autocorrelation $\tilde{g}^{(2)}$. While the resultant formula is excessively complex for inclusion within the main body of the text, it is available online for further examination [176].

4.3 Numerical results

The goal ahead is to identify driving patterns that make the system evolve towards a state with a minimal value of the autocorrelation $g^{(2)}$ at a desired point in time. This is achieved using the analytic dependence of the approximate autocorrelation function $\tilde{g}^{(2)}$ on the driving profile $\xi(t)$ derived in Sec. 4.2.2.

[2] Same definition as in Eq. (2.39).

Since most of the earlier works focused on monochromatic driving

$$\xi_1(t) = Ee^{-i(\omega_c+\Delta)t} , \tag{4.25}$$

with driving strength E and detuning Δ from the cavity resonance frequency, this situation is relevant for comparison. The main focus of the subsequent discussion, however, is on the bichromatic driving

$$\xi_2(t) = E_1 e^{-i(\omega_c+\Delta_1)t} + E_2 e^{i\psi} e^{-i(\omega_c+\Delta_2)t} , \tag{4.26}$$

with two driving amplitudes E_j, corresponding detunings Δ_j, and a phase difference ψ between the two driving components.

The construction of the optimized driving patterns is based on the system ground state $\rho_0 = |0\rangle\langle 0|_c \otimes |0\rangle\langle 0|_m$ as the initial state. Even though the approximate autocorrelation function $\tilde{g}^{(2)}$ is given as an analytic function of all system parameters including the Fourier components of the driving profile ξ, the actual optimization of the drive cannot be performed analytically. In all the subsequent examples, numerical optimization is performed with Mathematica [177].

The validity of all results obtained based on perturbative treatments is verified through comparison with numerically exact solutions. Numerical simulations are performed with Qutip [148, 149] in a Hilbert space truncated to include up to 6 photons and 15 phonons.

Since the explicit shape of the driving patterns identified as optimal is not necessarily insightful on its own, it is not specified directly in the subsequent discussion. For completeness, however, the optimized numerical values of the parameters in the driving functions ξ_1 and ξ_2 can be found in Appendix B.2.

4.3.1 Monochromatic driving

For comparison with the results obtained with bichromatic driving discussed below in Sec. 4.3.2, this section is focused on the photon-blockaded states that can be realized with monochromatic driving. In particular, it can be found that, within the perturbative regime ($(g_0/\omega_m)^4, (E/\omega_m)^2 \ll 1$), monochromatic driving in Eq. (4.25) is insufficient for strong photon blockade in the time limit $t \ll 1/\kappa$.

Figure 4.3 plots the values of the autocorrelation function $g^{(2)}(t_{\rm op})$ from the full numerical simulation as a function of the target time $t_{\rm op}$. For each data point, the drive detuning Δ is optimized to minimize the approximate autocorrelation function $\tilde{g}^{(2)}(t_{\rm op})$ at the target time $t_{\rm op}$. In addition, a range of coupling strength ($g_0 = 0.3\omega_{\rm m}, \ldots, 0.6\omega_{\rm m}$) are also considered while other parameters are kept constant $(E, \kappa) = (\omega_{\rm m}/200, \omega_{\rm m}/50)$.

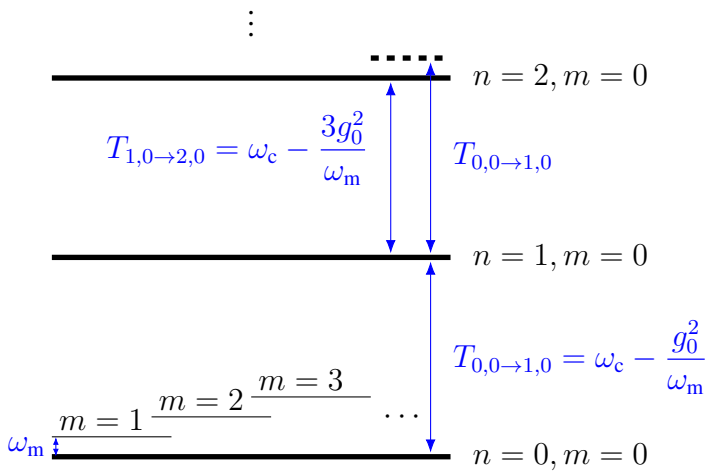


Figure 4.2: A replicate of the optomechanical energy-level diagram in Fig. 2.2.

The strength of photon blockade depends on the optomechanical coupling strength g_0. This can be confirmed by the data points corresponding to different coupling strength g_0 for each fixed target time $t_{\rm op}$ in Fig. 4.3. The minimized values of the autocorrelation function decrease as the coupling strength g_0 increases until it reaches the value $g_0 = 0.5\omega_{\rm m}$. The primary factor contributing to the increase in the autocorrelation is the proportionality of the difference between the transitions in the unevenly spaced energy spectrum (as depicted in Fig. 4.2 and discussed in Sec. 2.3.2) to the square of the coupling strength, which is formally expressed as $T_{n,m\to n+1,m} \propto g_0^2$ (refer to Eq. (2.12)). As the coupling strength increases further (e.g. $g_0 \geq 0.6\omega_{\rm m}$, starred points in Fig. 4.3), the energy required to pump a single photon into the cavity is eventually approached by the energy required to pump a second photon and an extra phonon into the cavity (i.e. $T_{1,0\to2,1} = T_{0,0\to1,0}$), and thus the photon blockade effect vanishes [43]. This can be confirmed by the increase in the autocorrelation function for larger coupling strength ($g_0 > 0.5\omega_{\rm m}$). The increase in the autocorrelation for larger coupling strength is also consistent with the fact that the assumption of small coupling strength (i.e. $(g_0/\omega_{\rm m})^4 \ll 1$) in Eq. (4.24) is violated close to the value $g_0 = 0.5\omega_{\rm m}$, but the errors only contribute to a small portion

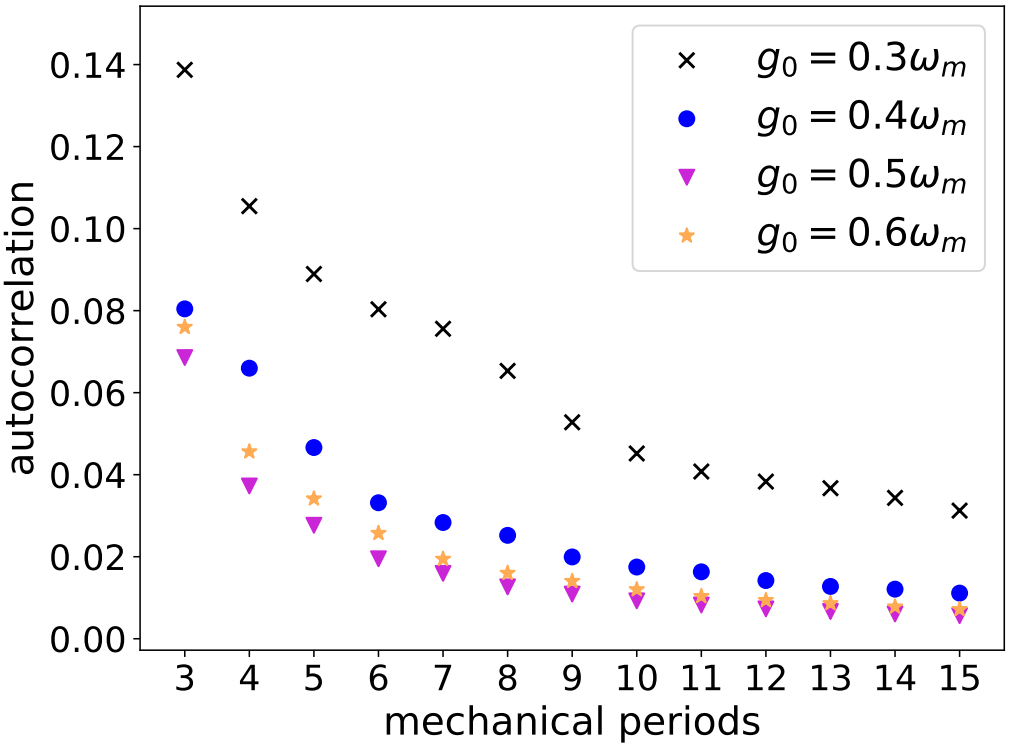


Figure 4.3: The value of the autocorrelation function $g^{(2)}$ as a function of the target time $t_{\rm op}$ in terms of mechanical periods ($T = 2\pi/\omega_{\rm m}$) when the approximate autocorrelation function $\tilde{g}^{(2)}(t_{\rm op})$ is minimized with respect to the drive detuning Δ at the considered time $t_{\rm op}$. Different values of the optomechanical coupling strength $g_0 = 0.3\omega_{\rm m}$ (cross), $g_0 = 0.4\omega_{\rm m}$ (circle), and $g_0 = 0.5\omega_{\rm m}$ (triangle) and $g_0 = 0.6\omega_{\rm m}$ (star) are considered. The driving strength is $E = \omega_{\rm m}/200$ and the cavity decay rate is $\kappa = 0.02\omega_{\rm m}$. The minimized autocorrelation function decreases when either the driving strength or the evolution time increases, but strong photon blockade ($g^{(2)} \sim 10^{-4}$) cannot be observed within the range of parameters considered.

of the increase.[3]

Furthermore, Fig. 4.3 also shows that monochromatic driving is insufficient for strong photon blockade for any target time within the first 15 mechanical periods. A close examination of the data points corresponding to different target time $t_{\rm op}$ for each fixed coupling strength g_0 reveals that the minimized values of the autocorrelation function $g^{(2)}(t_{\rm op})$ decrease monotonically as the target time $t_{\rm op}$ increases. Despite this decrease, the best value ($\sim 10^{-2}$) of the autocorrelation function that can be obtained within the first 15 mechanical periods ($T = 2\pi/\omega_{\rm m}$) is still far from the value ($g^{(2)} \lesssim 10^{-4}$) that can be achieved using a bichromatic drive scheme.

[3]The error of the theoretical values relative to the numerical values increases from 1.4% to 5.1% as the target time $t_{\rm op}$ increases from $3T$ to $15T$. However, the relative difference between the autocorrelation for coupling strength with values $g_0 = 0.5$ and $g_0 = 0.6$ ranges from 11% to 32% which are one order of magnitude larger than the relative difference between analytical results and numerical results.

4.3.2 Bichromatic driving

It is possible to induce a stronger fast photon blockade given an optimized bichromatic drive. To compare a bichromatic drive with a monochromatic drive, the time-evolution of the equal-time autocorrelation function $g^{(2)}(t)$ is plotted in Fig. 4.4 as a function of time t. Figure 4.4(a) shows the autocorrelation $g^{(2)}$ for the bichromatic drive, while Fig. 4.4(b) shows the autocorrelation $g^{(2)}$ for a monochromatic drive. In addition to the autocorrelation $g^{(2)}$, the single- and two-photon occupation numbers p_1 and p_2 are plotted to demonstrate the difference in the time evolution of the optical subsystem between the two cases. The cavity decay rate is set to $\kappa = \omega_{\mathrm{m}}/50$, as in Sec. 4.3.1. The coupling strength is fixed to $g_0 = 0.3\omega_{\mathrm{m}}$, which is less than the optimal value ($g_0 \approx 0.5\omega_{\mathrm{m}}$) in Fig. 4.3.[4] The driving strength for each component is kept constant as $E_1 = E_2 = \omega_{\mathrm{m}}/200$. In both plots, the detunings take the optimized values $\Delta = -0.040\omega_{\mathrm{m}}$, $\Delta_1 = -0.019\omega_{\mathrm{m}}$ and $\Delta_2 = -0.028\omega_{\mathrm{m}}$ and the relative phase of the bichromatic drive takes the optimized value $\psi = 2.8$ so that the approximate autocorrelation $\tilde{g}^{(2)}$ reaches its minimum around $t_{\mathrm{op}} = 5T$. This target time was chosen because it is close to the minimal time required to achieve the autocorrelation value $g^{(2)}(t_{\mathrm{op}}) \lesssim 10^{-4}$. The optimized values can be found in Appendix B.2.

From Fig. 4.4, it can be seen that much lower values of the autocorrelation $g^{(2)}$ can be achieved with the bichromatic drive. The evolution plotted in Fig. 4.4(a) shows a second-order autocorrelation of value $g^{(2)}(5T) \approx 5.8 \times 10^{-5}$ at the end of the fifth mechanical period, which is three orders of magnitude smaller than the best possible value for a monochromatic driving (see Sec. 4.3.1) $g^{(2)}(5T) \approx 8.9\times10^{-2}$ shown in Fig. 4.4(b). The significant enhancement in the strength of the photon blockade effect demonstrates the benefit of adopting an optimized bichromatic driving. Furthermore, it can be observed that the single-photon occupation p_1 also increases monotonically in both subplots but the two-photon occupation only shows a rapid decrease near the 5-th mechanical period when a bichromatic driving is adopted. This supports the argument in Sec. 4.1 that the entry of the second drive induces strong destructive interference only between different transition paths to the two-photon Fock state without affecting the single-photon occupation. It is also worth noticing that the low autocorrelation value $g^{(2)}(5T) \approx 5.8 \times 10^{-5}$ is achieved given a coupling strength g_0 weaker than the optimal value indi-

[4] This is to ensure that the assumption of small coupling strength (i.e. $(g_0/\omega_{\mathrm{m}})^4 \ll 1$) is satisfied with an error less than 0.01.

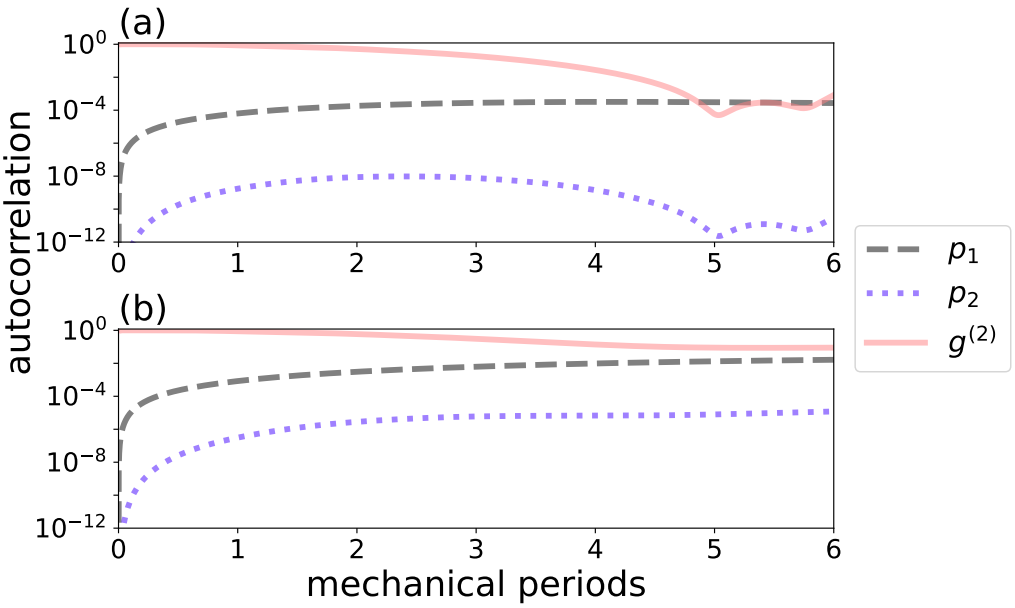


Figure 4.4: Single-photon occupation p_1 (dashed), two-photon occupation p_2 (dotted) and autocorrelation function $g^{(2)}$ (solid) as functions of time for parameters that minimize the autocorrelation function at the 5-th mechanical period when the parameters have the values $E = \omega_{\mathrm{m}}/200$, $g_0 = 0.3\omega_{\mathrm{m}}$, $\kappa = 0.02\omega_{\mathrm{m}}$, and the drive detuning and phases are optimized. Subplot (a) corresponds to the dynamics when the driving is bichromatic and strong photon blockade ($g^{(2)} \sim 10^{-4}$) can be observed at $5T$. Subplot (b) corresponds to the dynamics when the driving is monochromatic and the lowest value of the autocorrelation function only reaches 10^{-1}.

cated by Fig. 4.3, which suggests a further advantage of adopting a bichromatic driving.

It can also be noticed that in Fig. 4.4, the single-photon populations p_1 for the two subplots are different. However, the comparison of the intracavity photon numbers is not insightful. This is because the compound driving strength $\left|\xi_2(t)\right|$ (refer to Eq. (4.26)) of a bichromatic drive is dynamic in contrast to the time-independent driving strength $\left|\xi_1(t)\right| = E$ of a monochromatic drive. Therefore, the compound driving strength $\left|\xi_2(t)\right|$ of a bichromatic drive can be much weaker than that of a monochromatic drive even if the driving strengths of the components are equal (i.e. $E_1 = E_2 = E$). On the other hand, the autocorrelation $g^{(2)}$ does not suffer from the same problem. As long as the driving strengths for the two driving components are equal and weak (i.e. $E_1 = E_2 \ll \omega_{\mathrm{m}}$), the value of the approximate autocorrelation function $\tilde{g}^{(2)}$ to leading order becomes independent of the driving strength. Therefore, the value of the exact autocorrelation function $g^{(2)}$ is independent of the driving strength given the validity of the perturbative method. Further discussion of this point can be found in Sec. 4.4.3.

Although the driving function is the only degree of freedom to be optimized, other system parameters

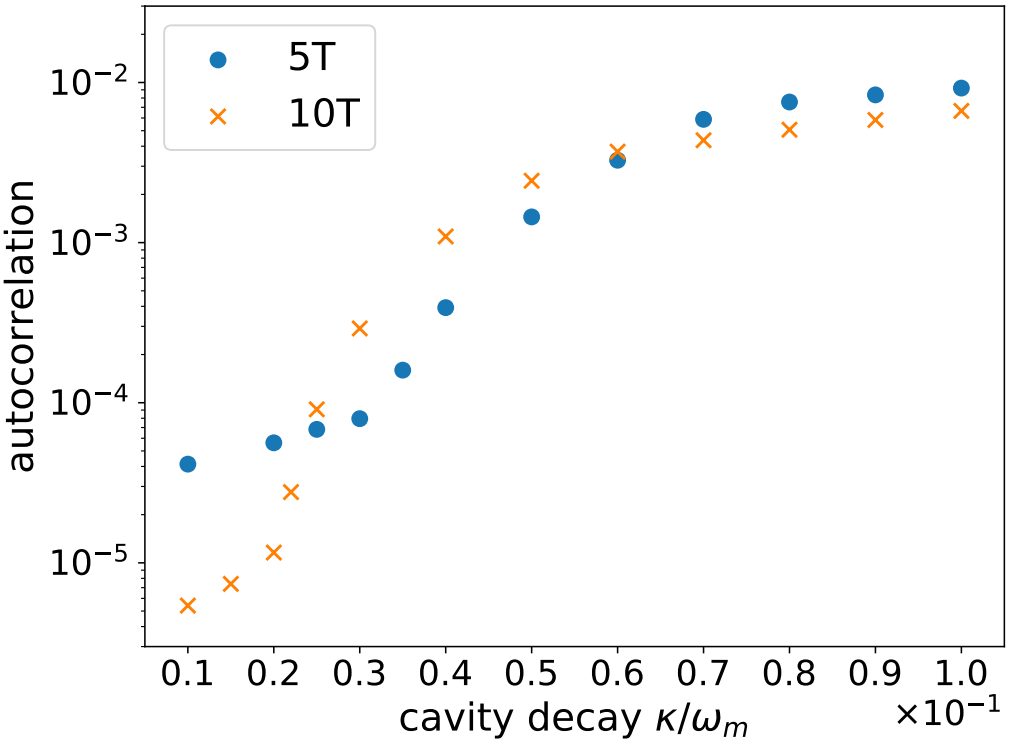


Figure 4.5: The minimal value of autocorrelation function against the relative cavity decay rate $\kappa/\omega_{\mathrm{m}}$ when $t_{\mathrm{op}} = 5T$ (circle) and $t_{\mathrm{op}} = 10T$ (cross). The driving strength is $E = \omega_{\mathrm{m}}/200$ and optomechanical coupling rate is $g_0 = 0.3\omega_{\mathrm{m}}$. The minimal values of the autocorrelation function increase as the cavity decay increases, but do not have a monotonic dependence on the evolution time.

also need to be kept within a suitable range for the strong photon blockade to occur. Especially, the cavity decay rate has a strong influence on $g^{(2)}$. To explore the behaviour of the $g^{(2)}$-function as the cavity decay κ increases, the minimized values of the autocorrelation function $g^{(2)}(t_{\mathrm{op}})$ are plotted in Fig. 4.5. Two different evolution times are considered, namely $t_{\mathrm{op}} = 5T$ (blue circles) and $t_{\mathrm{op}} = 10T$ (orange crosses). The optomechanical coupling is kept at $g_0 = 0.3\omega_{\mathrm{m}}$ and the driving is $E_1 = E_2 = \omega_{\mathrm{m}}/200$ as before. For each point, Δ_1, Δ_2 and ψ have been optimized such that $g^{(2)}$ reaches its lowest value.

From studying Fig. 4.5, it is clear that the minimal value of the autocorrelation function $g^{(2)}$ stays below 10^{-4} as long as the cavity linewidth remains below $\kappa \sim 0.03\omega_{\mathrm{m}}$. However, as κ becomes comparable to the optomechanical coupling g_0, the unequal spacings between different energy levels, as depicted in Fig. 4.2 are no longer distinguishable by the cavity, and thus the photon blockade effect eventually vanishes for large κ.

It is also noticeable from Fig. 4.5 that a longer evolution time does not necessarily lead to a lower min-

imal $g^{(2)}$. This is in sharp contrast with the monochromatic case, as seen in Fig. 4.4. Such a feature can be explained by the fact that the occurrence of the minimum of $g^{(2)}$ depends on the destructive interference between the two driving fields and it is not guaranteed that a longer evolution time enhances the destructive interference between the two driving tones.

While it is generally important to minimize the autocorrelation function, there are other aspects that can be further improved. They are explored in the following sections.

4.3.3 Extending the lifetime of photon blockade driving

The results presented in the previous section show the desired low values of the autocorrelation function $g^{(2)}$, which indicate strong photon blockade. Besides strong photon blockade, it is also helpful to extend the duration for which the photon-blockaded state can be accessed or equivalently, the duration in which the autocorrelation function stays at its minimum value. In this section, it is shown that the maximization of this duration can be achieved at the same time when the strength of photon blockade is maximized.

A broader minimum of the autocorrelation can be achieved by minimizing the following target function

$$\eta_1 = \left(1 + w_\mathrm{d}\frac{d}{dt} + w_\mathrm{s}\frac{d^2}{dt^2}\right)\tilde{g}^{(2)}(t_\mathrm{op})\,, \tag{4.27}$$

with scalar weights w_d and w_s. The minimization of the first-order derivative then guarantees that the local minimum of the autocorrelation function is located in the vicinity of the given time t_op. A minimal second-order derivative then assures that the vanishing first-order derivative stays at a low value around the given time t_op.

Figure 4.6 demonstrates that this choice of target function produces the desired result. A bichromatic driving is optimized for a flat minimum with fixed weights $w_\mathrm{d} = 1$ and $w_\mathrm{s} = 10$ and the other system parameters are chosen to be $(E_1, E_2, g_0, \kappa, t_\mathrm{op}) = (\omega_\mathrm{m}/200, \omega_\mathrm{m}/200, 3\omega_\mathrm{m}/10, \omega_\mathrm{m}/50, 5T)$ in accordance with Fig. 4.4. The weight w_s for the second-order derivative is chosen to be larger in order to prioritize the maximization of the width of the minimum. As can be noted from Fig. 4.6, the optimized

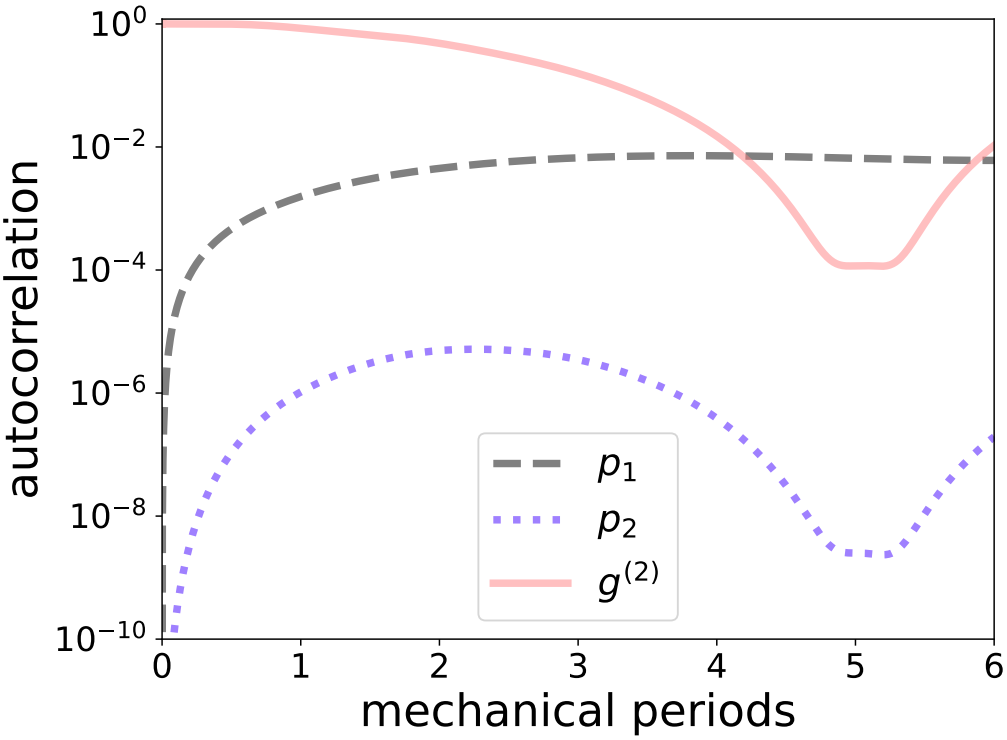


Figure 4.6: Single-photon occupation p_1 (dashed), two-photon occupation p_2 (dotted) and autocorrelation function $g^{(2)}$ (solid) as functions of time for parameters that minimize the target function Eq. (4.27) at 5-th mechanical period when the parameters have the values $E = \omega_m/200$, $g_0 = 0.3\omega_m$ and $\kappa = 0.02\omega_m$. The autocorrelation function stays around its minimum for approximately 0.2 mechanical periods.

driving in Fig. 4.6 makes the autocorrelation stay within $\pm 5\%$ of its value at the target time $t_{op} = 5T$ for 0.38 mechanical periods as compared to 1.1×10^{-2} mechanical periods in Fig. 4.4. The improvement is more than one order of magnitude, which suggests that the target function η_1 in Eq. (4.27) correctly predicts the desired driving function that widens the minimum.

There are however drawbacks to the optimization for broader minima. As a trade-off, the value of the autocorrelation function $g^{(2)}(5T) = 1.2 \times 10^{-4}$ is slightly higher as compared to the result in Fig. 4.4 ($g^{(2)}(5T) \approx 5.8 \times 10^{-5}$). However, this still suggests strong photon blockade (i.e. $g^{(2)} \sim 10^{-4}$). The trade-off also indicates that the increase in the length of time in which the autocorrelation function stays around its minimum is not unlimited, but rather depends on the threshold value of the autocorrelation function for strong photon blockade.

4.3.4 Optimization for higher single-photon occupation

While it is important to maximize the strength of the photon blockade effect by minimizing the $\tilde{g}^{(2)}$ function, maximizing the single-photon population p_1 at the same time is also important if a single-photon source is targeted. This can be done by minimizing the following target function

$$\eta_2 = \left(1 + w_\mathrm{d}\frac{d}{dt} + w_\mathrm{s}\frac{d^2}{dt^2}\right)\tilde{g}^{(2)}(t_\mathrm{op}) + \frac{w_1}{p_1(t_\mathrm{op})}\,, \tag{4.28}$$

with scalar weight w_1. The target function η_2 in Eq. (4.28) is the target function η_1 in Eq. (4.27) plus a second term that maximizes the single-photon population. Although the multi-photon populations are automatically minimized whenever the single-photon population approaches unity, this is not the case in the perturbative regime of weak driving. Therefore, the autocorrelation function still requires minimization at the same time when the single-photon population is maximized. The target function η_2 also assumes that the single-photon population only varies slowly over the interval in which the autocorrelation function stays near its minimum. This assumption is justified by the weak driving strength.

For better comparison with the results presented in Sec. 4.3.3, it is helpful to assume the system parameters $(\kappa, g_0, t_\mathrm{op}) = (\omega_\mathrm{m}/50, 3\omega_\mathrm{m}/10, 5T)$ and the weights $(w_\mathrm{d}, w_\mathrm{s}) = (1, 10)$. The weight w_1 for the term that is inversely proportional to the single-photon population p_1 is taken to be the value $w_1 = E_1^2/10$ which is proportional to the square strength so that the term becomes unitless to leading order. By minimizing the target function η_2 with respect to the driving strengths (E_1, E_2), the detunings (Δ_1, Δ_2) and the phase ψ, the single-photon occupation at fifth mechanical period increases to $p_1(5T) \approx 9.4 \times 10^{-3}$ as compared to the value $p_1(5T) \approx 6.6 \times 10^{-3}$ in Fig. 4.6. As a trade-off, the value of the autocorrelation function $g^{(2)}(5T)$ also increases from 1.2×10^{-4} to 1.6×10^{-4} but both values are of the same order of magnitude which suggests strong photon blockade. Similarly, the length of time at which the autocorrelation function stays within $\pm 5\%$ of the latter value only slightly reduces to 0.37 mechanical periods from 0.38 mechanical periods. Within this interval, the change in the single-photon population is also less than 5% of its value at the fifth mechanical period, which supports the slow-varying assumption discussed earlier in the section.

The photon population in the cavity is ultimately bounded by the maximal pumping power, and thus the single-photon population can be further enhanced by increasing the driving strength in addition to minimizing the target function Eq. (4.28). For example, with the optimized driving parameters, the single-photon occupation can be enhanced to exceed the vacuum occupation (i.e. $p_1 > 0.5$) if the pumping power is increased by 10-times. However, such modification can lead to a decrease in the accuracy of the perturbative model as is discussed in Sec. 4.4.3.

4.4 Discussion

In this section, I discuss the assumptions made when deriving the main result. For example, the interaction between the mechanical oscillator and the environment can be non-negligible and the perturbative assumptions in the theory fail when the system is driven too strongly. These differences are quantified by numerically computing the autocorrelation function and comparing it with the analytic approximate function $\tilde{g}(t)$ in Eq. (4.23). For consistency and unless otherwise specified, this section adopts the system parameters $(E_1, E_2, g_0, \kappa, t_{\mathrm{op}}) = (\omega_{\mathrm{m}}/200, \omega_{\mathrm{m}}/200, 3\omega_{\mathrm{m}}/10, \omega_{\mathrm{m}}/50, 5T)$ and the driving parameters as used in Fig. 4.6 for which the autocorrelation function reaches the value $g^{(2)}(5T) \approx 1.2 \times 10^{-4}$ at the end of the fifth mechanical period and stays within $\pm 5\%$ of this value for 0.38 mechanical periods. All numerical simulations in Sec. 4.4 are also performed in a larger Hilbert space including up to 10 photons and 25 phonons so that the increasing excitation due to errors can be accurately calculated.

4.4.1 Thermal initial state

Thus far, the mechanical initial state has been assumed to be the ground state. However, undesired thermal excitations in the mechanical oscillator are common in many experiments. It is therefore helpful to study a thermal initial state of the mechanical oscillator, which reads

$$\rho = \frac{1}{1+\bar{n}_{\mathrm{m}}} \sum_{n=0}^{\infty} \left(\frac{\bar{n}_{\mathrm{m}}}{1+\bar{n}_{\mathrm{m}}} \right)^n |n\rangle \langle n| \ , \tag{4.29}$$

with $\bar{n}_{\mathrm{m}}$ being the average phonon number initially in the mechanical mode. Therefore, in this section, the error of the theoretical model is analyzed when the mechanical initial state is cooled to a near-ground state instead of a perfect ground state.

Through numerical simulation, it can be concluded that when the initial state is cooled to a near-ground state with the phonon number below the threshold $\bar{n}_{\mathrm{m}} < 0.1$, the value of the autocorrelation function at the end of the fifth mechanical period remains at a low value $g^{(2)}(5T) < 1.3 \times 10^{-4}$. However, for thermal states with higher phonon population $\bar{n}_{\mathrm{m}} = 10$, the autocorrelation function $g^{(2)}(5T)$ increases by an order of magnitude to 3.7×10^{-3} which suggests a significant decrease in the strength of the photon blockade. This decrease can be explained by the larger uncertainty in the position of the oscillator due to the nature of the thermal state. When this uncertainty becomes comparable to the displacement of the oscillator induced by the optical field, there is a non-vanishing probability for another photon to enter the cavity and thus the strength of the photon blockade effect is diminished.

Although it is not a trivial task to perform a near-ground-state cooling, there are extensive research works [47, 178–180] on this topic with less-than-unity average phonon number $\bar{n}_{\mathrm{m}}$.

4.4.2 Mechanical dissipation

In Sec. 4.3, I assumed that the interactions between the mechanical oscillator and the environment are negligible. In any realistic setting, however, mechanical noise is likely to play an important role. Here, I examine the impact of thermal noise and dissipation on our results. For optomechanical systems with coupling strength g_0 comparable to the mechanical frequency ω_{m}, mechanical dissipation at a rate γ in an environment with mean thermal occupation $\bar{n}_{\mathrm{b}}$ can be modelled by the Lindblad master equation

$$\dot{\rho} = -i[H_{\mathrm{OM}} + H_{\mathrm{d}}, \rho] + \sum_{j=1}^{4} \mathcal{D}_j \rho \,, \tag{4.30}$$

in Eq. (2.30).

To determine the effect of mechanical noise on the photon blockade, I plot the autocorrelation function $g^{(2)}(5T)$ numerically for finite mechanical loss rate γ for different values of the environmental thermal

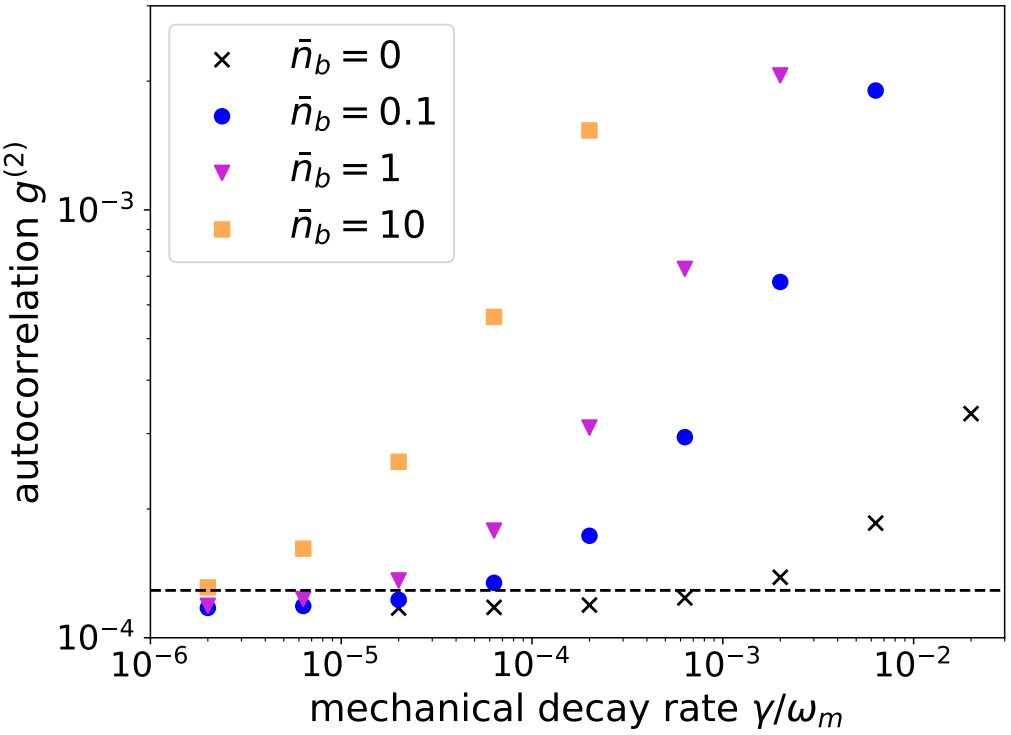


Figure 4.7: The autocorrelation function $g^{(2)}$ as a function of the relative mechanical decay rate $\gamma/\omega_{\rm m}$ for average phonon number in the heat bath being $\bar{n}_{\rm b} = 0$ (cross), $\bar{n}_{\rm b} = 0.1$ (circle), $\bar{n}_{\rm b} = 1$ (triangle), and $\bar{n}_{\rm b} = 10$ (square). The dashed line specifies the value of the autocorrelation function that is 10% larger than the value without the mechanical loss (i.e. $\gamma = 0$). The assumptions of vanishing mechanical decay rate $\gamma \ll \omega_{\rm m}$ and environmental phonon occupation $\bar{n}_b \approx 0$ are required in order to achieve strong photon blockade.

populations (i.e. $\bar{n}_{\rm b} = 0, 0.1, 1, 10$). Figure 4.7 shows the change in the autocorrelation function at the end of the fifth mechanical period as a function of the mechanical decay $\gamma/\omega_{\rm m}$ in units rescaled by the mechanical frequency. The values of γ range from the negligible value $\gamma = 2 \times 10^{-6}\omega_{\rm m}$ to $\gamma = 2 \times 10^{-2}\omega_{\rm m}$ which equals to the optical decay κ.

From Fig. 4.7, I see that a higher dissipation rate γ leads to higher values of autocorrelation $g^{(2)}$, which implies a weaker photon blockade. In a zero-temperature environment (i.e. $\bar{n}_{\rm b} = 0$, indicated by the crosses), the autocorrelation function appears robust to noise (i.e., it stays at the same order of magnitude $g^{(2)} \sim 10^{-4}$) even when γ becomes comparable to the cavity decay $\kappa = 2\times10^{-2}\omega_{\rm m}$. This suggests that, in the zero-temperature environment, the standard of negligible mechanical decay can be met by a variety of experimental setups [29, 171, 181, 182]. On the other hand, for environmental thermal occupation larger than the value $\bar{n}_{\rm b} = 1$, an extremely low mechanical decay rate $\gamma \approx 10^{-6}\omega_{\rm m}$ is required for the autocorrelation function to deviate by less than 10% from its original value. Furthermore, the

autocorrelation function increases by more than one order of magnitude when the mechanical decay rate γ becomes comparable to the optical decay rate κ. Although an autocorrelation of value $\sim 10^{-3}$ does not meet the criterion of strong photon blockade used in this paper, it is still more than one order of magnitude smaller than the best value that can be achieved with a monochromatic driving as in Sec. 4.3.1.

The minimum value of the autocorrelation function $g^{(2)}$ has a super-linear dependence on both the mean phonon occupation $\bar{n}_\mathrm{b}$ in the heat bath and the mechanical decay rate γ. The increasing dependence on the temperature and the coupling rate of the thermal bath is expected because a strongly coupled, hot bath can create excitations in the cavity through optomechanical coupling, which dominates the system dynamics and renders the optimization invalid.

4.4.3 Validity of perturbative methods

The optimization performed on the approximate autocorrelation function $\tilde{g}^{(2)}$ in Eq. (4.23) is only valid as long as the perturbative solutions presented in Sec. 4.2 hold. Their validity is based on the following two assumptions: the driving strength remains small (i.e. $(E/\omega_\mathrm{m})^2 \ll 1$), and the coupling strength remains small (i.e. $(g_0/\omega_\mathrm{m})^4 \ll 1$). Here, I investigate how the accuracy of $\tilde{g}^{(2)}$ changes as these two conditions break down.

The points at which the two perturbative assumptions break down can be found by studying the plot in Fig. 4.8 where the values of the autocorrelation function $g^{(2)}(5T)$ and the approximate autocorrelation function $\tilde{g}^{(2)}(5T)$ are plotted as functions of the driving strength. The coupling strength g_0 is kept fixed throughout[5] The dashed and dotted lines show $\tilde{g}^{(2)}$ when terms up to orders $(g_0/\omega_\mathrm{m})^2$ and $(g_0/\omega_\mathrm{m})^6$ are included, respectively. The circular dots and the crosses show numerical simulations of $g^{(2)}$ and $\tilde{g}^{(2)}$, respectively.

Firstly, it can be observed that the theoretical values for $\tilde{g}^{(2)}(5T)$ (dashed and dotted lines) stay constant

[5]This is because a change in the coupling strength g_0 requires a re-optimization of the driving parameters, and the balance between the strength of the autocorrelation function and the width of the local minimum can be different for each local minimum of the target function η_1. Therefore, instead of varying the coupling strength g_0, the perturbative expansion that assumes a small coupling strength is truncated to a higher order such that only the assumption $(g_0/\omega_\mathrm{m})^{12} \ll 1$ is required to hold.

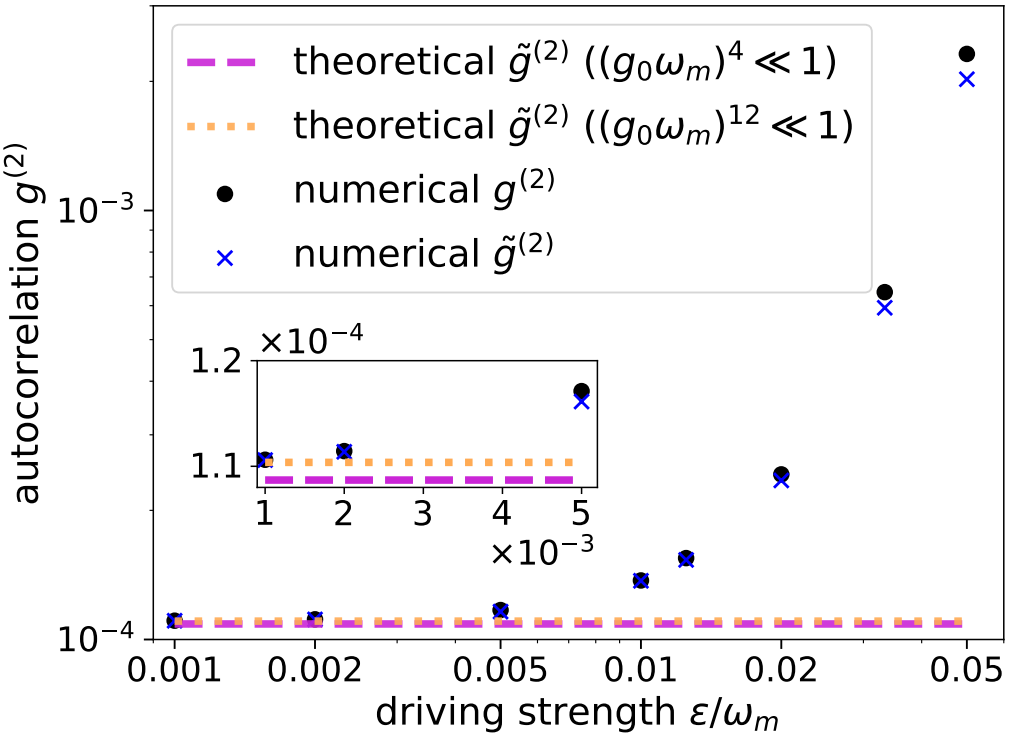


Figure 4.8: The autocorrelation $g^{(2)}$ and $\tilde{g}^{(2)}$ as functions of the driving strength E/ω_m rescaled by the mechanical frequency. The circular data points plot the exact autocorrelation values $g^{(2)}(5T)$ obtained from a full numerical simulation. The cross data points plot the approximate autocorrelation values $\tilde{g}^{(2)}(5T)$ obtained from numerical simulation. The dashed curve plots the case when the perturbative expansion is truncated up to the order $(g_0/\omega_\mathrm{m})^2$ (i.e. $(g_0/\omega_\mathrm{m})^4 \ll 1$). The dotted curve plots the case when the relevant perturbative expansion is truncated to a higher order which imposes a less strict condition (i.e. $(g_0/\omega_\mathrm{m})^8 \ll 1$) on the coupling strength. The inset zooms into the results for small driving strengths. The figure shows that a weak driving strength is necessary for obtaining the results in this paper.

in Fig. 4.8. This can be explained by the following argument. Because the approximate autocorrelation function $\tilde{g}^{(2)}$ omits the contribution from the three and more-photon populations, and because the two-photon population is negligible near its minimum, the function $\tilde{g}^{(2)}$ is approximately proportional to the ratio p_2/p_1^2. According to the series expansion in Eq. (4.13), the single-photon occupation is dominated by the second-order term $\mathcal{S}_1^{(2)}$ which is proportional to E^2. The two-photon occupation is dominated by the fourth-order term $\mathcal{S}_1^{(4)}$, which is proportional to E^4. Thus, to leading order, the approximate autocorrelation function is independent of the driving strength. As a result, the magnitude of E does not influence $g^{(2)}$. In contrast, the three-photon occupation is included in the full numerical calculation of the autocorrelation function $g^{(2)}$, and thus its value changes as a function of the driving strength.

Next, the numerically obtained values for $g^{(2)}$ and $\tilde{g}^{(2)}$ (circles and crosses) can be compared with the

theoretical values (lines). For a very small driving strength $E = \omega_{\mathrm{m}}/1000$ (Fig. 4.8 inset), the majority of the error around the minimum can be attributed to the assumption of small coupling strength (i.e. $(g_0/\omega_{\mathrm{m}})^4 \ll 1$) as there is a wider disagreement between the results when the relevant perturbative expansion is truncated to different orders (dashed and dotted lines) than between the theoretical values and the numerical values (lines and scattered data). However, the overall error of the theoretical model is negligible (< 0.01) even when the terms quartic in the coupling strength are truncated. On the other hand, for stronger driving in Fig. 4.8, the error is dominated by inaccuracy due to the truncated Hilbert space in the theoretical model. Both higher-order correction to the single-photon and two-photon populations (i.e. p_1 and p_2) and the three-photon population can explain the diversion of the exact autocorrelation values (circular dots) from the theoretical values (lines). However, the relatively minor difference between the exact values of the autocorrelation function $g^{(2)}$ and the numerically simulated values of the approximate autocorrelation function $\tilde{g}^{(2)}$ suggests that the higher order corrections to the single- and two-photon populations are responsible for the majority of the error. In the presence of these errors, the optimized driving parameters may not lead to the true minimum of the autocorrelation function, but still, lead to a fast decrease in the value of the autocorrelation function near the specified time $t = 5T$.

Overall, according to Fig. 4.8, it is safe to conclude that the analytic approximations only start breaking down for values larger than $E/\omega_{\mathrm{m}} \approx 0.005$, which is the value used in Sec. 4.3.

4.4.4 System parameters in existing platforms

Since the question of what can be practically achieved with suitably shaped driving depends on the actual system parameters, a brief overview over system parameters that have been realized in existing optomechanical platforms is in order. Table 4.2 shows the relevant parameters from a selection of works, together with the calculated autocorrelation function. The autocorrelation values are computed by minimizing the target function $\tilde{g}^{(2)}(5T)$ at target time $t_{\mathrm{op}} = 5T$ with respect to the driving parameters shown for each case. For each of the examples, two different temperatures (i.e. $\bar{n}_{\mathrm{b}} = 0, 1$) of the thermal bath surrounding the mechanical oscillator are shown.

	g_0/ω_m	κ/ω_m	γ/ω_m	g_0/κ	$g^{(2)}(5T)$ $(\bar{n}_\mathrm{b}=0)$	$g^{(2)}(5T)$ $(\bar{n}_\mathrm{b}=1)$
Nano-acoustic resonator [170]	1.4×10^{-4}	2.3×10^{-1}	4.2×10^{-11}	6.3×10^{-4}	1.0	1.0
Hybrid system (theory) [1]	4.0×10^{-1}	4.6×10^{-2}	1.0×10^{-2}	8.7	1.5×10^{-3}	1.5×10^{-2}
Parameters used in this paper	3.0×10^{-1}	2.0×10^{-2}	0	15	5.8×10^{-5}	5.8×10^{-5}

Table 4.2: System parameters in experiments in comparison with the parameters adopted in this paper and the strength of the resulting photon blockade at the target time $t_\mathrm{op}=5T$. The coupling strength assumed in this paper is too large in comparison with experimental data in the work on nano-acoustic resonators. The parameters in the theoretical work [1] suggest that hybrid systems potentially constitute good platforms for realizing photon blockade.

While it is generally difficult to achieve strong photon blockade, many experimental proposals are moving towards the values assumed in this paper. Most difficulty originates from the requirement of strong coupling strength $g_0 > \kappa$. Especially for solid-state resonators, the best values [168–171] of the coupling strength are still three orders of magnitude smaller than the cavity linewidth. As shown in Table 4.2, the strength of photon blockade is negligible in such a case. However, there are several theoretical proposals [1, 39, 146, 183, 184] for enhancing the optomechanical coupling strength. One approach involves deriving an effective optomechanical Hamiltonian with strong coupling by introducing an additional subsystem. For example, this can be achieved through driving a weakly coupled quadratic optomechanical system using strong coherent light field [146], or by driving a optomechanical system with a χ^2 medium [39]. In particular, in [1], an effective optomechanical Hamiltonian is obtained through plasmon-enhanced Raman scattering in a hybrid metal–dielectric cavity. As listed in Table 4.2, the effective optomechanical coupling strength and the cavity decay rate in such a system are of the same order of magnitude as considered in our work. Thus, the hybrid system could potentially be a good platform to realize the results in Sec. 4.3. Some optomechanical systems with levitated particles [185–188] also have strong values of coupling strength g_0 as compared to the mechanical frequency ω_m. However, in such a system, it is usually true that the inequality $g_0 > \omega_\mathrm{m}$ holds, which is not consistent with the approximations used in the present approach.

4.5 Conclusions and outlook

While it is elusive to realize a strong photon blockade effect without a clear separation of scales, the proposed control scheme demonstrates promising advancements, enhancing the quality of photon blockade even under imperfect conditions. This includes inducing strong photon blockade well before

the steady state is reached ($t_{\mathrm{op}} \ll 1/\kappa$), extending the duration of photon blockade, and maximizing the single-photon occupation.

Further, this control scheme exhibits flexibility, going beyond the mere minimization of the autocorrelation function. It opens up the possibility for optimizing the driving profile in relation to various states. This could include generation of an intermediate state which accelerates the rate of achieving a steady state, or an entangled state that can generate single photons conditioned on specific measurements.

It is important to note that even though the present work does not directly apply to systems with strong coupling strength ($g_0 > \omega_{\mathrm{m}}$), one would expect that suitably designed bichromatic (or polychromatic) driving offers increased capabilities for the preparation of quantum mechanical states also in systems with stronger optomechanical interactions. In particular, strong optomechanical interactions could be used for the preparation of broader classes of quantum states, and the driving techniques developed in this paper can be generalized straightforwardly to any other quantum state with desirable properties. Stronger phonon-photon coupling would certainly make it generally more difficult to identify driving patterns such that the system evolves towards the desired states. However, the potential of the nonclassical quantum states that might be realized in such systems makes such an endeavor a worthwhile goal.

Chapter 5

Output states from optomechanical cavity

The research presented in this chapter was conducted in the concluding phase of my doctoral studies. It is included here to ensure the comprehensiveness of the research undertaken during my PhD program.

5.1 Introduction

In the preceding chapters, optimal driving schemes have been proposed to generate nonclassical states, such as photon Fock states and photon-blockaded states, in optomechanical cavities. These optimized schemes lead to the generation of high-quality intracavity states, aligning with the desired outcomes. Despite these advancements, the discussion so far does not straightforwardly apply to the light fields that are emitted from the cavity. The study of extracavity light field becomes essential when aiming to retrieve the nonclassical states from the optomechanical cavity, or preparing nonclassical states within the cavity that are conditioned on the light measurement result of the extracavity field. In particular, in optomechanical systems, any excitations in the mechanical oscillator lead to a variation in the frequency of the light field stored in the cavity. This variability compromises the suitability of optomechanical systems for light storage when maintaining a constant frequency is essential, necessitating immediate retrieval of the light field after its generation. In light of this issue, the present chapter focuses on the extracavity light field. This investigation builds upon the findings of optomechanical photon blockade as presented in Chap. 4, which already assumes an open cavity configuration.

One possible theoretical framework that allows for the analysis of the output state from the system is through the input-output equation in Eq. (2.34). This model has demonstrated its capability in accurately capturing the physics in several experimental works in optomechanics, such as optomechanically induced transparency [189, 190], quantum metrology [191, 192], and measurement-based state preparation [193, 194]. Despite its success, most existing schemes primarily focus on the so-called linearized regime, where the cavity is dominated by a classical, coherent light field. In this regime, generating photon-blockaded states through classical driving is impossible. Unfortunately, stepping out of this regime also presents challenges as neither analytical nor numerical solutions to the Langevin equation are readily available. It is, therefore, necessary to consider an alternative model that allows for the dynamics of the extracavity light field to be solved.

In this chapter, a cascaded model is adopted to study the output field from the optomechanical cavity. In this model, the output field is assumed to be a single mode quantum harmonic oscillator that exerts negligible back action onto the optomechanical cavity. While this assumption is a coarse approximation of the real-world scenario, one can always choose to study the output state occupying any specific mode in experiments, making the cascaded model relevant. Furthermore, this model is also relevant when one retrieves the cavity state using a one-way waveguide or photon circulator. Therefore, this chapter serves as an elementary study to the output field in optomechanical systems, setting the groundwork for more advanced research in this area.

The chapter is structured into two main sections. First, Sec. 5.2 introduces the general theoretical framework, building upon the foundational works from Sec. 2.5.2. Subsequently, Sec. 5.3 provides a numerical analysis of the output component based on this framework.

5.2 Model

This section discusses a cascaded model made up of two parts: the optomechanical system characterized by annihilation operators a_1 and b, and the output component characterized by the annihilation operator a_2. A schematic plot of the combined system is presented in Fig. 5.1.

For the purpose of this chapter, the output component is considered as a quantum harmonic oscillator

situated within the same heat bath where the optomechanical system under consideration is located. The optomechanical cavity has two pairs of input and output ports. The leaked light from the output port $a_{\mathrm{r,out}}$ at rate κ_{r} is directed into the output component. On the other hand, the driving light field, represented as f_{in}, along with any other forms of dissipation are accommodated by the other input-output port $a_{\mathrm{l,in/out}}$ with dissipation rate κ_{l}. This setup ensures that the reflected driving field, which is generally stronger than the output field from the cavity due to the low cavity dissipation rate, does not overshadow the nonclassical features in the output light field[1]. To capture the light leaked from the optomechanical cavity, the output component has to be partially open. Therefore, the output component also experiences dissipation, represented by the output operator $a_{2,\mathrm{out}}$, at a rate of κ_2.

Given that the two input ports, $a_{\mathrm{l,in}}$ and $a_{\mathrm{r,in}}$, are subject to dissipation rates κ_{l} and κ_{r}, respectively, the overall input operator, $a_{1,\mathrm{in}}$, can then be expressed as

$$a_{1,\mathrm{in}} = \frac{1}{\sqrt{\kappa_1}}\left(\sqrt{\kappa_{\mathrm{l}}}a_{\mathrm{l,in}} + \sqrt{\kappa_{\mathrm{r}}}a_{\mathrm{r,in}}\right) \tag{5.1}$$

where the total dissipation rate κ_1 of the optomechanical cavity is defined by the equation $\kappa_1 = \kappa_{\mathrm{l}} + \kappa_{\mathrm{r}}$.

Assuming the optical heat bath to be a vacuum state and ignoring mechanical dissipation, the master equation of the cascaded system can be derived from Eq. (2.37), and reads as

$$\dot{\rho} = i[\rho, H_{\mathrm{OM}} + H_{\mathrm{out}} + H_{\mathrm{d}}] + \frac{\sqrt{\kappa_2\kappa_{\mathrm{r}}}}{2}([a_1\rho, a_2^\dagger] + [a_2, \rho a_1^\dagger]) + \sum_{j=1,2}\frac{\kappa_j}{2}(2a_j\rho a_j^\dagger - a_j^\dagger a_j\rho - \rho a_j^\dagger a_j)\ , \tag{5.2}$$

where $H_{\mathrm{OM}} = \omega_{\mathrm{c}}a^\dagger a + \omega_{\mathrm{m}}b^\dagger b - g_0 a^\dagger a(b^\dagger + b)$ is the Hamiltonian of the bare optomechanical system, and $H_{\mathrm{out}} = \omega_2 a_2^\dagger a_2$ is the system Hamiltonian of the output component with resonance frequency ω_2. Because the bath degree of freedom is traced out, the driving operator f_{in} has been replaced by adding a semi-classical driving term $H_{\mathrm{d}} = \xi(t)a^\dagger + \xi^*(t)a$ to the system Hamiltonian.

The master equation previously derived serves as a starting point for examining the output light in a specific mode with frequency ω_2. For example, the methodology detailed in Sec. 4.2 could be employed to solve for the autocorrelation $g^{(2)}_{\mathrm{out}}$ and the single photon occupation $\langle a_2^\dagger a_2\rangle$ in the output cavity.

[1] In certain experimental configurations [195–197], it is possible to ensure that the output light remains unaffected by the reflected pump, even though they share the same input-output port. The results presented in this chapter natually accommodates these situations, despite not being explicitly modelled.

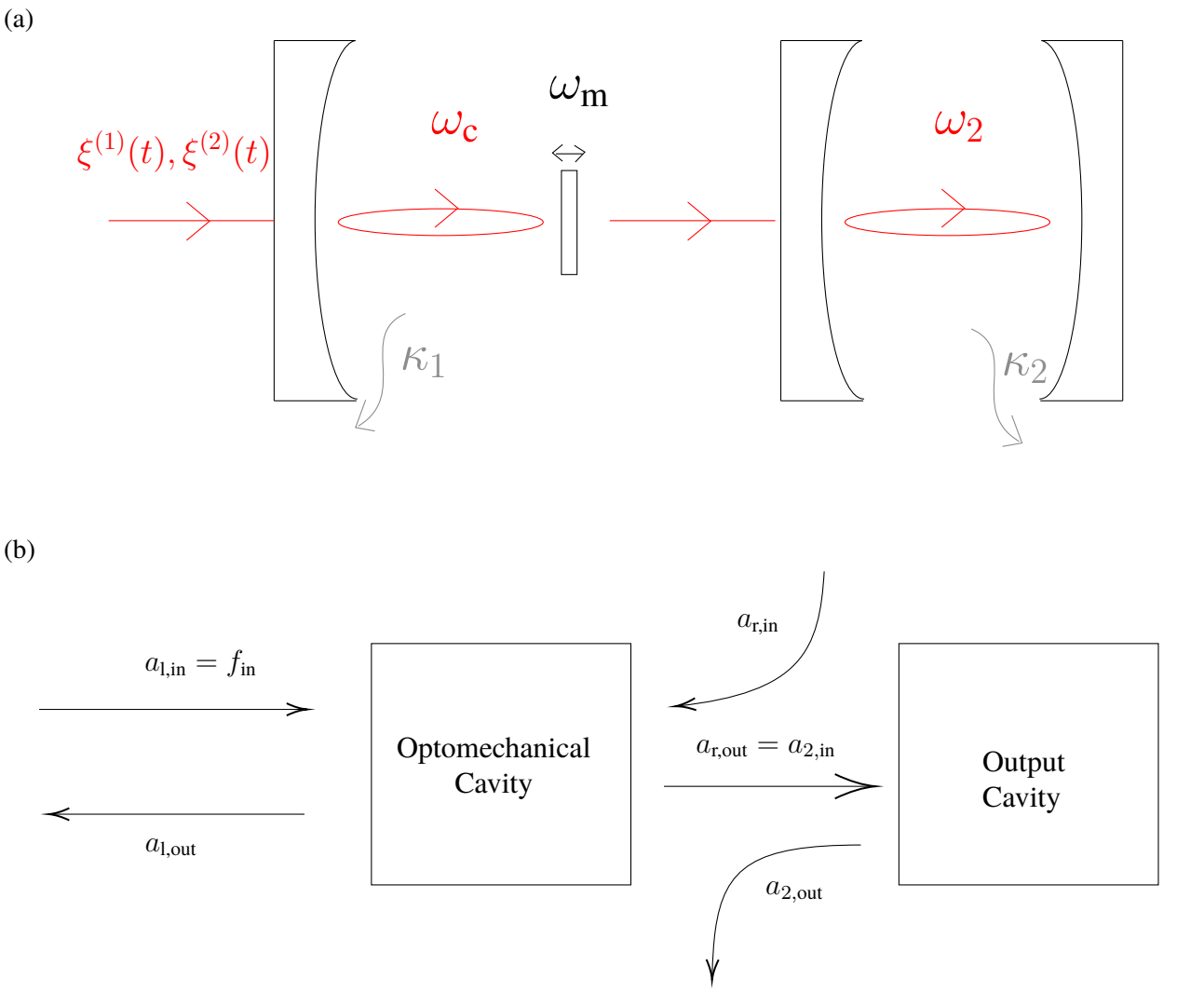


Figure 5.1: Subplot (a) displays a schematic of the cascaded optomechanical system under consideration in this Chapter. This model can serve for analyzing the specific mode output field of the optomechanical cavity. The system comprises an optomechanical setup and a second cavity (output component). The output light from the optomechanical cavity is directed into the output component using a unidirectional waveguide. Subplot (b) display the same physical setup but plotted in a different way to highlight the optical input and output ports. The optomechanical cavity involves two pairs of optical input and output ports ($a_{l,in}$, $a_{l,out}$ and $a_{r,in}$, $a_{r,out}$). The output component has one pair of optical input and output ports ($a_{2,in}$, $a_{2,out}$). The coupling between the optomechanical cavity and the output component is unidirectional, with $a_{r,out} = a_{2,in}$.

However, such reoptimization is not mandatory for accomplishing photon blockade in the output cavity. This is mainly due to the fact that the optomechanical cavity, under photon blockade, functions as an effective photon turnstile over a finite time period. Within this interval, the output cavity experiences dissipation, causing the multi-photon population to decay with time, while the single-photon population retains relatively high levels, owing to the single-photon pumping from the optomechanical cavity. The upcoming section numerically validates this assertion while further exploring the impact

of different system parameters on the output state.

5.3 Numerical results

In this section, the behaviour of the output state under a variety of conditions is examined. This investigation is based on four distinct sets of optomechanical system parameters, denoted by (i)-(iv), along with their respective driving profiles, optimized in a manner identical to the approach detailed in Chap. 4. Among these parameter sets, three correspond to the scenario in which the driving function is determined by minimizing the autocorrelation $\tilde{g}^{(2)}$ at the time point $t_{\rm op} = 5T$. These three parameter sets differ in terms of the optomechanical coupling, with variations as $g_0 =$ (i) $0.28\omega_{\rm m}$, (ii) $0.3\omega_{\rm m}$, (iii) $0.32\omega_{\rm m}$. The fourth parameter set (iv) also has $g_0 = 0.3\omega_{\rm m}$ but with the driving parameters optimized for an extended duration of photon blockade (i.e. same as that detailed in Sec. 4.3.3). This parameter set simultaneously minimizes the autocorrelation and maximizes the duration of photon blockade at the time point $t_{\rm op} = 5T$, when the optomechanical coupling is $g_0 = 0.3\omega_{\rm m}$. In all four parameter sets, the dissipation rates κ_l and κ_r are fixed to be equal to $\kappa_1/2 = \omega_{\rm m}/100$, but all discussions below can straightforwardly be extended to accommodate cases where these rates are unequal. Similar as in Sec. 4.3, the numerical values of the parameters in the driving functions are not specified directly in the subsequent discussion but can be found in Appendix B.3.

Alongside the optomechanical parameters, the resonance frequency ω_2 of the output cavity and the dissipation rate κ_2 can also influence the quantum states in the output cavity. However, the ensuing discussion fixes the resonance frequency ω_2 of the output cavity to be equal to the resonance frequency $\omega_{\rm c}$ of the optomechanical cavity that is the expected frequency of the photons emitted when the optomechanical system remains static. A detailed examination of the impact of the output resonance frequency is left for future studies.

All analysis are grounded on numerical simulations conducted with Qutip [148, 149]. The Hilbert space in these simulations is truncated to include up to 6 photons in each of the optomechanical cavity and the output cavity, and up to 15 phonons unless stated otherwise.

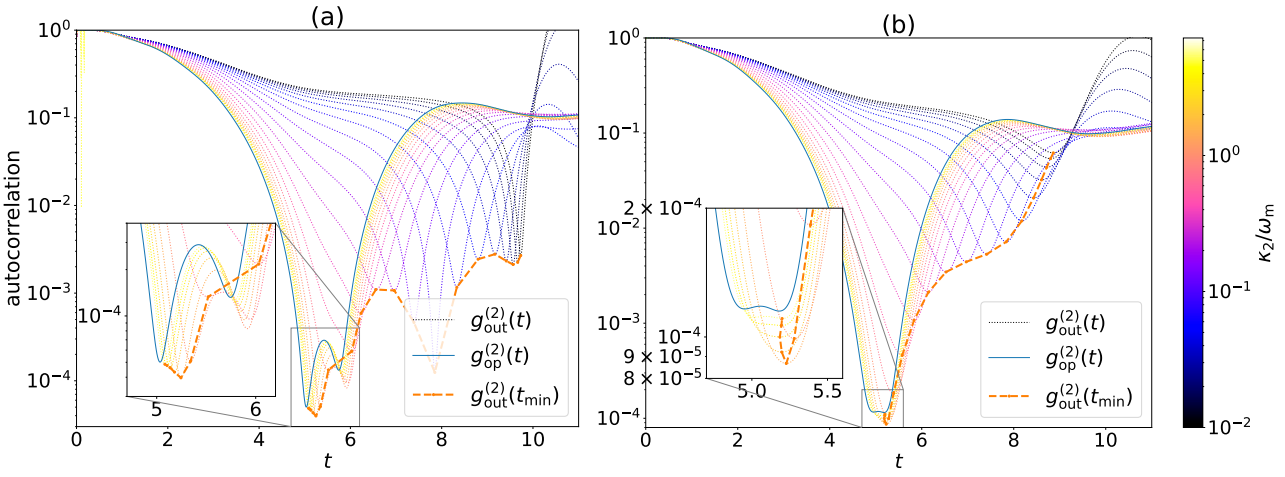


Figure 5.2: Temporal dependence of output autocorrelation, $g^{(2)}_{\text{out}}(t)$, across different output dissipation rates $\kappa_2 \in [10^{-2}/\omega_{\text{m}}, 10/\omega_{\text{m}}]$. The dotted curves represent output autocorrelation values when the optomechanical parameters read $E = \omega_{\text{m}}/200$, $g_0 = 0.3\omega_{\text{m}}$, $\kappa_l = \omega_{\text{m}}/100$, $\kappa_r = \omega_{\text{m}}/100$. Subplot (a) and (b) correspond to simulations under the driving profiles (ii) $g_0 = 0.3\omega_{\text{m}}$ and (iv) $g_0 = 0.3\omega_{\text{m}}$ with broader minimum, respectively. The dashed lines connect minimum output autocorrelation values, $(t_{\text{min}}, g^{(2)}_{\text{out}}(t_{\text{min}}))$. The solid curve presents the optical autocorrelation $g^{(2)}_{\text{op}}(t)$ within the optomechanical cavity, which mirrors the temporal dependence shown in Fig. 4.4(a) and Fig. 4.6 for subplots (a) and (b) respectively.

5.3.1 Autocorrelation against output dissipation rate

This section discusses the dependence of the quantum states within the output cavity on the dissipation rate κ_2 of the output cavity. As an elementary analysis, Fig. 5.2 illustrates the temporal dependence of the output autocorrelation $g^{(2)}_{\text{out}}(t)$ (depicted via dotted curves) across a spectrum of output dissipation rates $\kappa_2 \in [10^{-2}, 10]$. The two subplots are simulation results when the driving profiles (ii) $g_0 = 0.3\omega_{\text{m}}$ and (iv) $g_0 = 0.3\omega_{\text{m}}$ with broader minimum are adopted, respectively.

The minimum values of the output autocorrelation, denoted by $g^{(2)}_{\text{out}}(t_{\text{min}})$ where t_{min} represents the time when the output autocorrelation reaches its minimum, are connected by dashed lines to show the movement of the minimum point $(t_{\text{min}}, g^{(2)}_{\text{out}}(t_{\text{min}}))$ as a function of the output dissipation rate κ_2. The optical autocorrelation $g^{(2)}_{\text{op}}(t)$ within the optomechanical cavity is also plotted alongside. Due to the undirectional nature of the cascaded system (as discussed in Eq. (2.36)), the temporal dependence of the optomechanical autocorrelation mirrors precisely those depicted in Fig. 4.4(a) and Fig. 4.6. Therefore, the autocorrelation within the optomechanical cavity can serve as an insightful comparative benchmark for the output autocorrelation.

As demonstrated by Fig. 5.2, under conditions of high decay rates (i.e. when $\kappa_2 \gg \omega_\mathrm{m}$), the autocorrelation $g^{(2)}_\mathrm{out}$ in the output cavity asymptotically approaches the autocorrelation $g^{(2)}_\mathrm{op}$ in the optomechanical cavity. In this regime, the relaxation time of the output cavity is negligible compared to the timescale of state preparation, ensuring that the output cavity remains in thermal equilibrium with the optomechanical cavity. This observation is in line with the input-output equation in Eq. (2.35), which suggests that in a Markovian (i.e. when $\kappa_2 \to \infty$) thermal heat bath, the autocorrelation of the output field from the optomechanical cavity is exactly the same as that within the optomechanical cavity. This can be substantiated by the following equation

$$g^{(2)} = \frac{\langle a^\dagger_\mathrm{r,out} a^\dagger_\mathrm{r,out} a_\mathrm{r,out} a_\mathrm{r,out}\rangle}{\langle a^\dagger_\mathrm{r,out} a_\mathrm{r,out}\rangle^2} = \frac{\langle a_1^\dagger a_1^\dagger a_1 a_1\rangle}{\langle a_1^\dagger a_1\rangle^2} = g^{(2)}_\mathrm{op} \,, \tag{5.3}$$

where it is assumed that the heat bath is a zero eigenstate of the input operator (i.e. $a_\mathrm{r,in}\rho = 0$).

While the regime of high dissipation rates κ_2 reveals only familiar phenomena which can be interpreted through the input-output equation alone, scenarios involving lower output decay rates have been comparatively less explored in earlier research works. For example, Fig. 5.2 reveals that in the limit of low output dissipation rates (i.e. when $\kappa_2 \ll \omega_\mathrm{m}$), both the minimum value of the autocorrelation $g^{(2)}_\mathrm{out}$ and the time t_min at which this minimum is reached increase as the decay rate decreases. The increase in the time t_min can be attributed to the stronger retardation effect resulting from longer memory of the output cavity. During the initial phase of dynamics (i.e. $t < t_\mathrm{min}$), the photon blockade effect in the optomechanical cavity is less pronounced (i.e. $g^{(2)}_\mathrm{out}(t) \gg g^{(2)}_\mathrm{out}(t_\mathrm{min})$), so the state transferred to the output cavity has a non-negligible multi-photon population. Despite the state becoming highly photon-blockaded thereafter, the multi-photon population requires an extended time to completely dissipate in the output cavity via decay. Moreover, as the strength of photon blockade diminishes in the optomechanical cavity after $t \approx 5T$, the multi-photon population transferred to the output cavity increases again prior to reaching a value equal to the minimum observed in the optomechanical cavity. Consequently, the minimum value of output autocorrelation also increases with decreasing output cavity decay.

While there is a general trend indicating that the autocorrelation $g^{(2)}_\mathrm{out}(t_\mathrm{min})$ and the corresponding time t_min increase with the output cavity decay rate κ_2, this trend is not absolute and there are observable

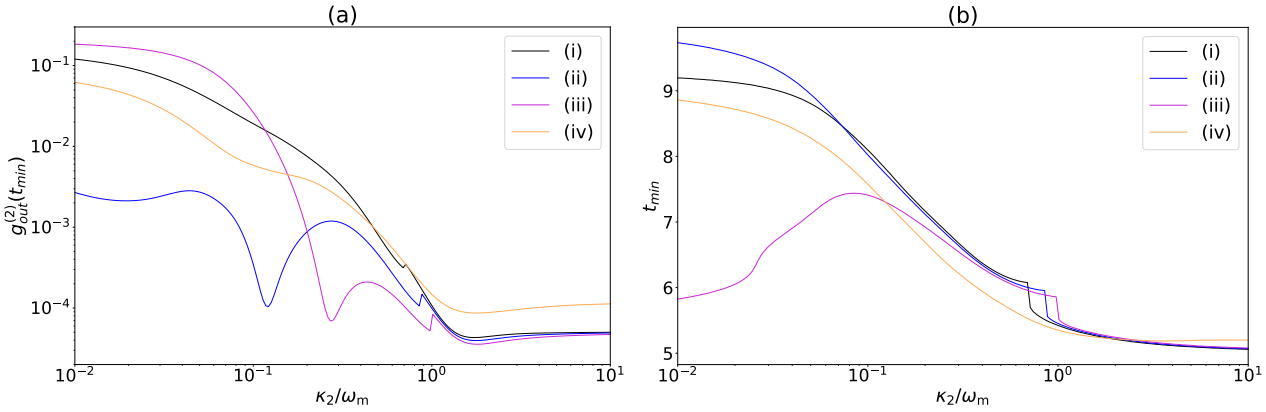


Figure 5.3: Plots of (a) the minimum autocorrelation $g^{(2)}_{\text{out}}(t_{\text{min}})$ in the output cavity; (b) the time t_{min} at which the output autocorrelation achieves its minimum, each as a function of the output cavity decay rate κ_2. The four distinct curves in each subplot correspond to instances where: (i) $g_0 = 0.28\omega_{\text{m}}$, (ii) $g_0 = 0.3\omega_{\text{m}}$, (iii) $g_0 = 0.32\omega_{\text{m}}$, and (iv) $g_0 = 0.3\omega_{\text{m}}$ with the driving parameters optimized for an extended duration of photon blockade. The remaining optomechanical parameters are set as $(E, \kappa_l, \kappa_r) = (\omega_{\text{m}}/200, \omega_{\text{m}}/100, \omega_{\text{m}}/100)$. The optimized driving profiles can be found in Appendix B.3.

local deviations. These local deviations manifest across various instances, potentially affecting either some parameter sets or encompassing all sets. To compare the dependence of the minimum of the output autocorrelation on the output decay rate κ_2 under various parameter sets, Fig. 5.3 plots the minima values of the autocorrelation $g^{(2)}_{\text{out}}(t_{\text{min}})$ and the corresponding time points t_{min} as functions of the output decay rate κ_2 for all four parameter sets (i)-(iv). This comparison aims to highlight the similarities and differences between these relationships under different parameter sets.

Figure 5.3(a) reveals how the minimal value of the output autocorrelation $g^{(2)}_{\text{out}}(t_{\text{min}})$ varies. Starting from high output decay rates (i.e. $\kappa_2 = 10\omega_{\text{m}}$), the minimum autocorrelation initially decrease as the output decay rate decreases for all four sets of parameters, which contrasts with the general rule that autocorrelation increases as decay rate decreases for low output dissipation rate κ_2. In this regime (i.e. when $\kappa_2 < 10\omega_{\text{m}}$), the photon lifetime in the output cavity in non-negligible compared to the numerical precision adopted in this work, such that the output cavity does not instantly reach equilibrium with the optomechanical cavity. Due to this delay in equilibration, the light field in the output cavity and the emitted light from the optomechanical cavity can interfere in a non-trivial way, such that the single-photon population increases while the multi-photon population decreases (for more details, see Appendix A). Furthermore, in contrast to the case of bidirectional coupling where the back action of the output cavity on the optomechanical cavity accelerates equilibration, the deviation of the

output autocorrelation from that in the optomechanical cavity can potentially be more significant in the cascaded system. Nonetheless, the effect is weak compared to the existing photon blockade effect resulting from the bichromatic driving, such that the additional decrease in autocorrelation is minor compared to the minimum autocorrelation $g^{(2)}_{\text{op}}(t_{\text{min}}) \sim 10^{-4}$ in the optomechanical cavity according to Fig. 5.3(a). As the output decay rate κ_2 further decreases, the memory effect of the cavity becomes prominent, such that the destructive interference between the two light fields becomes overshadowed by the increase in the multi-photon population in the output cavity. The autocorrelation then increases as the dissipation rate κ_2 decreases.

In addition to the initial decrease in the autocorrelation, there are sharp decreases in the minimum autocorrelation $g^{(2)}_{\text{out}}(t_{\text{min}})$ when the output decay rate reaches the value $\kappa \approx \omega_{\text{m}}$ for three of the parameter sets (i.e. curves (i) - (iii) in Fig. 5.3). This is because the autocorrelation $g^{(2)}_{\text{op}}(t)$ in the optomechanical cavity has two local minima in the vicinity of $t = 5$ for these parameters. The same effect can also be observed in Fig. 5.2(a) inset.

Figure 5.3(b) also reveals decreases in the minimum value of the autocorrelation function $g^{(2)}_{\text{out}}(t_{\text{min}})$ as κ_2 decreases in the vicinity of $\kappa_2 \approx 0.1$ for the parameter set (ii) and $\kappa_2 \approx 0.3$ for the set (iii) (also see Fig. 5.2(a), around $t_{\text{min}} \approx 8T$). Furthermore, in the limit of low output decay rate $\kappa_2 \sim 10^{-2}$, the photon blockade effect becomes weak (i.e. $g^{(2)}_{\text{out}}(t_{\text{min}}) \sim 10^{-1}$) for three parameter sets but not for the parameter set (i) , where the autocorrelation functions still attains a value $\sim 10^{-3}$. These phenomena suggest that for some parameter sets, strong photon blockade effect can be induced in the output cavity even when the output cavity has a low decay rate. Especially, the robust photon blockade effect in the output cavity for parameter set (i) (i.e. $g_0 = 0.28\omega_{\text{m}}$) indicates potential advantages in the cascaded setup when the photon-blockaded state needs to be transferred to a second cavity or other optical components. While the precise mechanism that drives this unusual decrease in autocorrelation as output dissipation decreases is not straightforward to explain within the scope of the theoretical tools employed in this thesis, the subject undoubtedly merits more detailed theoretical exploration in future works.

Figure 5.3(b) illustrates how the time t_{min} at which minimum autocorrelation occurs depends on the output decay rate κ_2. Analogous to Fig. 5.3(a), abrupt jumps appear at $\kappa \approx \omega_{\text{m}}$ in the plots due to the

merging of local minima of the autocorrelation $g^{(2)}_{\text{out}}(t)$. There is also slight decrease in the time t_{min} as dissipation rate κ_2 decreases at large values of κ_2 for parameter set (iv) (i.e. $g_0 = 0.3\omega_{\text{m}}$ broader minimum). The decrease is also due to a merge of local minima as can be observed in Fig. 5.2(b) inset.

Aside from the merging of local minima, the time t_{min} monotonically increases as the decay rate κ_2 decreases for three sets of parameters, except for set (iii) (i.e. $g_0 = 0.32\omega_{\text{m}}$). The reduction of the time t_{min} for the parameter set with optomechanical coupling rate $g_0 = 0.32\omega_{\text{m}}$ can be attributed to high minimum autocorrelation values (i.e., $g^{(2)}_{\text{out}}(t_{\text{min}}) > 0.1$). In this regime, the sudden decrease in the autocorrelation $g^{(2)}_{\text{op}}(t)$ of the optomechanical cavity around $t = 5T$ no longer contributes significantly to the dynamics of the output cavity due to its relatively short duration compared to the lifetime of the photons inside the output cavity (i.e. $t \ll 1/\kappa_2$). Nonetheless, a mild photon blockade effect can still be observed because the bare optomechanical system coupling can still facilitate photon blockade, even without the destructive interference between the two driving components (i.e. conventional photon blockade). This is further substantiated by the similar values between optomechanical autocorrelation $g^{(2)}_{\text{op}}(5T) \approx 0.09$ under a monochromatic drive and the output autocorrelation $g^{(2)}_{\text{out}}(t_{\text{min}}) \approx 0.1$ when t_{min} begins to fall as the dissipation rate κ_2 decreases in Fig. 5.3(b).

5.3.2 Single-photon population against output dissipation rate

In addition to the strength of photon blockade, the single-photon population $p_{1,\text{out}}(t_{\text{min}})$ in the output component at the point of maximum photon blockade is also an important factor. In the rest of the section, the dependence of the single-photon population $p_{1,\text{out}}$ on the output linewidth κ_2 is examined through analysis of Fig. 5.4. Considering that the single-photon population $p_{1,\text{op}}$ varies in the optomechanical cavity depending on the parameters used, the ratio of the single-photon populations $p_{1,\text{out}}$ to $p_{1,\text{op}}$ is plotted instead of the bare single-photon population.

Figure Fig. 5.4(a) plots the temporal variation of the single-photon ratio for parameter set (ii) which is also used in Fig. 5.2(a). The plot demonstrates that, due to the low coupling rate $\sqrt{\kappa_2\kappa_r}$ between the optomechanical and output cavities, the single-photon population in the output component is invariably lower than in the optomechanical cavity in the first ten mechanical periods.

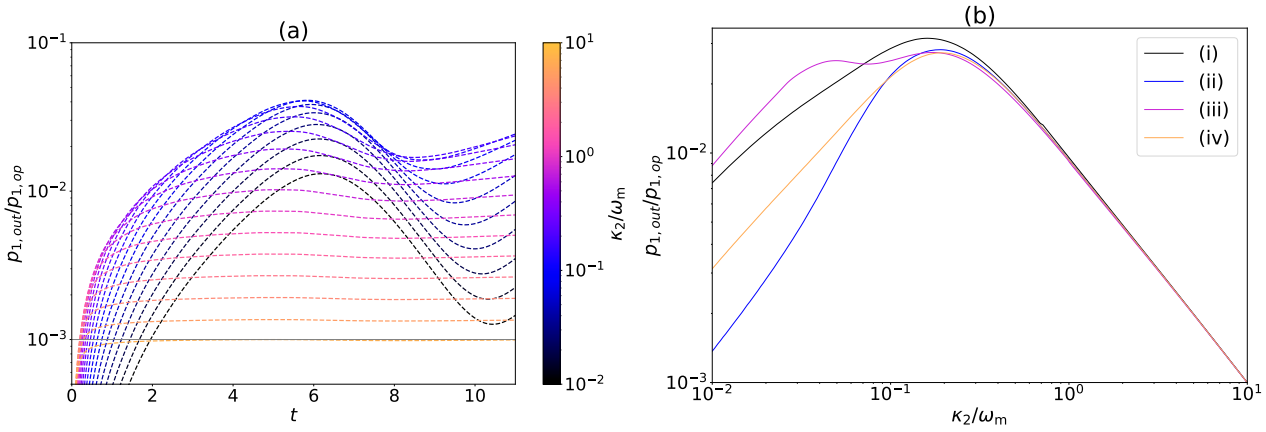


Figure 5.4: Ratio of the single-photon population $p_{1,\text{out}}/p_{1,\text{op}}$ (a) as a function of evolution time for a range of different output dissipation rate ($\kappa_2 \in [0.01, 10]$) for the parameter set ((ii)) (i.e. same as in Fig. 5.2(a)), (b) at the time point when the photon blockade effect is the strongest for the output component and the optomechanical cavity respectively (y-axis) against the output decay rate (x-axis), where: (i) $g_0 = 0.28\omega_\text{m}$, (ii) $g_0 = 0.3\omega_\text{m}$, (iii) $g_0 = 0.32\omega_\text{m}$, and (iv) $g_0 = 0.3\omega_\text{m}$ with the driving parameters optimized for an extended duration of photon blockade.

When there is a high output dissipation rate ($\kappa_2 \sim 10\omega_\text{m}$), the short photon lifetime ($1/\kappa_2 \ll t_\text{min}$) is the key constraint limiting the photon population within the output cavity. In this regime, the ratio of single-photon population quickly achieves equilibrium, whereby the photon population within the output cavity can be approximated by the squared ratio of the photon pumping and dissipation rates in the output cavity. This can be expressed as $\langle n\rangle_\text{out} = (\sqrt{\kappa_r\kappa_2\langle n\rangle_\text{op}})^2/\kappa_2^2$, assuming the number of photons $\langle n\rangle_\text{op}$ in the optomechanical cavity remains steady over a timescale of $1/\kappa_2$. The plot exhibits strong correlation between this estimation and the simulation result when $\kappa_2 = 10\omega_\text{m}$ (i.e. $\langle n\rangle_\text{out}/\langle n\rangle_\text{op} \approx 10^{-3}$).

As the photon lifetime in the output cavity increases, the photon population within the optomechanical cavity can no longer be considered constant, possibly leading to destructive interference within the output cavity. For instance, after a time period of $t = 6T$, Fig. 5.4(a) reveals a reduction in the single-photon population within the output cavity. This decrease is more pronounced for lower cavity dissipation rates κ_2, thereby inhibiting the accumulation of high single-photon population in the output cavity. Consequently, the ideal cavity dissipation rate for the parameter set is identified to be $\kappa_2 \approx 10^{-2}\omega_\text{m}$ for any evolution time in the range $t \in (6T, 10T)$.

Figure Fig. 5.4(b) plots the dependency of the single-photon ratio on the output dissipation rate at time point t_min, where the output autocorrelation reaches its minimum value. As in Fig. 5.4(a), the

single-photon ratios for all four parameter sets attain their respective local maxima around the point when $\kappa_2 \approx 10^{-1}\omega_{\mathrm{m}}$, indicating the presence of similar destructive interference in each case. There is an additional local minimum for parameter set (iii) , but this is attributed to the high autocorrelation as discussed in Fig. 5.3(b). In this regime, as t_{min} moves earlier from $t_{\mathrm{min}} \approx 7T$, the single-photon ratio drifts away from the local minimum, as seen in Fig. 5.4(a), which consequently results in a slight increase in its value.

5.4 Conclusions

In this chapter, I build upon the prior chapters and further extend the existing frameworks to include the dynamics of the emitted light field, particularly when the output field is channeled into an external cavity. A regime has been identified where, owing to destructive interference within the output cavity, the autocorrelation of the emitted field remains suppressed without introducing additional complication to the driving profile. Interestingly, while many instances demand the output cavity to exhibit high transmittance, specific driving profiles can induce pronounced photon blockades even in less transmissive setups.

It is noteworthy that, while this chapter focuses on scenarios where only the output light from a single optomechanical system interfaces with the output cavity, the study can be straightforwardly extended to incorporate additional driving in the output cavity. Benefiting from the inherent one-way dynamics of the model, it becomes possible to solve the dynamics of the feeder systems as independent problems, facilitating the synthesis of resultant states in the output cavity without disrupting individual system dynamics. This attribute presents promising avenues for enhancing state preparation quality and broadening the range of attainable states.

While the approach in this chapter predominantly utilizes numerical tools, the underlying theoretical framework permits an analytical solution to the dynamics of the output field using the same methodology as in Chap. 4. Moreover, due to the one-way nature of the model, the study of the output dynamics is largely simplified when the dynamics of the optomechanical system are already known. This paves the way for a more insightful interpretation of output dynamics if the internal system dynamics can be

recast into a form that is more physically intuitive, although this is currently hindered by the approximation in Eq. (4.24).

Chapter 6

Conclusion

6.1 Thesis achievements and limitations

This thesis illustrates the successful application of quantum control in generating highly nonclassical light within optomechanical systems. Our exploration is segmented into three integral yet distinct aspects.

In Chap. 3, I design driving protocols based on the perturbative solution of closed system dynamics. This method paves the way towards the deterministic generation of high-fidelity optical states through driven optomechanical systems. It is also noteworthy that although only a select set of target states have been presented using a bichromatic setup, the method can potentially be extended to other setups, thus expanding the spectrum of attainable states. Notably, our driving scheme demonstrates resilience even under minor perturbations by the thermal bath, which attests to its practical viability in upcoming applications. Apart from the advantages, the proposed methodology makes several assumptions that can lead to potential limitations. One assumption is that the phase and amplitude modulation of the driving fields can be performed instantly. Both earlier work [198] and standard experimental parameters ($\sim$ GHz) suggest that such modulation can be immaterial compared to the typical mechanical frequency ($\sim$ MHz), but such separation in the scale may not hold in all optomechanical experiments. One other assumption is that the driving can be pumped into a cavity with arbitrarily long photon lifetime. While this assumption can in general be more difficult to fulfill, Chap. 4 addresses this problem

by explicitly including a non-negligible cavity dissipation into the model.

In Chap. 4, the system dynamics of a driven-dissipative optomechanical system is solved perturbatively where the driving strength is weak. By focusing on short-time system dynamics, I design a driving profile that induces a strong photon blockade, remarkably quicker than existing steady-state procedures. This work further underscores the potential of an optimized driving profile in the generation of nonclassical light. Also, although the requisite system parameters currently surpass the capabilities of existing experiments, I identify promising evidence suggesting feasible advancements in future experimental setups. However, the proposed methodology also suffers from its limitations. First, the current series expansion leads to an expression that lacks explanation. This can compromise the design of more complicated driving protocols such as the ones in Chap. 3. Secondly, the system dynamics is solved in the weak-driving regime, which, together with non-vanishing cavity dissipation, ultimately limits the number of photons inside the cavity. However, this problem can potentially be reconciled by moving into a perturbative regime with weak coupling but strong driving. Finally, the research is restricted to intracavity light fields, but the extraction of the generated states also worths discussion.

In Chap. 5, the interaction between the optomechanical system and the environmental degree of freedom is further exploited to include the dynamics of an output mode. Our findings suggest that the strong photon blockade effect can be transferred to the output component for sufficiently large system dissipation of the output component. This chapter serves as a complement to the earlier study in Chap. 4, and opens up the possibility for broader applications.

In essence, this research endeavors to overcome the inherent challenges optomechanical systems present in the creation of nonclassical light states. By drawing inspiration from works by the pioneers in the field and developing new methods, I aspire to spark further innovation in the domain. Given the consistent advancements in optomechanical systems research, the realization of the proposed control techniques in experiments remains a tangible future prospect.

6.2 Future work

The insights derived from this thesis encompass a broad spectrum of optomechanical systems, opening doors to several promising research trajectories. Below are potential directions that warrant further investigation:

- By incorporating higher order terms into the Magnus expansion, challenges detailed in Sec. 3.4 can be addressed. This would allow for a stronger coupling strength and shorter dynamics in state preparation such as outlined in Chap. 3.
- Even though optomechanical systems can operate under cryogenic conditions, there are advantages in conducting experiments at higher temperatures. Extending the theoretical frameworks presented in this thesis to analytically include mechanical thermalization would thus be a valuable addition.
- An analytical solution or more intuitive representation of the double exponential function Eq. (4.24) would enhance the interpretability of findings in Chap. 4. Therefore, an alternative solution might provide deeper insights into the fast photon blockade effect.
- The discussions on output dynamics in Chap. 5 can be broadened to incorporate additional elements. For instance, introducing external driving to the output or channeling the output from multiple optomechanical cavities to the output components might unveil a wider range of optomechanical system applications.

Bibliography

[1] Mohsen Kamandar Dezfouli, Reuven Gordon, and Stephen Hughes. Molecular optomechanics in the anharmonic cavity-QED regime using hybrid metal–dielectric cavity modes. *ACS Photonics*, 6(6):1400–1408, May 2019.

[2] Li-Yun Hu, Chao-Ping Wei, Jie-Hui Huang, and Cun-Jin Liu. Quantum metrology with fock and even coherent states: Parity detection approaches to the heisenberg limit. *Opt. Commun.*, 323:68–76, July 2014.

[3] Sean D. Huver, Christoph F. Wildfeuer, and Jonathan P. Dowling. Entangled fock states for robust quantum optical metrology, imaging, and sensing. *Phys. Rev. A*, 78(6):063828, December 2008.

[4] Rafal Demkowicz-Dobrzański, Marcin Jarzyna, and Jan Kołodyński. Quantum limits in optical interferometry. In *Progress in Optics*, pages 345–435. Elsevier, 2015.

[5] Nicolas Gisin, Grégoire Ribordy, Wolfgang Tittel, and Hugo Zbinden. Quantum cryptography. *Rev. Mod. Phys.*, 74(1):145–195, March 2002.

[6] Zhen-Qiang Yin, Hong-Wei Li, Wei Chen, Zheng-Fu Han, and Guang-Can Guo. Security of counterfactual quantum cryptography. *Phys. Rev. A*, 82(4):042335, October 2010.

[7] Mathieu Bozzio, Michal Vyvlecka, Michael Cosacchi, Cornelius Nawrath, Tim Seidelmann, Juan C Loredo, Simone L Portalupi, Vollrath M Axt, Peter Michler, and Philip Walther. Enhancing quantum cryptography with quantum dot single-photon sources. *Npj Quantum Inf.*, 8(1), September 2022.

[8] A Mari and J Eisert. Positive wigner functions render classical simulation of quantum computation efficient. *Phys. Rev. Lett.*, 109(23):230503, December 2012.

[9] Victor Veitch, Nathan Wiebe, Christopher Ferrie, and Joseph Emerson. Efficient simulation scheme for a class of quantum optics experiments with non-negative wigner representation. *New J. Phys.*, 15(1):013037, January 2013.

[10] John F Clauser. Experimental distinction between the quantum and classical field-theoretic predictions for the photoelectric effect. *Phys. Rev. D Part. Fields*, 9(4):853–860, February 1974.

[11] Hiroki Takesue and Kyo Inoue. Generation of polarization-entangled photon pairs and violation of bell's inequality using spontaneous four-wave mixing in a fiber loop. *Phys. Rev. A*, 70(3), September 2004.

[12] B R Gadway, E J Galvez, and F De Zela. Bell-inequality violations with single photons entangled in momentum and polarization. *J. Phys. B At. Mol. Opt. Phys.*, 42(1):015503, January 2009.

[13] Adam Vallés, Vincenzo D'Ambrosio, Martin Hendrych, Michal Mičuda, Lorenzo Marrucci, Fabio Sciarrino, and Juan P Torres. Generation of tunable entanglement and violation of a bell-like inequality between different degrees of freedom of a single photon. *Phys. Rev. A*, 90(5), November 2014.

[14] S Magnitskiy, D Frolovtsev, V Firsov, P Gostev, I Protsenko, and M Saygin. A SPDC-based source of entangled photons and its characterization. *J. Russ. Laser Res.*, 36(6):618–629, November 2015.

[15] M Brune, S Haroche, V Lefevre, V, J M Raimond, and N Zagury. Quantum nondemolition measurement of small photon numbers by rydberg-atom phase-sensitive detection. *Phys. Rev. Lett.*, 65, aug 1990.

[16] B T Varcoe, S Brattke, M Weidinger, and H Walther. Preparing pure photon number states of the radiation field. *Nature*, 403(6771):743–746, February 2000.

[17] X Zhou, I Dotsenko, B Peaudecerf, T Rybarczyk, C Sayrin, S Gleyzes, J M Raimond, M Brune, and S Haroche. Field locked to a fock state by quantum feedback with single photon corrections. *Phys. Rev. Lett.*, 108(24):243602, June 2012.

[18] Serge Haroche. Nobel lecture: Controlling photons in a box and exploring the quantum to classical boundary. *Rev. Mod. Phys.*, 85(3):1083–1102, July 2013.

[19] Igor Aharonovich, Dirk Englund, and Milos Toth. Solid-state single-photon emitters. *Nat. Photonics*, 10(10):631–641, September 2016.

[20] Peter Lodahl, Arne Ludwig, and Richard J. Warburton. A deterministic source of single photons. *Phys. Today*, 75(3):44–50, March 2022.

[21] Xiaoyan Zhou, Liang Zhai, and Jin Liu. Epitaxial quantum dots: a semiconductor launchpad for photonic quantum technologies. *Photonics Insights*, 1(2):R07, 2022.

[22] Shuai Shi, Biao Xu, Kuan Zhang, Gen-Sheng Ye, De-Sheng Xiang, Yubao Liu, Jingzhi Wang, Daiqin Su, and Lin Li. High-fidelity photonic quantum logic gate based on near-optimal rydberg single-photon source. *Nat. Commun.*, 13(1):4454, August 2022.

[23] H Wang, M Hofheinz, M Ansmann, R C Bialczak, E Lucero, M Neeley, A D O'Connell, D Sank, J Wenner, A N Cleland, and John M Martinis. Measurement of the decay of fock states in a superconducting quantum circuit. *Phys. Rev. Lett.*, 101(24):240401, December 2008.

[24] V S C Canela and H J Carmichael. Bright sub-poissonian light through intrinsic feedback and external control. *Phys. Rev. Lett.*, 124(6):063604, February 2020.

[25] M Uria, P Solano, and C Hermann-Avigliano. Deterministic generation of large fock states. *Phys. Rev. Lett.*, 125(9), August 2020.

[26] Mohammad Mirhosseini, Alp Sipahigil, Mahmoud Kalaee, and Oskar Painter. Superconducting qubit to optical photon transduction. *Nature*, 588(7839):599–603, December 2020.

[27] Rishabh Sahu, William Hease, Alfredo Rueda, Georg Arnold, Liu Qiu, and Johannes M Fink. Quantum-enabled operation of a microwave-optical interface. *Nat. Commun.*, 13(1):1276, March 2022.

[28] Hai-Tao Tu, Kai-Yu Liao, Zuan-Xian Zhang, Xiao-Hong Liu, Shun-Yuan Zheng, Shu-Zhe Yang, Xin-Ding Zhang, Hui Yan, and Shi-Liang Zhu. High-efficiency coherent microwave-to-optics conversion via off-resonant scattering. *Nat. Photonics*, 16(4):291–296, April 2022.

[29] Markus Aspelmeyer, Tobias J. Kippenberg, and Florian Marquardt. Cavity optomechanics. *Rev. Mod. Phys.*, 86(4):1391–1452, December 2014.

[30] Daniel W. C. Brooks, Thierry Botter, Sydney Schreppler, Thomas P. Purdy, Nathan Brahms, and Dan M. Stamper-Kurn. Non-classical light generated by quantum-noise-driven cavity optomechanics. *Nature*, 488(7412):476–480, August 2012.

[31] S. Bose, K. Jacobs, and P. L. Knight. Preparation of nonclassical states in cavities with a moving mirror. *Phys. Rev. A*, 56(5):4175–4186, November 1997.

[32] P. Rabl. Photon blockade effect in optomechanical systems. *Phys. Rev. Lett.*, 107(6):063601, August 2011.

[33] Z R Gong, H Ian, Yu-Xi Liu, C P Sun, and Franco Nori. Effective hamiltonian approach to the kerr nonlinearity in an optomechanical system. *Phys. Rev. A*, 80(6), December 2009.

[34] Samuel Aldana, Christoph Bruder, and Andreas Nunnenkamp. Equivalence between an optomechanical system and a kerr medium. *Phys. Rev. A*, 88(4), October 2013.

[35] Victor Fiore, Yong Yang, Mark C Kuzyk, Russell Barbour, Lin Tian, and Hailin Wang. Storing optical information as a mechanical excitation in a silica optomechanical resonator. *Phys. Rev. Lett.*, 107(13):133601, September 2011.

[36] Pardeep Kumar and M Bhattacharya. Single-photon transfer using levitated cavityless optomechanics. *Phys. Rev. A (Coll. Park.)*, 99(2), February 2019.

[37] David P Lake, Matthew Mitchell, Denis D Sukachev, and Paul E Barclay. Processing light with an optically tunable mechanical memory. *Nat. Commun.*, 12(1):663, January 2021.

[38] Bijita Sarma and Amarendra K Sarma. Single-photon blockade in a hybrid cavity-optomechanical system via third-order nonlinearity. *J. Phys. B At. Mol. Opt. Phys.*, 51(7):075505, April 2018.

[39] Dong-Yang Wang, Cheng-Hua Bai, Xue Han, Shutian Liu, Shou Zhang, and Hong-Fu Wang. Enhanced photon blockade in an optomechanical system with parametric amplification. *Opt. Lett.*, 45(9):2604–2607, May 2020.

[40] A. A. Clerk, M. H. Devoret, S. M. Girvin, Florian Marquardt, and R. J. Schoelkopf. Introduction to quantum noise, measurement, and amplification. *Rev. Mod. Phys.*, 82(2):1155–1208, April 2010.

[41] Aashish A. Clerk. Optomechanics and Quantum Measurement. In *Quantum Optomechanics and Nanomechanics: Lecture Notes of the Les Houches Summer School: Volume 105, August 2015*. Oxford University Press, 03 2020.

[42] A. Nunnenkamp, K. Børkje, and S. M. Girvin. Single-photon optomechanics. *Phys. Rev. Lett.*, 107(6), August 2011.

[43] P Rabl. Photon blockade effect in optomechanical systems. *Phys. Rev. Lett.*, 107(6):063601, August 2011.

[44] P Forn-Díaz, L Lamata, E Rico, J Kono, and E Solano. Ultrastrong coupling regimes of light-matter interaction. *Rev. Mod. Phys.*, 91(2):025005, June 2019.

[45] Jiaojiao Chen, Zhuanxia Li, Xiao-Qing Luo, Wei Xiong, Mingfeng Wang, and Hai-Chao Li. Strong single-photon optomechanical coupling in a hybrid quantum system. *Opt. Express*, 29(20):32639, September 2021.

[46] N Carlon Zambon, Z Denis, R De Oliveira, S Ravets, C Ciuti, I Favero, and J Bloch. Enhanced cavity optomechanics with quantum-well exciton polaritons. *Phys. Rev. Lett.*, 129(9):093603, August 2022.

[47] B M Brubaker, J M Kindem, M D Urmey, S Mittal, R D Delaney, P S Burns, M R Vissers, K W Lehnert, and C A Regal. Optomechanical ground-state cooling in a continuous and efficient electro-optic transducer. *Phys. Rev. X.*, 12(2), June 2022.

[48] Yu-Hong Liu, Xian-Li Yin, Jin-Feng Huang, and Jie-Qiao Liao. Accelerated ground-state cooling of an optomechanical resonator via shortcuts to adiabaticity. *Phys. Rev. A (Coll. Park.)*, 105(2), February 2022.

[49] E. Wigner. On the quantum correction for thermodynamic equilibrium. *Phys. Rev.*, 40(5):749–759, June 1932.

[50] A. Holevo. Some statistical problems for quantum gaussian states. *IEEE Trans. Inf. Theory*, 21(5):533–543, September 1975.

[51] Christian Weedbrook, Stefano Pirandola, Raúl García-Patrón, Nicolas J. Cerf, Timothy C. Ralph, Jeffrey H. Shapiro, and Seth Lloyd. Gaussian quantum information. *Rev. Mod. Phys.*, 84(2):621–669, May 2012.

[52] Shao-Hua Xiang and Ke-Hui Song. Exact solution and short-time dynamics of multimode gaussian states embedded in a common non-markovian environment. *Eur. Phys. J. D*, 67(7), July 2013.

[53] Stephen D. Bartlett, Barry C. Sanders, Samuel L. Braunstein, and Kae Nemoto. Efficient classical simulation of continuous variable quantum information processes. *Phys. Rev. Lett.*, 88(9), February 2002.

[54] J. Aasi, J. Abadie, B. P. Abbott, R. Abbott, T. D. Abbott, M. R. Abernathy, C. Adams, T. Adams, P. Addesso, R. X. Adhikari, et al. Enhanced sensitivity of the LIGO gravitational wave detector by using squeezed states of light. *Nat. Photonics*, 7(8):613–619, July 2013.

[55] Raphael C. Pooser and Benjamin Lawrie. Ultrasensitive measurement of microcantilever displacement below the shot-noise limit. *Optica*, 2(5):393–399, May 2015.

[56] Mohammadjavad Dowran, Ashok Kumar, Benjamin J. Lawrie, Raphael C. Pooser, and Alberto M. Marino. Quantum-enhanced plasmonic sensing. *Optica*, 5(5):628–633, May 2018.

[57] B. J. Lawrie, P. D. Lett, A. M. Marino, and R. C. Pooser. Quantum sensing with squeezed light. *ACS Photonics*, 6(6):1307–1318, May 2019.

[58] Seth Lloyd and Samuel L. Braunstein. Quantum computation over continuous variables. *Phys. Rev. Lett.*, 82(8):1784–1787, February 1999.

[59] M. Ohliger, K. Kieling, and J. Eisert. Limitations of quantum computing with gaussian cluster states. *Phys. Rev. A*, 82(4), October 2010.

[60] Mattia Walschaers. Non-gaussian quantum states and where to find them. *PRX Quantum*, 2(3), September 2021.

[61] Warit Asavanant and Akira Furusawa. Non-Gaussian Quantum States. In *Optical Quantum Computers: A Route to Practical Continuous Variable Quantum Information Processing*. AIP Publishing LLC.

[62] R.L. Hudson. When is the wigner quasi-probability density non-negative? *Rep. Math. Phys.*, 6(2):249–252, October 1974.

[63] Francisco Soto and Pierre Claverie. When is the wigner function of multidimensional systems nonnegative? *J. Math. Phys.*, 24(1):97–100, January 1983.

[64] G. Adesso, F. Dell'Anno, S. De Siena, F. Illuminati, and L. A. M. Souza. Optimal estimation of losses at the ultimate quantum limit with non-gaussian states. *Phys. Rev. A*, 79(4), April 2009.

[65] Pieter Kok, W. J. Munro, Kae Nemoto, T. C. Ralph, Jonathan P. Dowling, and G. J. Milburn. Linear optical quantum computing with photonic qubits. *Rev. Mod. Phys.*, 79(1):135–174, January 2007.

[66] Michael A Nielsen and Isaac L Chuang. *Quantum Computation and Quantum Information*. Cambridge University Press, Cambridge, England, December 2010.

[67] Dik Bouwmeester, Jian-Wei Pan, Klaus Mattle, Manfred Eibl, Harald Weinfurter, and Anton Zeilinger. Experimental quantum teleportation. *Nature*, 390(6660):575–579, December 1997.

[68] B. A. Bell, D. A. Herrera-Martí, M. S. Tame, D. Markham, W. J. Wadsworth, and J. G. Rarity. Experimental demonstration of a graph state quantum error-correction code. *Nat. Commun.*, 5(1), April 2014.

[69] R. E. Slusher, L. W. Hollberg, B. Yurke, J. C. Mertz, and J. F. Valley. Observation of squeezed states generated by four-wave mixing in an optical cavity. *Phys. Rev. Lett.*, 55(22):2409–2412, November 1985.

[70] Ling-An Wu, H. J. Kimble, J. L. Hall, and Huifa Wu. Generation of squeezed states by parametric down conversion. *Physical Review Letters*, 57(20):2520–2523, November 1986.

[71] R. M. Shelby, M. D. Levenson, S. H. Perlmutter, R. G. DeVoe, and D. F. Walls. Broad-band parametric deamplification of quantum noise in an optical fiber. *Phys. Rev. Lett.*, 57(6):691–694, August 1986.

[72] Alexandre Z. Leger, Samridhi Gambhir, Julien Légère, and Deny R. Hamel. Amplification of cascaded down-conversion by reusing photons with a switchable cavity. *Phys. Rev. Res.*, 5:023131, May 2023.

[73] Ofir Yesharim, Shaul Pearl, Joshua Foley-Comer, Irit Juwiler, and Ady Arie. Direct generation of spatially entangled qudits using quantum nonlinear optical holography. *Sci. Adv.*, 9(8), February 2023.

[74] Sangbae Kim and Byoung S. Ham. Observations of the delayed-choice quantum eraser using coherent photons. *Sci. Rep.*, 13(1), June 2023.

[75] R Brouri, A Beveratos, J P Poizat, and P Grangier. Photon antibunching in the fluorescence of individual color centers in diamond. *Opt. Lett.*, 25(17):1294–1296, September 2000.

[76] P Michler, A Kiraz, C Becher, W V Schoenfeld, P M Petroff, L Zhang, E Hu, and A Imamoglu. A quantum dot single-photon turnstile device. *Science*, 290(5500):2282–2285, December 2000.

[77] Pascale Senellart, Glenn Solomon, and Andrew White. High-performance semiconductor quantum-dot single-photon sources. *Nat. Nanotechnol.*, 12(11):1026–1039, November 2017.

[78] Rahul Trivedi, Kevin A. Fischer, Jelena Vučković, and Kai Müller. Generation of non-classical light using semiconductor quantum dots. *Adv. Quantum Technol.*, 3(1):1900007, December 2019.

[79] Ravitej Uppu, Hans T. Eriksen, Henri Thyrrestrup, Aslı D. Uğurlu, Ying Wang, Sven Scholz, Andreas D. Wieck, Arne Ludwig, Matthias C. Löbl, Richard J. Warburton, Peter Lodahl, and Leonardo Midolo. On-chip deterministic operation of quantum dots in dual-mode waveguides for a plug-and-play single-photon source. *Nat. Commun.*, 11(1), July 2020.

[80] Dan Cogan, Zu-En Su, Oded Kenneth, and David Gershoni. Deterministic generation of indistinguishable photons in a cluster state. *Nat. Photonics*, 17(4):324–329, February 2023.

[81] Jack Y. Qiu, Arne Grimsmo, Kaidong Peng, Bharath Kannan, Benjamin Lienhard, Youngkyu Sung, Philip Krantz, Vladimir Bolkhovsky, Greg Calusine, David Kim, Alex Melville, Bethany M. Niedzielski, Jonilyn Yoder, Mollie E. Schwartz, Terry P. Orlando, Irfan Siddiqi, Simon Gustavsson, Kevin P. O'Brien, and William D. Oliver. Broadband squeezed microwaves and amplification with a josephson travelling-wave parametric amplifier. *Nat. Phys.*, 19(5):706–713, February 2023.

[82] Bharath Kannan, Aziza Almanakly, Youngkyu Sung, Agustin Di Paolo, David A. Rower, Jochen Braumüller, Alexander Melville, Bethany M. Niedzielski, Amir Karamlou, Kyle Serniak, Antti Vepsäläinen, Mollie E. Schwartz, Jonilyn L. Yoder, Roni Winik, Joel I-Jan Wang, Terry P. Orlando, Simon Gustavsson, Jeffrey A. Grover, and William D. Oliver. On-demand directional microwave photon emission using waveguide quantum electrodynamics. *Nat. Phys.*, 19(3):394–400, January 2023.

[83] Nancy Aggarwal, Torrey J. Cullen, Jonathan Cripe, Garrett D. Cole, Robert Lanza, Adam Libson, David Follman, Paula Heu, Thomas Corbitt, and Nergis Mavalvala. Room-temperature optomechanical squeezing. *Nat. Phys.*, 16(7):784–788, July 2020.

[84] Javier Argüello-Luengo and Darrick E Chang. Optomechanical strong coupling between a single photon and a single atom. *New J. Phys.*, 24(2):023006, February 2022.

[85] P. Kharel, Y. Chu, D. Mason, E. A. Kittlaus, N. T. Otterstrom, S. Gertler, and P. T. Rakich. Multimode strong coupling in cavity optomechanics. *Phys. Rev. Appl.*, 18(2), August 2022.

[86] F. J. Dyson. The radiation theories of tomonaga, schwinger, and feynman. *Phys. Rev.*, 75(3):486–502, February 1949.

[87] Michael Reed and Barry Simon. *I: Functional Analysis: Volume 1*. Methods of Modern Mathematical Physics. Academic Press, San Diego, CA, 2 edition, February 1981.

[88] César R. de Oliveira. *Intermediate Spectral Theory and Quantum Dynamics (Progress in Mathematical Physics, 54)*, page 423. Birkhäuser, hardcover edition, 11 2008.

[89] Juzar Thingna, Hangbo Zhou, and Jian-Sheng Wang. Improved dyson series expansion for steady-state quantum transport beyond the weak coupling limit: Divergences and resolution. *J. Chem. Phys.*, 141(19), nov 2014.

[90] Michael Reed and Barry Simon. *II: Fourier Analysis, Self-Adjointness: Volume 2*, pages 282–283. Methods of Modern Mathematical Physics. Academic Press, San Diego, CA, November 1975.

[91] Michael Baake and Ulrike Schlaegel. The peano-baker series. 2010.

[92] Tepper L. Gill. The feynman-dyson view. *J. Phys.: Conf. Ser.*, 845:012023, may 2017.

[93] Marco Frasca. Theory of dressed states in quantum optics. *Phys. Rev. A*, 60(1):573–581, jul 1999.

[94] Kevin Fischer. Derivation of the quantum-optical master equation based on coarse-graining of time. *J. Phys. Commun.*, 2(9):091001, sep 2018.

[95] Agata M. Brańczyk, Thomas M. Stace, T. C. Ralph, Timothy Ralph, and Ping Koy Lam. Time ordering in spontaneous parametric down-conversion. In *AIP Conference Proceedings*. AIP, 2011.

[96] Daniel Puzzuoli, Sophia Fuhui Lin, Moein Malekakhlagh, Emily Pritchett, Benjamin Rosand, and Christopher J. Wood. Algorithms for perturbative analysis and simulation of quantum dynamics. *J. Comput. Phys.*, 489:112262, sep 2023.

[97] Xiang Zhang, Kuan Zhang, Yangchao Shen, Shuaining Zhang, Jing-Ning Zhang, Man-Hong Yung, Jorge Casanova, Julen S. Pedernales, Lucas Lamata, Enrique Solano, and Kihwan Kim. Experimental quantum simulation of fermion-antifermion scattering via boson exchange in a trapped ion. *Nat. Commun.*, 9(1), jan 2018.

[98] Ross Shillito, Jonathan A. Gross, Agustin Di Paolo, Élie Genois, and Alexandre Blais. Fast and differentiable simulation of driven quantum systems. *Phys. Rev. Res.*, 3(3), sep 2021.

[99] Wilhelm Magnus. On the exponential solution of differential equations for a linear operator. *Commun. Pure Appl. Math*, 7(4):649–673, November 1954.

[100] S. Blanes, F. Casas, J.A. Oteo, and J. Ros. The magnus expansion and some of its applications. *Phys. Rep.*, 470(5-6):151–238, January 2009.

[101] D. P. Burum. Magnus expansion generator. *Phys. Rev. B*, 24(7):3684–3692, oct 1981.

[102] W. R. Salzman. An alternative to the magnus expansion in time-dependent perturbation theory. *J. Chem. Phys.*, 82(2):822–826, jan 1985.

[103] Taiki Haga. Divergence of the floquet-magnus expansion in a periodically driven one-body system with energy localization. *Phys. Rev. E*, 100(6), dec 2019.

[104] W.R. Salzman. On the convergence of exponential perturbation theories in the schrödinger representation. *Chem. Phys. Lett.*, 124(6):531–533, mar 1986.

[105] W. R. Salzman. New criterion for convergence of exponential perturbation theory in the schrödinger representation. *Phys. Rev. A*, 36(10):5074–5076, nov 1987.

[106] Per Christian Moan and Jitse Niesen. Convergence of the magnus series. *Found. Comput. Math.*, 8(3):291–301, nov 2007.

[107] Michael Klaiber, Darko Dimitrovski, and John S Briggs. The magnus expansion for interaction of atoms with attosecond laser pulses. *J. Phys. B: At., Mol. Opt. Phys.*, 41(17):175002, aug 2008.

[108] Eugene Stephane Mananga and Thibault Charpentier. On the floquet–magnus expansion: Applications in solid-state nuclear magnetic resonance and physics. *Phys. Rep.*, 609:1–49, jan 2016.

[109] Tobias Lipfert, Dmitri B. Horoshko, Giuseppe Patera, and Mikhail I. Kolobov. Bloch-messiah decomposition and magnus expansion for parametric down-conversion with monochromatic pump. *Phys. Rev. A*, 98(1), jul 2018.

[110] Yu Guo, Xiaobing Luo, Shan Ma, and Chuan-Cun Shu. All-optical generation of quantum entangled states with strictly constrained ultrafast laser pulses. *Phys. Rev. A*, 100(2), aug 2019.

[111] Tuguldur Kh. Begzjav and Hichem Eleuch. Magnus expansion applied to a dissipative driven two-level system. *Results Phys.*, 17:103098, jun 2020.

[112] Ludovico Latmiral and Florian Mintert. Deterministic preparation of highly non-classical macroscopic quantum states. *npj Quantum Inf.*, 4:44, September 2018.

[113] S. Mancini, V. I. Man'ko, and P. Tombesi. Ponderomotive control of quantum macroscopic coherence. *Phys. Rev. A*, 55(4):3042–3050, April 1997.

[114] James Wei and Edward Norman. Lie algebraic solution of linear differential equations. *J. Math. Phys.*, 4(4):575–581, apr 1963.

[115] Sofia Qvarfort and Igor Pikovski. Solving quantum dynamics with a lie algebra decoupling method, 2022.

[116] U. Haeberlen and J. S. Waugh. Coherent averaging effects in magnetic resonance. *Phys. Rev.*, 175(2):453–467, nov 1968.

[117] A. B. Klimov, L. L. Sánchez-Soto, A. Navarro, and E. C. Yustas. Effective hamiltonians in quantum optics: a systematic approach. *J. Mod. Opt.*, 49(13):2211–2226, nov 2002.

[118] Holger Haas, Daniel Puzzuoli, Feihao Zhang, and David G Cory. Engineering effective hamiltonians. *New J. Phys.*, 21(10):103011, oct 2019.

[119] Rüdiger Achilles and Andrea Bonfiglioli. The early proofs of the theorem of campbell, baker, hausdorff, and dynkin. *Arch. Hist. Exact Sci.*, 66(3):295–358, apr 2012.

[120] H. F. Trotter. On the product of semi-groups of operators. *Proc. Am. Math. Soc.*, 10(4):545–551, 1959.

[121] Naomichi Hatano and Masuo Suzuki. Finding exponential product formulas of higher orders. In *Quantum Annealing and Other Optimization Methods*, pages 37–68. Springer Berlin Heidelberg, nov 2005.

[122] A. Kossakowski. On quantum statistical mechanics of non-hamiltonian systems. *Rep. Math. Phys.*, 3(4):247–274, 1972.

[123] G. Lindblad. On the generators of quantum dynamical semigroups. *Commun. Math. Phys.*, 48(2):119–130, June 1976.

[124] Vittorio Gorini, Andrzej Kossakowski, and E C G Sudarshan. Completely positive dynamical semigroups of N-level systems. *J. Math. Phys.*, 17(5):821–825, May 1976.

[125] Ángel Rivas, A Douglas K Plato, Susana F Huelga, and Martin B Plenio. Markovian master equations: a critical study. *New Journal of Physics*, 12(11):113032, November 2010.

[126] Crispin W Gardiner and Peter Zoller. *Quantum noise*. Springer Series in Synergetics. Springer, Berlin, Germany, 3 edition, August 2004.

[127] Dan Hu, Shang-Yu Huang, Jie-Qiao Liao, Lin Tian, and Hsi-Sheng Goan. Quantum coherence in ultrastrong optomechanics. *Phys. Rev. A*, 91(1), January 2015.

[128] Ralf Betzholz, Bruno G Taketani, and Juan Mauricio Torres. Breakdown signatures of the phenomenological lindblad master equation in the strong optomechanical coupling regime. *Quantum Sci. Technol.*, 6(1):015005, November 2020.

[129] M. Tahir Naseem, André Xuereb, and Özgür E. Müstecaplıoğlu. Thermodynamic consistency of the optomechanical master equation. *Phys. Rev. A*, 98(5), November 2018.

[130] C. W. Gardiner and M. J. Collett. Input and output in damped quantum systems: Quantum stochastic differential equations and the master equation. *Phys. Rev. A*, 31(6):3761–3774, June 1985.

[131] C. W. Gardiner. Driving a quantum system with the output field from another driven quantum system. *Phys. Rev. Lett.*, 70(15):2269–2272, April 1993.

[132] Joshua Combes, Joseph Kerckhoff, and Mohan Sarovar. The SLH framework for modeling quantum input-output networks. *Adv. Phys.: X*, 2(3):784–888, May 2017.

[133] Brahim Lounis and Michel Orrit. Single-photon sources. *Rep. Prog. Phys.*, 68(5):1129–1179, May 2005.

[134] Jianwei Wang, Fabio Sciarrino, Anthony Laing, and Mark G Thompson. Integrated photonic quantum technologies. *Nat. Photonics*, 14(5):273–284, May 2020.

[135] Jeremy L O'Brien, Akira Furusawa, and Jelena Vučković. Photonic quantum technologies. *Nat. Photonics*, 3(12):687–695, December 2009.

[136] Ran Huang, Adam Miranowicz, Jie-Qiao Liao, Franco Nori, and Hui Jing. Nonreciprocal photon blockade. *Phys. Rev. Lett.*, 121(15):153601, October 2018.

[137] Sanjib Ghosh and Timothy C H Liew. Dynamical blockade in a single-mode bosonic system. *Phys. Rev. Lett.*, 123(1):013602, July 2019.

[138] Andrei Faraon, Arka Majumdar, and Jelena Vučković. Generation of nonclassical states of light via photon blockade in optical nanocavities. *Phys. Rev. A*, 81(3):033838, March 2010.

[139] Qian Bin, Xin-You Lü, Shang-Wu Bin, and Ying Wu. Two-photon blockade in a cascaded cavity-quantum-electrodynamics system. *Phys. Rev. A (Coll. Park.)*, 98(4):043858, October 2018.

[140] Y F Han, C J Zhu, X S Huang, and Y P Yang. Electromagnetic control and improvement of nonclassicality in a strongly coupled single-atom cavity-QED system. *Phys. Rev. A (Coll. Park.)*, 98(3):033828, September 2018.

[141] Rahul Trivedi, Marina Radulaski, Kevin A Fischer, Shanhui Fan, and Jelena Vučković. Photon blockade in weakly driven cavity quantum electrodynamics systems with many emitters. *Phys. Rev. Lett.*, 122(24):243602, June 2019.

[142] Yu-Xi Liu, Xun-Wei Xu, Adam Miranowicz, and Franco Nori. From blockade to transparency: Controllable photon transmission through a circuit-QED system. *Phys. Rev. A*, 89(4):043818, April 2014.

[143] Xin Wang, Adam Miranowicz, Hong-Rong Li, and Franco Nori. Multiple-output microwave single-photon source using superconducting circuits with longitudinal and transverse couplings. *Phys. Rev. A (Coll. Park.)*, 94(5):053858, November 2016.

[144] Xiu Gu, Anton Frisk Kockum, Adam Miranowicz, Yu-Xi Liu, and Franco Nori. Microwave photonics with superconducting quantum circuits. *Phys. Rep.*, 718-719:1–102, November 2017.

[145] Hui Wang, Xiu Gu, Yu-Xi Liu, Adam Miranowicz, and Franco Nori. Tunable photon blockade in a hybrid system consisting of an optomechanical device coupled to a two-level system. *Phys. Rev. A*, 92(3):033806, September 2015.

[146] Gui-Lei Zhu, Xin-You Lü, Liang-Liang Wan, Tai-Shuang Yin, Qian Bin, and Ying Wu. Controllable nonlinearity in a dual-coupling optomechanical system under a weak-coupling regime. *Phys. Rev. A (Coll. Park.)*, 97(3):033830, March 2018.

[147] Yuxun Ling and Florian Mintert. Deterministic preparation of nonclassical states of light in cavity optomechanics. *Phys. Rev. Res.*, 3:033071, Jul 2021.

[148] J.R. Johansson, P.D. Nation, and Franco Nori. QuTiP 2: A python framework for the dynamics of open quantum systems. *Comput. Phys. Commun.*, 184(4):1234–1240, April 2013.

[149] J.R. Johansson, P.D. Nation, and Franco Nori. QuTiP: An open-source python framework for the dynamics of open quantum systems. *Comput. Phys. Commun.*, 183(8):1760–1772, August 2012.

[150] D.F. Walls and Gerard J. Milburn, editors. *Quantum Optics*. Springer Berlin Heidelberg, 2008.

[151] Ingemar Bengtsson and Karol Zyczkowski. *Geometry of Quantum States: An Introduction to Quantum Entanglement*. Cambridge University Press, 2006.

[152] Martin Bouillard, Guillaume Boucher, Júlia Ferrer Ortas, Bhaskar Kanseri, and Rosa Tualle-Brouri. High production rate of single-photon and two-photon fock states for quantum state engineering. *Opt. Express*, 27(3):3113–3120, February 2019.

[153] Andreas Kronwald, Florian Marquardt, and Aashish A. Clerk. Arbitrarily large steady-state bosonic squeezing via dissipation. *Phys. Rev. A*, 88(6):063833, December 2013.

[154] Christian Arenz, Cecilia Cormick, David Vitali, and Giovanna Morigi. Generation of two-mode entangled states by quantum reservoir engineering. *J. Phys. B: At., Mol. Opt. Phys.*, 46(22):224001, November 2013.

[155] Muhammad Asjad and David Vitali. Reservoir engineering of a mechanical resonator: generating a macroscopic superposition state and monitoring its decoherence. *J. Phys. B: At., Mol. Opt. Phys.*, 47(4):045502, January 2014.

[156] Yuxun Ling, Sofia Qvarfort, and Florian Mintert. Fast optomechanical photon blockade. *Phys. Rev. Res.*, 5:023148, Jun 2023.

[157] K Stannigel, P Komar, S J M Habraken, S D Bennett, M D Lukin, P Zoller, and P Rabl. Optomechanical quantum information processing with photons and phonons. *Phys. Rev. Lett.*, 109(1):013603, July 2012.

[158] Jie-Qiao Liao and Franco Nori. Photon blockade in quadratically coupled optomechanical systems. *Phys. Rev. A*, 88(2):023853, August 2013.

[159] Jie-Qiao Liao and C K Law. Correlated two-photon scattering in cavity optomechanics. *Phys. Rev. A*, 87(4):043809, April 2013.

[160] Xun-Wei Xu, Yuan-Jie Li, and Yu-Xi Liu. Photon-induced tunneling in optomechanical systems. *Phys. Rev. A*, 87(2):025803, February 2013.

[161] Andreas Kronwald, Max Ludwig, and Florian Marquardt. Full photon statistics of a light beam transmitted through an optomechanical system. *Phys. Rev. A*, 87(1):013847, January 2013.

[162] P Kómár, S D Bennett, K Stannigel, S J M Habraken, P Rabl, P Zoller, and M D Lukin. Single-photon nonlinearities in two-mode optomechanics. *Phys. Rev. A*, 87(1):013839, January 2013.

[163] Xin-You Lü, Wei-Min Zhang, Sahel Ashhab, Ying Wu, and Franco Nori. Quantum-criticality-induced strong kerr nonlinearities in optomechanical systems. *Sci. Rep.*, 3(1):2943, October 2013.

[164] T. C. H. Liew and V. Savona. Single photons from coupled quantum modes. *Phys. Rev. Lett.*, 104(18), May 2010.

[165] H. Flayac and V. Savona. Unconventional photon blockade. *Phys. Rev. A*, 96(5), November 2017.

[166] Bijita Sarma and Amarendra K. Sarma. Unconventional photon blockade in three-mode optomechanics. *Phys. Rev. A*, 98(1), July 2018.

[167] J. Y. Sun and H. Z. Shen. Photon blockade in non-hermitian optomechanical systems with nonreciprocal couplings. *Phys. Rev. A*, 107(4), April 2023.

[168] Jasper Chan, T P Mayer Alegre, Amir H Safavi-Naeini, Jeff T Hill, Alex Krause, Simon Gröblacher, Markus Aspelmeyer, and Oskar Painter. Laser cooling of a nanomechanical oscillator into its quantum ground state. *Nature*, 478(7367):89–92, October 2011.

[169] E Verhagen, S Deléglise, S Weis, A Schliesser, and T J Kippenberg. Quantum-coherent coupling of a mechanical oscillator to an optical cavity mode. *Nature*, 482(7383):63–67, February 2012.

[170] Gregory S MacCabe, Hengjiang Ren, Jie Luo, Justin D Cohen, Hengyun Zhou, Alp Sipahigil, Mohammad Mirhosseini, and Oskar Painter. Nano-acoustic resonator with ultralong phonon lifetime. *Science*, 370(6518):840–843, November 2020.

[171] Hengjiang Ren, Matthew H Matheny, Gregory S MacCabe, Jie Luo, Hannes Pfeifer, Mohammad Mirhosseini, and Oskar Painter. Two-dimensional optomechanical crystal cavity with high quantum cooperativity. *Nat. Commun.*, 11(1):3373, July 2020.

[172] Juan Mauricio Torres, Ralf Betzholz, and Marc Bienert. Optomechanical damping basis. *J. Phys. A: Math. Theor.*, 52(8):08LT02, January 2019.

[173] Sofia Qvarfort, Michael R. Vanner, P. F. Barker, and David Edward Bruschi. Master-equation treatment of nonlinear optomechanical systems with optical loss. *Phys. Rev. A*, 104:013501, Jul 2021.

[174] Yuto Ashida, Zongping Gong, and Masahito Ueda. Non-hermitian physics. *Adv. Phys.*, 69(3):249–435, 2020.

[175] Katherine Holmes, Wasim Rehman, Simon Malzard, and Eva-Maria Graefe. Husimi dynamics generated by non-hermitian hamiltonians. *Phys. Rev. Lett.*, 130:157202, Apr 2023.

[176] Yuxun Ling. Fast-Photon-Blockade-Codes, November 2022.

[177] Wolfram Research, Inc. Mathematica, Version 13.1. Champaign, IL, 2022.

[178] Jun-Ya Yang, Dong-Yang Wang, Cheng-Hua Bai, Si-Yu Guan, Xiao-Yuan Gao, Ai-Dong Zhu, and Hong-Fu Wang. Ground-state cooling of mechanical oscillator via quadratic optomechanical coupling with two coupled optical cavities. *Opt. Express*, 27(16):22855–22867, August 2019.

[179] D Cattiaux, I Golokolenov, S Kumar, M Sillanpää, L Mercier de Lépinay, R R Gazizulin, X Zhou, A D Armour, O Bourgeois, A Fefferman, and E Collin. A macroscopic object passively cooled into its quantum ground state of motion beyond single-mode cooling. *Nat. Commun.*, 12(1):6182, October 2021.

[180] Muhammad Tahir Naseem and Özgür E Müstecaplıoğlu. Ground-state cooling of mechanical resonators by quantum reservoir engineering. *Commun. phys.*, 4(1), December 2021.

[181] Dustin Kleckner, Brian Pepper, Evan Jeffrey, Petro Sonin, Susanna M Thon, and Dirk Bouwmeester. Optomechanical trampoline resonators. *Opt. Express*, 19(20):19708–19716, September 2011.

[182] Faraz Monifi, Jing Zhang, Şahin Kaya Özdemir, Bo Peng, Yu-Xi Liu, Fang Bo, Franco Nori, and Lan Yang. Optomechanically induced stochastic resonance and chaos transfer between optical fields. *Nat. Photonics*, 10(6):399–405, June 2016.

[183] André Xuereb, Claudiu Genes, and Aurélien Dantan. Strong coupling and long-range collective interactions in optomechanical arrays. *Phys. Rev. Lett.*, 109(22):223601, November 2012.

[184] A J Rimberg, M P Blencowe, A D Armour, and P D Nation. A cavity-cooper pair transistor scheme for investigating quantum optomechanics in the ultra-strong coupling regime. *New J. Phys.*, 16(5):055008, May 2014.

[185] Kater W Murch, Kevin L Moore, Subhadeep Gupta, and Dan M Stamper-Kurn. Observation of quantum-measurement backaction with an ultracold atomic gas. *Nat. Phys.*, 4(7):561–564, July 2008.

[186] Monika H Schleier-Smith, Ian D Leroux, Hao Zhang, Mackenzie A Van Camp, and Vladan Vuletić. Optomechanical cavity cooling of an atomic ensemble. *Phys. Rev. Lett.*, 107(14):143005, September 2011.

[187] Polnop Samutpraphoot, Tamara Dordevic, Paloma L. Ocola, Hannes Bernien, Crystal Senko, Vladan Vuletić, and Mikhail D. Lukin. Strong coupling of two individually controlled atoms via a nanophotonic cavity. *Phys. Rev. Lett.*, 124(6):063602, February 2020.

[188] James Millen, Tania S Monteiro, Robert Pettit, and A Nick Vamivakas. Optomechanics with levitated particles. *Rep. Prog. Phys.*, 83(2):026401, February 2020.

[189] Stefan Weis, Rémi Rivière, Samuel Deléglise, Emanuel Gavartin, Olivier Arcizet, Albert Schliesser, and Tobias J. Kippenberg. Optomechanically induced transparency. *Science*, 330(6010):1520–1523, December 2010.

[190] Hao Xiong and Ying Wu. Fundamentals and applications of optomechanically induced transparency. *Appl. Phys. Rev.*, 5(3):031305, September 2018.

[191] Sydney Schreppler, Nicolas Spethmann, Nathan Brahms, Thierry Botter, Maryrose Barrios, and Dan M. Stamper-Kurn. Optically measuring force near the standard quantum limit. *Science*, 344(6191):1486–1489, June 2014.

[192] David Mason, Junxin Chen, Massimiliano Rossi, Yeghishe Tsaturyan, and Albert Schliesser. Continuous force and displacement measurement below the standard quantum limit. *Nat. Phys.*, 15(8):745–749, May 2019.

[193] G. A. Brawley, M. R. Vanner, P. E. Larsen, S. Schmid, A. Boisen, and W. P. Bowen. Nonlinear optomechanical measurement of mechanical motion. *Nat. Comm.*, 7(1), March 2016.

[194] Chao Meng, George A. Brawley, Soroush Khademi, Elizabeth M. Bridge, James S. Bennett, and Warwick P. Bowen. Measurement-based preparation of multimode mechanical states. *Sci. Adv.*, 8(21), May 2022.

[195] Takao Aoki, Barak Dayan, E. Wilcut, W. P. Bowen, A. S. Parkins, T. J. Kippenberg, K. J. Vahala, and H. J. Kimble. Observation of strong coupling between one atom and a monolithic microresonator. *Nature*, 443(7112):671–674, October 2006.

[196] Barak Dayan, A. S. Parkins, Takao Aoki, E. P. Ostby, K. J. Vahala, and H. J. Kimble. A photon turnstile dynamically regulated by one atom. *Science*, 319(5866):1062–1065, February 2008.

[197] Takao Aoki, A. S. Parkins, D. J. Alton, C. A. Regal, Barak Dayan, E. Ostby, K. J. Vahala, and H. J. Kimble. Efficient routing of single photons by one atom and a microtoroidal cavity. *Phys. Rev. Lett.*, 102(8), February 2009.

[198] Ludovico Latmiral. *Quantumness in Optomechanics*. PhD thesis, Imperial College London, 2017.

[199] Yuxun Ling. Deterministic-preparation-of-non-classical-states-of-light-in-cavity-optomechanics, October 2023.

Appendix A

Excess reduction in the autocorrelation function due to cascade coupling

This appendix section presents an examination of the transfer of autocorrelation from the optomechanical cavity to the output cavity in the cascaded model discussed in Fig. 5.1. Herein, I demonstrate that the autocorrelation function within the output cavity can fall below that in the optomechanical cavity.

In mathematical terms, this section seeks to confirm that the increment in the output autocorrelation function

$$\Delta g^{(2)}_{\text{out}} = \frac{\text{Tr}\left(a_2^\dagger a_2^\dagger a_2 a_2 (\rho + \Delta\rho)\right)}{\text{Tr}\left(a_2^\dagger a_2 (\rho + \Delta\rho)\right)^2} - \frac{\text{Tr}\left(a_2^\dagger a_2^\dagger a_2 a_2 \rho\right)}{\text{Tr}\left(a_2^\dagger a_2 \rho\right)^2}, \text{ with}$$
$$\Delta\rho = \frac{\sqrt{\kappa_2 \kappa_r}}{2}\left([a_1\rho, a_2^\dagger] + [a_2, \rho a_1^\dagger]\right)\Delta t \tag{A.1}$$

can be negative when the autocorrelation in the optomechanical cavity is no smaller than that in the output cavity (i.e. when $g^{(2)}_{\text{op}} \geq g^{(2)}_{\text{out}}$). The effect of the Lindblad operator $\mathcal{D}[a_2]$ of the output cavity is neglected in the state increment $\Delta\rho$ for simplicity. This simplification does not affect the qualitative result because the autocorrelation function is preserved under cavity dissipation.

To start with, a most general form of the total system state, after tracing out the mechanical degree of

freedom in the optomechanical system, is given by

$$\rho = \sum_{pqrs} \alpha_{pqrs} \left|p\right\rangle\!\left\langle q\right|_1 \otimes \left|r\right\rangle\!\left\langle s\right|_2 \ , \tag{A.2}$$

where α_{pqrs} are complex coefficients, and $\left|p\right\rangle\!\left\langle q\right|_j$ corresponds to a matrix element in the Fock basis for either the optomechanical cavity ($j = 1$) or the output cavity ($j = 2$). For the given state, the increment in the system state $\Delta\rho$ reads

$$\begin{aligned}
\Delta\rho =& \frac{\sqrt{\kappa_2\kappa_r}}{2} \sum_{pqrs} \alpha_{pqrs} \left(\sqrt{ps}\left|p-1\right\rangle\!\left\langle q\right|_1 \otimes \left|r\right\rangle\!\left\langle s-1\right|_2 - \sqrt{p(r+1)}\left|p-1\right\rangle\!\left\langle q\right|_1 \otimes \left|r+1\right\rangle\!\left\langle s\right|_2 \right) \Delta t + \\
&+ \frac{\sqrt{\kappa_2\kappa_r}}{2} \sum_{pqrs} \alpha_{pqrs} \left(\sqrt{qr}\left|p\right\rangle\!\left\langle q-1\right|_1 \otimes \left|r-1\right\rangle\!\left\langle s\right|_2 - \sqrt{q(s+1)}\left|p\right\rangle\!\left\langle q-1\right|_1 \otimes \left|r\right\rangle\!\left\langle s+1\right|_2 \right) \Delta t \\
=& \frac{\sqrt{\kappa_2\kappa_r}}{2} \sum_{pqrs} \left(\sqrt{(p+1)(s+1)}\alpha_{(p+1)qr(s+1)} - \sqrt{(p+1)r}\alpha_{(p+1)q(r-1)s} \right) \left|p\right\rangle\!\left\langle q\right|_1 \otimes \left|r\right\rangle\!\left\langle s\right|_2 \Delta t + \\
&+ \frac{\sqrt{\kappa_2\kappa_r}}{2} \sum_{pqrs} \left(\sqrt{(q+1)(r+1)}\alpha_{p(q+1)(r+1)s} - \sqrt{(q+1)s}\alpha_{p(q+1)r(s-1)} \right) \left|p\right\rangle\!\left\langle q\right|_1 \otimes \left|r\right\rangle\!\left\langle s\right|_2 \Delta t \ .
\end{aligned} \tag{A.3}$$

The expectation values in Eq. (A.1) only involve the diagonal terms in the density matrix, and can be expressed as following

$$\begin{aligned}
\langle a_2^\dagger a_2(\rho+\Delta\rho)\rangle &= \sum_{jk} k\alpha_{jjkk} - \sum_{jk} \sqrt{\kappa_2\kappa_r}\sqrt{(j+1)(k+1)}\,\mathrm{Re}(\alpha_{(j+1)jk(k+1)})\Delta t \ , \\
\langle a_2^\dagger a_2^\dagger a_2 a_2(\rho+\Delta\rho)\rangle &= \sum_{jk} k(k-1)\alpha_{jjkk} - \sum_{jk} 2k\sqrt{\kappa_2\kappa_r}\sqrt{(j+1)(k+1)}\,\mathrm{Re}(\alpha_{(j+1)jk(k+1)})\Delta t \ ,
\end{aligned} \tag{A.4}$$

where the off diagonal terms $\alpha_{j(j+1)k(k+1)}$ are replaced by their real parts due to the Hermitian nature of the density matrix (i.e. $\alpha_{pqrs} = \alpha^*_{qpsr}$).

For any small time increment Δt satisfying the inequality $\sqrt{\kappa_2\kappa_r}\Delta t \ll 1$, the approximation $1/(x + y\Delta t)^2 \approx (1 - 2y\Delta t/x)/x^2$ is valid for any positive numbers x and y, and thus the increment in the

autocorrelation can be written as

$$\begin{aligned}\Delta g^{(2)}_{\text{out}} \approx & \frac{-2(\sum_{jk} k(k-1)\alpha_{jjkk})(\sum_{jk}\sqrt{(j+1)(k+1)}\,\mathrm{Re}(\alpha_{(j+1)jk(k+1)}))}{\left(\sum_{jk} k\alpha_{jjkk}\right)^3}\delta + \\ & + \frac{2(\sum_{jk} k\sqrt{(j+1)(k+1)}\,\mathrm{Re}(\alpha_{(j+1)jk(k+1)}))(\sum_{jk} k\alpha_{jjkk})}{\left(\sum_{jk} k\alpha_{jjkk}\right)^3}\delta\,,\end{aligned} \tag{A.5}$$

where $\delta = \sqrt{\kappa_2\kappa_r}\Delta t$. In Eq. (A.5), not only the two terms $\propto \delta$ have different signs, but also the real parts of the off-diagonal terms $\mathrm{Re}(\alpha_{(j+1)jk(k+1)})$ that encode the relative phases between Fock components can also take positive or negative values. Therefore, the increment in the output autocorrelation (i.e. $\Delta g^{(2)}_{\text{out}}$) can be positive or negative regardless of the autocorrelation in the optomechanical cavity.

Subsequently, I provide a concrete example that substantiates the above statement. In the simple case when the total system state is pure and separable with a maximum of two photons present in each of the optomechanical and output cavities, the system state can be expressed as $\rho = |\phi_{\text{op}}\rangle\langle\phi_{\text{op}}| \otimes |\phi_{\text{out}}\rangle\langle\phi_{\text{out}}|$, with

$$\begin{aligned}|\phi_{\text{op}}\rangle =& \sqrt{1-p_{1,\text{op}}-p_{2,\text{op}}}\,|0\rangle + \sqrt{p_{1,\text{op}}}e^{i\psi_{1,\text{op}}}\,|1\rangle + \sqrt{p_{2,\text{op}}}e^{i\psi_{2,\text{op}}}\,|0\rangle\ ,\\ |\phi_{\text{out}}\rangle =& \sqrt{1-p_{1,\text{out}}-p_{2,\text{out}}}\,|0\rangle + \sqrt{p_{1,\text{out}}}e^{i\psi_{1,\text{out}}}\,|1\rangle + \sqrt{p_{2,\text{out}}}e^{i\psi_{2,\text{out}}}\,|0\rangle\ .\end{aligned} \tag{A.6}$$

The increment of the autocorrelation function after a short time Δt can then be written as

$$\Delta g^{(2)}_{\text{out}} \approx -\frac{2\delta\sqrt{p_{1,\text{op}}p_{1,\text{out}}p_{2,\text{out}}}}{(p_{1,\text{out}}+2p_{2,\text{out}})^3}\sum_{j=1}^{4} c_j z_j\ , \tag{A.7}$$

with

$$\begin{aligned}z_1 &= 2\sqrt{p_{2,\text{out}}}\sqrt{1-p_{1,\text{op}}-p_{2,\text{op}}}\sqrt{1-p_{1,\text{out}}-p_{2,\text{out}}}\ ,\\ z_2 &= 2\sqrt{2}\sqrt{p_{2,\text{op}}}\sqrt{p_{2,\text{out}}}\sqrt{1-p_{1,\text{out}}-p_{2,\text{out}}}\ ,\\ z_3 &= \sqrt{2}p_{1,\text{out}}\sqrt{1-p_{1,\text{op}}-p_{2,\text{op}}}\ ,\\ z_4 &= 2p_{1,\text{out}}\sqrt{p_{2,\text{op}}}\ ,\\ c_1 &= \cos\left(\pi+\psi_{1,\text{op}}-\psi_{1,\text{out}}\right)\ ,\\ c_2 &= \cos\left(\pi+\psi_{1,\text{op}}+\psi_{1,\text{out}}-\psi_{2,\text{op}}\right)\ ,\\ c_3 &= \cos\left(\psi_{1,\text{op}}+\psi_{1,\text{out}}-\psi_{2,\text{out}}\right)\ ,\\ c_4 &= \cos\left(\psi_{1,\text{op}}-\psi_{1,\text{out}}-\psi_{2,\text{op}}+\psi_{2,\text{out}}\right)\ .\end{aligned} \tag{A.8}$$

In the specific scenario where both the optomechanical system and the output cavity exhibit significant photon blockade such that the inequalities $p_2 \ll (1-p_1-p_2)$ and $p_2 \ll p_1^2$ are satisfied in each cavity, Eq. (A.7) is dominated by the term $\propto c_3 z_3$. The increament in the autocorrelation is thus negative whenever it is satisfied that $c_3 > 0$, or equivalently, $-\pi < \psi_{1,\text{op}} + \psi_{1,\text{out}} - \psi_{2,\text{out}} < \pi$, regardless of whether or not the output cavity has a lower autocorrelation than the optomechanical cavity.

As an example, Fig. A.1 plots the time evolution of the autocorrelation functions, when the initial state of the system is a direct tensor product of two pure states with single-photon population $p_{1,\text{op}} = p_{1,\text{out}} = 0.1$ and autocorrelation $g^{(2)}_{\text{op}} = 10^{-3}$ and $g^{(2)}_{\text{out}} = 10^{-4}$. Despite that the optomechanical autocorrelation is initially one order of magnitude larger than that in the output cavity, the numerical simulation shows varied initial dynamics of the autocorrelation function, which may increase, decrease or remain approximately flat depending on the phases of the single-photon component and the two-photon component.

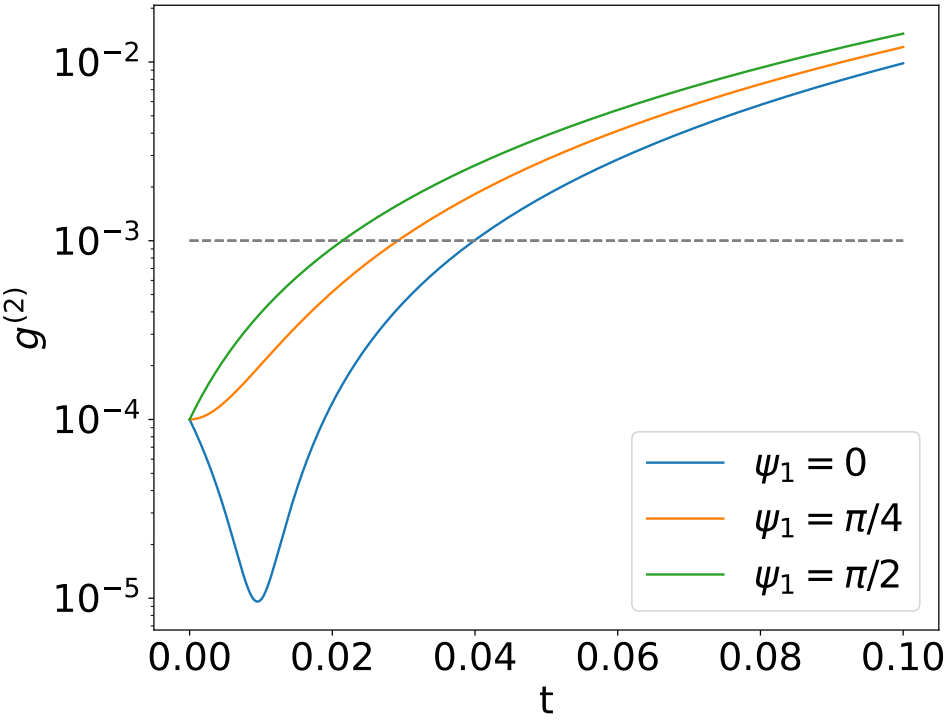


Figure A.1: Time evolution of the autocorrelation function in the output cavity for the initial system state described in Eq. (A.6), with parameters $p_{1,\text{op}} = p_{1,\text{out}} = 0.1$, $g^{(2)}_{\text{op}} = 10^{-3}$, $g^{(2)}_{\text{out}} = 10^{-4}$, $\psi_{2,\text{op}} = \psi_{2,\text{out}} = 0$, and the vacuum and two-photon populations are determined by the values of autocorrelation and the normalization condition. The x-axis is plotted in the unit of coupling strenth (i.e. $\sqrt{\kappa_2 \kappa_r} = 1$) The three curves correspond to the cases where the phase of the single-photon components are $\psi_{1,\text{op}} = \psi_{1,\text{out}} = 0, \pi/4, \pi/2$, respectively. For these three values, c_3 in Eq. (A.8) is positive, zero and negative, respectively, and so does the derivatives of the three curves at $t = 0$. The gray dashed line represents the autocorrelation value in the optomechanical cavity.

Appendix B

Driving profiles used in plots

B.1 Parameters in Chap. 3

In Fig. 3.3, driving strengths over each driven interval $\mathcal{T} = 5T$ read

$$E/\omega_{\mathrm{m}} = 4., 4., 4., 4., 4., 4., 4., 4., 4., 4., 3.56, 3.56, 2.19, 2.19, 2.74, 2.74\ . \tag{B.1}$$

In Fig. 3.4, driving strengths over each driven interval $\mathcal{T} = 5T$ when the optomechanical coupling strength $g_0 = \omega_{\rm m}/26$ read

$$
\begin{aligned}
E/\omega_{\rm m} =&\{4.0, 4.0, 4.0, 4.0, 4.0, 4.0, 4.0, 4.0, 4.0, 4.0, 3.97615762, 2.43055998, 3.6873501,\\
&\quad 1.95440809, 0.04559224, 3.7363291\},\\
&\{4.0, 4.0, 4.0, 4.0, 4.0, 4.0, 4.0, 4.0, 4.0, 4.0, 3.17006597, 4.0, 1.22723673, 1.52223483, 4.0\},\\
&\{4.0, 4.0, 4.0, 4.0, 4.0, 4.0, 4.0, 4.0, 4.0, 3.5495041, 4.0, 1.5971311, 2.36274737, 4.0\},\\
&\{4.0, 4.0, 4.0, 4.0, 4.0, 4.0, 4.0, 4.0, 3.71577367, 4.0, 1.63366753, 3.22583102, 4.0\},\\
&\{4.0, 4.0, 4.0, 4.0, 4.0, 4.0, 4.0, 3.87411802, 4.0, 0.96209439, 4.0, 4.0\},\\
&\{4.0, 4.0, 4.0, 4.0, 4.0, 4.0, 3.88956397, 3.85112561, 1.61025478, 4.0, 4.0\},\\
&\{4.0, 4.0, 4.0, 4.0, 4.0, 4.0, 3.40516261, 2.13973876, 4.0, 4.0\},\\
&\{4.0, 4.0, 4.0, 4.0, 4.0, 3.01725078, 2.33951478, 4.0, 4.0\},\\
&\{4.0, 4.0, 4.0, 4.0, 3.53009253, 0.8734978, 4.0, 4.0\},\\
&\{4.0, 4.0, 4.0, 3.97676322, 0.0, 4.0, 4.0\},\\
&\{4.0, 4.0, 4.0, 1.25045869, 4.0, 4.0\},\\
&\{4.0, 4.0, 4.0, 4.0, 4.0\},\\
&\{4.0, 4.0, 4.0, 4.0\},\\
&\{4.0, 4.0, 4.0\},\\
&\{4.0, 4.0\}\ .
\end{aligned}
\tag{B.2}
$$

When the optomechanical coupling $g_0 = \omega/13$,

$$
\begin{aligned}
E/\omega_{\mathrm{m}} =&\{0.83093504, 0.0, 0.0, 2.10521188, 3.46665956, 2.77389036, 0.22988597, 0.1306046, 0.86739215,\\
&\quad 0.16249172, 1.21165408, 2.85668221, 3.247835, 3.24689537, 2.85721714, 2.3522673\},\\
&\{0.674783, 1.98725721, 2.77445101, 3.37351876, 3.15248317, 2.86872136, 1.69225217, 0.9479075,\\
&\quad 0.4195115, 1.5718756, 2.95950184, 3.08234397, 2.57322173, 0.13098301\},\\
&\{2.32243241, 0.311356, 1.68925154, 3.37609797, 2.79420661, 1.8517636, 2.00062808, 1.25809964,\\
&\quad 2.56401952, 2.45209519, 2.76029606, 3.98158015, 3.83377598, 3.02951596\},\\
&\{2.94037727, 2.33163804, 1.78828629, 1.53691764, 0.792807, 0.5236126, 0.8754181,\\
&\quad 1.84818364, 3.49894809, 3.56598942, 3.4559403, 2.10826174, 1.40657165\},\\
&\{2.31313424, 3.00783591, 0.0, 0.0, 1.06233684, 0.0, 0.15660283, 2.61055237,\\
&\quad 3.44946681, 3.82153135, 3.13792614, 2.59067397\},\\
&\{4.0, 3.78323189, 3.99953547, 3.49068232, 2.72282416, 0.32744249, 0.07638135,\\
&\quad 1.85979568, 2.50356829, 2.12706333, 1.42569084\},\\
&\{3.49038164, 0.0, 0.0, 0.0, 2.75168283, 0.88558901, 4.0, 4.0, 4.0, 2.60935021\},\\
&\{0.0, 0.0, 4.0, 4.0, 3.76746468, 2.42546703, 1.14962237, 0.0, 0.000999952145\},\\
&\{4.0, 4.0, 4.0, 2.95518955, 0.97831183, 0.0, 1.0529061, 1.76085499\},\\
&\{4.0, 4.0, 3.76746682, 2.42533462, 1.14979777, 0.0, 0.00462229\},\\
&\{0.0, 3.12325688, 4.0, 4.0, 3.05750842, 1.4690436\},\\
&\{4.0, 4.0, 3.76745115, 2.42540346, 1.14966943\},\\
&\{4.0, 4.0, 3.69069554, 2.26722955\},\\
&\{4.0, 4.0, 3.39113346\},\\
&\{4.0, 3.47665854\}\ .
\end{aligned}
\tag{B.3}
$$

for $t_{\mathrm{f}} = 16\mathcal{T}, 15\mathcal{T}, ..., 2\mathcal{T}$, respectively.

When the optomechanical coupling takes the values

$$g_0/\omega_{\rm m} = 1/26, 1/25, 2/49, 2/47, 2/45, 1/22, 1/21, 1/20, 1/19, 1/18, 1/17, 1/16, 1/15, 1/14, 1/13 \tag{B.4}$$

and,

$$\begin{aligned} E/\omega_{\rm m} =& \{4., 4., 4., 4., 4., 4., 4., 4., 4., 4., \\ & \quad 2.49797375, 3.59489053, 2.08846815, 0., 3.70603786\}, \\ & \{4., 4., 4., 4., 4., 4., 4., 4., 4., 2.98076997, \\ & \quad 3.18952502, 2.43134345, 1.18002863, 3.31344385\}, \\ & \{4., 4., 4., 4., 4., 4., 4., 4., 3.68650052, \\ & \quad 2.990641, 2.89324996, 0., 3.63966483\}, \\ & \{4., 4., 4., 4., 4., 4., 4., 4., 3.93645222, \\ & \quad 2.84478589, 3.17641015, 0., 3.46080055\}, \\ & \{4., 4., 4., 4., 4., 4., 4., 4., 3.09525006, \\ & \quad 3.23263751, 0.43243956, 3.32943828\}, \\ & \{4., 4., 4., 4., 4., 4., 4., 3.68606787, 3.37912976, 0., 3.63974771\}, \\ & \{4., 4., 4., 4., 4., 4., 3.91014959, 3.42725666, 1.29097229, 3.47449182\}, \\ & \{4., 4., 4., 4., 4., 4., 3.66716892, 1.66618426, 3.37162242\}, \\ & \{4., 4., 4., 4., 4., 3.94224786, 2.04301788, 3.29227687\}, \\ & \{4., 4., 4., 4., 4., 2.67924787, 3.13455576\}, \\ & \{4., 4., 4., 4., 3.21014382, 3.09264885\}, \\ & \{4., 4., 4., 3.563877, 3.28142102\}, \\ & \{4., 4., 3.7853928, 3.58642551\}, \\ & \{4.0, 4.0, 3.39113346\}, \\ & \{4.0, 3.47665854\} \ . \end{aligned} \tag{B.5}$$

for $t_{\rm f} = 16\mathcal{T}, 15\mathcal{T}, ..., 2\mathcal{T}$, respectively.

In Fig. 3.5, driving strengths over each driven interval $\mathcal{T} = 5T$ read

$$\begin{aligned} E/\omega_{\rm m} =& 4., 3.69291531, 3.51161495, 3.686096, 2.60729845, 3.19989213, \\ & 3.13977697, 1.51847303, 2.00439795, 3.9995126 \end{aligned} \tag{B.6}$$

The parameters used in Fig. 3.6 can be found in 'optimizedDrivingData.csv' at [199].

The parameters used in Sec. 3.5 have $\{g_0/\omega_{\rm m}, t_{\rm f}/\mathcal{T}\}$ equal to $\{1/26, 16\}$, $\{1/21, 10\}$, $\{1/16, 5\}$ and the driving strengths $E/\omega_{\rm m}$ for each driven period equal to

$$\begin{aligned} &\{4.0, 4.0, 4.0, 4.0, 4.0, 4.0, 4.0, 4.0, 4.0, 4.0, 3.97615762, \\ &\quad 2.43055998, 3.6873501, 1.95440809, 0.04559224, 3.7363291\}, \\ &\{4., 4., 4., 4., 4., 4., 3.91014959, 3.42725666, 1.29097229, 3.47449182\}\ , \\ &\{4., 4., 4., 3.563877, 3.28142102\} \end{aligned} \tag{B.7}$$

for the parameter sets (i) , (ii) and (iii) respectively.

B.2 Parameters in Chap. 4

The parameters used in Fig. 4.3 and Fig. 4.5 can be found in 'param_vs_res.xlsx' at [176].

In Fig. 4.4, the amplitude of the monochromatic driving reads $E/\omega_{\rm m} = 1/200$ and its detuning from the cavity resonance frequency reads $\Delta/\omega_{\rm m} = -0.0395255$. The bichromatic driving have two driving components with driving amplitudes $E/\omega_{\rm m} = 1/200, e^{2.83667i}/200$ and detunings $\Delta/\omega_{\rm m} = -0.0192947, -0.0282437$ respectively.

In Fig. 4.6 and Sec. 4.4, the bichromatic driving have two driving components with driving amplitudes $E/\omega_{\rm m} = 1/200, e^{1.4571i}/200$ and detunings $\Delta/\omega_{\rm m} = 0.0165539, -0.0364786$ respectively.

In Sec. 4.3.4, the bichromatic driving have two driving components with driving amplitudes $E/\omega_{\rm m} = 1/200, e^{0.847036}/200$ (or $E/\omega_{\rm m} = 1/20, e^{0.847036}/20$ when the driving strength is increased by tenfold) and detunings $\Delta/\omega_{\rm m} = 0.0324604, -0.0412605$ respectively.

B.3 Parameters in Chap. 5

The four parameters sets in the section are listed in B.1

E_0/ω_m	g_0/ω_m	ω_c/ω_m	ω_o/ω_m	Δ_1/ω_m	Δ_2/ω_m	ψ/ω_m	κ_l/ω_m	κ_r/ω_m
0.005	0.28	0	0	0.007132	-0.00066	2.87197	0.01	0.01
0.005	0.3	0	0	-0.01929	-0.02824	2.83667	0.01	0.01
0.005	0.32	0	0	-0.049	-0.05739	2.85863	0.01	0.01
0.005	0.3	0	0	0.016554	-0.03648	1.4571	0.01	0.01

Table B.1: Parameters in Sec. 5.3.